Measuring the charged pion and kaon contributions to the T2K neutrino beam in neutrino and antineutrino running modes using ν_μ and $\bar{\nu}_\mu$ CC inclusive selections in the ND280 detector

Alasdair Knox

Lancaster University

November 14, 2018

Lancaster University

Declaration

No part of this thesis has been previously submitted for the award of a higher degree.

Abstract

Tokai to Kamioka (T2K) is a long-baseline experiment designed to study neutrino oscillations using an (anti)neutrino beam. The beam is created by colliding 30 GeV protons with a stationary graphite target. Secondary hadrons, primarily pions and kaons, are selected using magnetic horns and they subsequently decay to final states that include neutrinos. Depending on the magnetic horn current, a neutrino or antineutrino enhanced beam can be produced. It is important to understand the flux and flavour content of the beam, in order to maximise sensitivity of the experiment. The T2K experiment uses flux models constrained by external measurement from the NA61/SHINE experiment [1] [2]. Despite this, an *in-situ* measurement is required to confirm the flux model derived from the NA61/SHINE data, account for time variations and any other differences between the modelled and actual beamline.

This thesis used inclusive charged-current (CC) ν_μ and $\bar{\nu}_\mu$ selections to obtain (anti)muon samples binned in reconstructed momentum. A χ^2 fit, which took into account all statistical and shape-only systematic errors, was performed on the (anti)muon momentum distributions to determine the parent hadron yields. The fit was performed on each neutrino and antineutrino T2K data run separately, and to the entire neutrino data set. The data to Monte Carlo ratio for the parent hadron yields, with shape-only uncertainties applied, was found to be 1.080 ± 0.039 for π^+ and 0.981 ± 0.080 for K$^+$ in the neutrino enhanced data set, and 1.113 ± 0.124 for π^+, 1.089 ± 0.182 for K$^+$, 0.980 ± 0.069 for π^- and 0.880 ± 0.230 for K$^-$, in the antineutrino enhanced run 6 data set. This shape-only analysis provides a comparison of neutrino parent yields relative to each other. This does not constitute an absolute measurement of the yields as that would limited by the normalisation uncertainties on the cross-section models, at around 10%. The normalisation uncertainties have been added after the fit and the resulting distribution is consistent with the nominal distribution at the 1σ level. No significant time variation was found, and results were in agreement with the NA61 model at around the 2σ level for neutrino and antineutrino beams.

Preface

As part of the T2K collaboration this work was performed through a combination of my own efforts with elements drawn from the expertise and previous work of others within the collaboration, which has been adapted to meet the needs of this analysis.

Chapter 2 gives an overview of the theory behind neutrino physics which is relevant to multiple experiments. The T2K experiment is described in chapter 3 with my contributions to the experiment consisting of monitoring part of the data distribution system and time spent on-site as data acquisition expert.

An overview of the neutrino parent analysis and the selections used is presented in chapter 4. This analysis provides a cross-check of the neutrino parent yields used in the T2K neutrino flux model using muon (anti)neutrino events in the ND280 detector. This is performed using previously existing neutrino running ν_μ and antineutrino running ν_μ and $\bar\nu_\mu$ selections. During this analysis I developed as joint ν_μ and $\bar\nu_\mu$ analysis package by combining these selections.

Chapter 5 describes the fitting method I developed for this analysis and the propagation of the systematic uncertainties. The systematic uncertainty propagation is performed using highland2/psyche for detector systematics and xsTool for all remaining systematics. These tools have been developed by several members of the T2K collaboration. I then subjected the fitting method to a variety of tests, described in chapter 6, to confirm that it was behaving as expected.

In addition to the muon (anti)neutrino analysis I performed the first study on whether further information on neutrino parent yields could be gathered using an electron neutrino selection. The process used is described in chapter 8 with the conclusion that an analysis may be possible when more data becomes available.

Acknowledgements

Firstly I would like to thank Dr. Helen O'Keeffe, Dr. Laura Kormos and Prof. Peter Ratoff for their help throughout. I would also like to thank the many students, and ex-wildlife, that I have shared an office with, as there would be far fewer memories otherwise.

Thank you to Rosie Knox for putting up with the all too frequent trips to Japan and planning many trips out there to make it seem far more worthwhile!

Finally I would like to thank all the members of the various Graduate College bar sports teams, Historia Normannis and 'The Spanish Inquizition' for consuming every remaining minute of my free time and ensuring I retained at least some sanity.

Contents

List of Figures

List of Tables

Chapter 1

Introduction

The Standard Model, described in chapter 2, is the best current model for subatomic interactions and the accuracy of its predictions is such that particles are often inferred from measurements long before being discovered. However there are still many observations which cannot be explained by this alone.

Possibly the most significant example is the asymmetry between the amount of matter and antimatter in the universe. In order to explain this it is required that there be differences between matter and antimatter at levels far greater than has currently been observed in the quark sector. It is therefore important to determine what effects the may be within the lepton sector. Neutrino oscillations, in itself evidence for physics beyond the Standard Model, provide a mechanism for observing this effect, as described in section 2.1.

The T2K experiment sets out to measure a number of the neutrino mixing parameters by observing oscillations that occur from a predominantly muon (anti)neutrino beam. However it is not possible to produce a completely pure, single-flavour neutrino beam and as such it is necessary to understand the relative contributions in order to produce accurate oscillation results.

In the T2K experiment the flux models are constrained using hadron production data from the NA61/SHINE experiment [1] [2], described in section 3.1, which uses a similar beam generation setup to T2K. As the flavour of neutrino is dependent on the hadron which decayed to produce it is important to understand all particles produced.

This analysis uses muon momentum data from the ND280 detector to provide a cross-check of the hadron production measurements using the selections detailed in chapter 4. The method used for this analysis and the propagation of systematic uncertainties are described in chapter 5 and validation studies are presented in chapter 6. The results of the muon (anti)neutrino analysis is presented in chapter 7.

The muon (anti)neutrino analysis is sensitive to (anti)neutrinos arising from charged pion and kaon decays however there are other particles produced, such as muons and neutral kaons. These can decay to produce electron (anti)neutrinos which is a significant background to appearance measurements at the far detector. Chapter 8 describes a study of whether a similar analysis using an electron neutrino selection is feasible.

Chapter 2

Theory

The neutrino was first inferred in 1930 by Wolfgang Pauli [3] to explain the observed energy spectrum of electrons emitted by beta decay. It had been assumed that it was a two-body decay, with only an electron released, and therefore all the electrons from a given decay were produced with exactly the same energy. However, the measured electrons were observed with a broad spectrum of energies. In addition, the decay, as it was understood, violated angular momentum conservation, with one spin-1/2 particle decaying to two spin-1/2 particles. These required properties, along with conservation of charge, imply that the postulated particle must be neutral, spin-1/2 and have a very low (or zero) mass.

The first direct observation of neutrinos came in 1953 by C. Cowan and F. Reines [4] using interactions in a Cd doped scintillator solution. Anti-neutrinos from nuclear reactors were detected via the reaction

$$\bar{\nu}_e + p \rightarrow n + e^+. \tag{2.1}$$

The observed signal was composed of two parts. First, the positron annihilates with an electron typically producing two photons with combined energy of greater than 1.02 MeV, the rest mass of the two particles, with a distribution peaking at a few MeV before falling away. Approximately 5×10^{-6} s later another signal is produced when the neutron is captured by Cd. However, this is still only evidence for electron antineutrinos. The muon and tau neutrinos were discovered in 1962 [5] and

2000 [6] respectively.

The total number of light neutrino flavours that couple to the weak interaction can be determined using the shape of the Z^0 resonance. The total width of the Z^0 resonance, Γ_z, can be expressed in terms of the partial widths to different decay products as

$$\Gamma_Z = \Gamma_{Z \to l^+ l^-} + \Gamma_{Z \to hadrons} + N_\nu \Gamma_{Z \to \nu \bar{\nu}}, \tag{2.2}$$

where $\Gamma_{Z \to l^+ l^-}$, $\Gamma_{Z \to hadrons}$ and $\Gamma_{Z \to \nu \bar{\nu}}$ are the partial widths for decays to pairs of charged leptons, hadrons and neutrinos respectively and N_ν is the number of light neutrinos $(m_\nu < m_Z/2)$ which couple to the Z boson. The 'invisible' partial decay width $\Gamma_{Z \to \nu \bar{\nu}}$ is calculated using the Standard Model prediction, the other partial widths and the total width can be measured via experiment. Therefore, N_ν can be calculated. The value of N_ν was measured by the four experiments at LEP and found to be 2.9840 ± 0.0082 [7]. This result indicates that there are three light and weakly interacting neutrinos.

The Standard Model picture of neutrinos is as follows:

1. Three distinct flavours of neutrinos identical to those of the charged leptons, with flavour conservation of each.

2. Exactly zero mass.

3. There are only left-handed neutrinos and right-handed antineutrinos.

4. Neutrinos and antineutrinos are distinct (i.e. they are Dirac particles).

However some neutrino experiments began to find results which could not be explained at the time. The Homestake experiment [8] set out to measure the flux of neutrinos from fusion reactions within the Sun and compare the results with those from solar model predictions. In the Homestake experiment, neutrinos were detected using a large tank of chlorine as a target via the reaction

$$\nu_e + \mathrm{Cl} \to \mathrm{Ar}^+ + e^-. \tag{2.3}$$

This reaction is only sensitive to electron neutrinos and the experiment found approximately 1/3 of number of neutrinos predicted by solar models. It was initially believed to be a fault with the experiments or theory, however these results were then confirmed by several experiments using gallium [9] [10] and water [11] as targets, making it very unlikely that the measured discrepancy was caused by experimental error. This was the beginning of the Solar Neutrino Problem which indicated flaws with either our understanding of neutrino physics or solar reaction rates.

The second observed anomaly came from measurements of atmospheric neutrinos produced by cosmic ray interactions in the upper atmosphere. These occur when a high energy particle interacts in the upper atmosphere producing a shower of particles including pions. The pions decay to muons, which subsequently decay to electrons. This process produces muon (anti)neutrinos and electron (anti)neutrinos in a ratio of approximately 2:1.

Results from Super-Kamiokande [12], shown in figure 2.1, show the ratio between the number of observed and predicted rates for electron- and muon-like events as a function of distance travelled over energy, L/E. In the absence of oscillations the number of observed electron- and muon-like events should agree with the MC for all values of L/E. Electron-like events show a stable data-MC ratio, whereas the number of muon-like events decreases at higher values of L/E. Super-Kamiokande is sensitive to both electron and muon (anti)neutrinos but not tau (anti)neutrinos. As the number of electron (anti)neutrinos shows no significant change it is assumed that muon (anti)neutrinos have changed to the third flavour, tau (anti)neutrinos. These observations could not be explained by the Standard Model and this led to the prospect of new physics.

2.1 Neutrino Oscillations

In the Standard Model, neutrinos are massless meaning that flavour changing oscillations should be impossible. The fact that these are observed is evidence of physics beyond the Standard Model as well as not conserving individual lepton flavours.
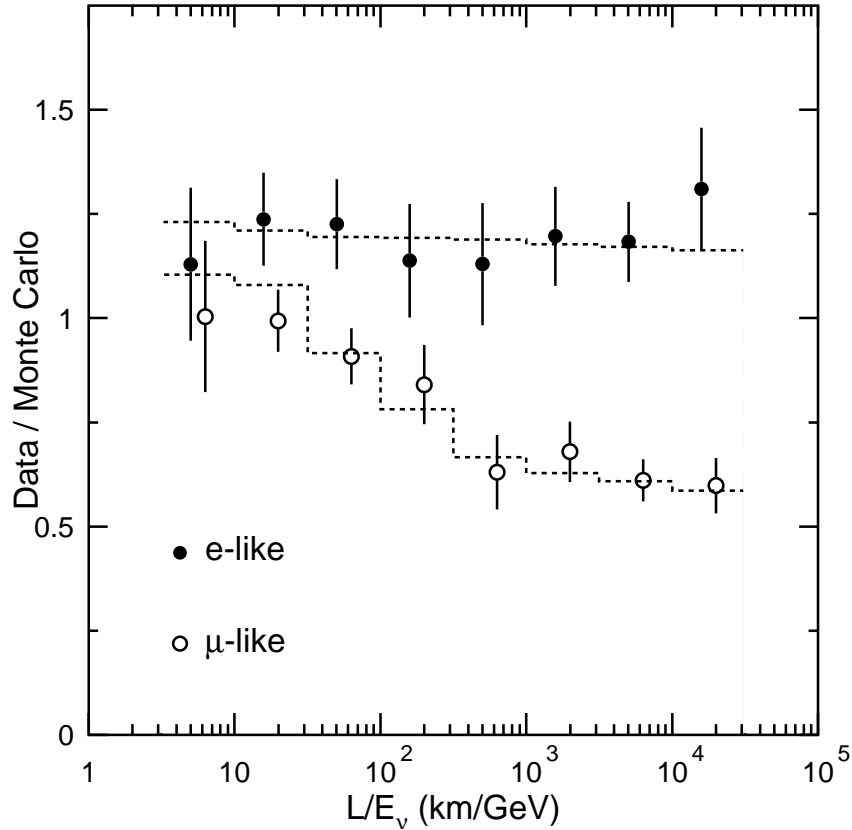
Figure 2.1: The ratio of the number of observed electron- and muon-like rings to unoscillated MC predictions at Super-Kamiokande [12]. The dashed lines show the MC predictions with oscillations applied.

Weak interactions require a set of three well-defined lepton flavour states, with the lepton flavour conserved during interactions. As there are three distinct flavour states there must also be three mass states. If the mass and flavour eigenstates are not equivalent then oscillations occur.

To transform between the flavour and mass states a 3×3 matrix is required. The mixing parameters consist of three 2D rotation angles between flavour and mass eigenstates (θ_{21}, θ_{23} and θ_{13}) and a complex phase, δ_{CP}. If this complex phase, δ_{CP}, is not equal to $0°$ or $180°$ CP is not conserved. The PMNS mixing matrix [13] can be expressed as the product of the three matrices, shown in equation 2.4, where s_{ij} and c_{ij} denote $\sin\theta_{ij}$ and $\cos\theta_{ij}$ respectively and the numbers represent each of the rotation angles.

$$U_{PMNS} = \begin{pmatrix} 1 & 0 & 0 \\ 0 & c_{23} & s_{23} \\ 0 & -s_{23} & c_{23} \end{pmatrix} \begin{pmatrix} c_{13} & 0 & s_{13}e^{-i\delta_{CP}} \\ 0 & 1 & 0 \\ -s_{13}e^{i\delta_{CP}} & 0 & c_{13} \end{pmatrix} \begin{pmatrix} c_{12} & s_{12} & 0 \\ -s_{12} & c_{12} & 0 \\ 0 & 0 & 1 \end{pmatrix}$$

$$= \begin{pmatrix} c_{12}c_{13} & s_{12}c_{13} & s_{13}e^{-i\delta_{CP}} \\ -s_{12}c_{23} - c_{12}s_{23}s_{13}e^{i\delta_{CP}} & c_{12}c_{23} - s_{12}s_{23}s_{13}e^{i\delta_{CP}} & s_{23}c_{13} \\ s_{12}s_{23} - c_{12}c_{23}s_{13}e^{i\delta_{CP}} & -c_{12}s_{23} - s_{12}c_{23}s_{13}e^{i\delta_{CP}} & c_{23}c_{13} \end{pmatrix} \tag{2.4}$$

2.1.1 Two Flavour Mixing

The key points of three flavour mixing can be expressed more clearly by considering the simpler, two flavour case. This is done by considering two flavour states, ν_α and ν_β, and two mass states, ν_1 and ν_2, where $|\nu\rangle$ represents the wavefunction of a given neutrino. The basis states are related by a 2D rotation by an angle, θ, given by:

$$\begin{pmatrix} \nu_\alpha \\ \nu_\beta \end{pmatrix} = \begin{pmatrix} \cos\theta & \sin\theta \\ -\sin\theta & \cos\theta \end{pmatrix} \begin{pmatrix} \nu_1 \\ \nu_2 \end{pmatrix}. \tag{2.5}$$

This provides an expression for each flavour state in terms of a linear superposition of the mass states at the time the neutrino was created. Propagating this forward in time, using natural units, where c and $\hbar = 1$, each mass state gains a complex phase given by:

$$|\nu_{1,2}(t)\rangle = e^{iE_{1,2}t}|\nu_{1,2}\rangle. \tag{2.6}$$

Expanding equation 2.5 and substituting in equation 2.6 gives:

$$|\nu_\alpha(t)\rangle = \cos(\theta)|\nu_1\rangle e^{iE_1 t} + \sin(\theta)|\nu_2\rangle e^{iE_2 t}$$
$$= \left(\cos(\theta)|\nu_1\rangle + \sin(\theta)|\nu_2\rangle e^{i(E_2 - E_1)t} \right) e^{iE_1 t}, \tag{2.7}$$

$$|\nu_\beta(t)\rangle = \left(-\sin(\theta)|\nu_1\rangle + \cos(\theta)|\nu_2\rangle e^{i(E_2 - E_1)t} \right) e^{iE_1 t}. \tag{2.8}$$

The energy, E, of the neutrino can be expressed in terms of its mass, m, and momentum, p, as

$$E^2 = p^2 + m^2,$$
$$E = p\sqrt{1 + \frac{m^2}{p^2}}. \tag{2.9}$$

Due to the very small neutrino mass, it is assumed that the neutrino is highly relativistic meaning that $E \approx p$. Taylor expanding this and discarding higher order terms gives:

$$E \approx p\left(1 + \frac{m^2}{2p^2}\right) \approx p\left(1 + \frac{m^2}{2E^2}\right). \tag{2.10}$$

As momentum, p, is conserved, it is the same for each mass state which means the difference between the two energies can be given by:

$$E_2 - E_1 \approx \frac{m_2^2}{2E} - \frac{m_1^2}{2E} = \frac{\Delta m^2}{2E}, \tag{2.11}$$

$$\Delta m^2 = m_2^2 - m_1^2. \tag{2.12}$$

This means that we can rewrite equations 2.7 and 2.8 as:

$$|\nu_\alpha(t)\rangle = \left(\cos(\theta)|\nu_1\rangle + \sin(\theta)|\nu_2\rangle e^{\frac{i\Delta m^2 t}{2E}}\right)e^{iEt}, \tag{2.13}$$

$$|\nu_\beta(t)\rangle = \left(-\sin(\theta)|\nu_1\rangle + \cos(\theta)|\nu_2\rangle e^{\frac{i\Delta m^2 t}{2E}}\right)e^{iEt}. \tag{2.14}$$

The probabilities can then be extracted for the case where the flavour of the neutrino remains the same and the case in which it changes. The probability, P, for an initial state i to be observed some time, t, later in state j is:

$$P(\nu_i \rightarrow \nu_j) = |\langle\nu_j|\nu_i(t)\rangle|^2. \tag{2.15}$$

Therefore the survival probability is given by:

$$P(\nu_\alpha \rightarrow \nu_\alpha) = |\langle\nu_\alpha|\nu_\alpha(t)\rangle|^2, \tag{2.16}$$

$$P(\nu_\alpha \rightarrow \nu_\alpha) = \left|\left(\cos\theta\langle\nu_1| + \sin\theta\langle\nu_2|\right) \times \left(\left(\cos\theta|\nu_1\rangle + \sin\theta|\nu_2\rangle e^{\frac{i\Delta m^2 t}{2E}}\right)e^{iE_1 t}\right)\right|^2. \tag{2.17}$$

As the mass states are orthogonal $\langle\nu_i|\nu_j\rangle = \delta_{ij}$, where $i, j = 1, 2$. Using orthogonality and that $|e^{iE_1 t}|^2 = 1$, equation 2.17 can be simplified to give:

$$\begin{aligned} P(\nu_\alpha \rightarrow \nu_\alpha) &= \left|\cos^2\theta + \sin^2\theta\, e^{\frac{i\Delta m^2 t}{2E}}\right|^2 \\ &= \cos^4\theta + \cos^2\theta\sin^2\theta\left(e^{\frac{i\Delta m^2 t}{2E}} + e^{\frac{-i\Delta m^2 t}{2E}}\right) + \sin^4\theta \\ &= \cos^4\theta + \sin^4\theta + 2\cos^2\theta\sin^2\theta\cos\left(\frac{\Delta m^2 t}{2E}\right). \end{aligned} \tag{2.18}$$

Using the relation $\cos^2\theta + \sin^2\theta = 1$ to simplify this equation further gives:

$$P(\nu_\alpha \to \nu_\alpha) = (\cos^2\theta + \sin^2\theta)^2 - 2\cos^2\theta\sin^2\theta + 2\cos^2\theta\sin^2\theta\cos\left(\frac{\Delta m^2 t}{2E}\right)$$
$$= 1 - 2\cos^2\theta\sin^2\theta\left(1 - \cos\left(\frac{\Delta m^2 t}{2E}\right)\right).$$
(2.19)

Then using the relations $2\cos\theta\sin\theta = \sin 2\theta$, and $1 - \cos\theta = 2\sin^2(\frac{\theta}{2})$ the probability can be expressed as:

$$P(\nu_\alpha \to \nu_\alpha) = 1 - \sin^2 2\theta \sin^2\left(\frac{\Delta m^2 t}{4E}\right). \tag{2.20}$$

Rather than using the time of flight of the neutrinos, it is more intuitive to consider the distance from the source to the detector. Converting the above equation into appropriate units and using the fact that neutrinos have very little mass, and therefore move at almost the speed of light, gives the survival probability:

$$P(\nu_\alpha \to \nu_\alpha) = 1 - \sin^2 2\theta \sin^2\left(\frac{1.27\Delta m^2 L}{E}\right), \tag{2.21}$$

where L is the distance between the detector and the source of neutrinos, in km, Δm^2 is measured in units of eV^2 and the neutrino energy, E, is in units of GeV.

The other probability is for the case of oscillation to ν_β. For two flavour mixing this is the trivial result:

$$P(\nu_\alpha \to \nu_\beta) = 1 - P(\nu_\alpha \to \nu_\alpha)$$
$$= \sin^2 2\theta \sin^2\left(\frac{1.27\Delta m^2 L}{E}\right). \tag{2.22}$$

2.1.2 Experimental Measurements

The PMNS matrix shown in equation 2.4 contains four parameters. These are three mixing angles (θ_{12}, θ_{23} and θ_{13}) and the CP violating phase (δ_{CP}). In addition to these there are two independent mass squared differences (Δm_{21}^2 Δm_{32}^2). The current global best-fit values for these parameters are given in table 2.1. The two mass splittings, Δm_{21}^2 and Δm_{32}^2, are different by around two orders of magnitude meaning that different oscillations occur at very different values of L/E. The result is that no individual method is sensitive to all mixing parameters and therefore many different

experiments are required. The four types of experiment that will be discussed here are solar, atmospheric, accelerator and reactor experiments. These use different energies, baselines and neutrino sources in order to have sensitivity to different parameters. The parameters are typically divided into three sets based on the types of experiments that have sensitivity in that area. These are solar (θ_{12} and Δm_{21}^2), atmospheric (θ_{23} and Δm_{32}^2) and accelerator (θ_{13} and δ_{CP}).

Solar neutrino experiments measure the flux of relatively low energy (< 20 MeV) neutrinos produced by fusion reactions within the Sun. These experiments observe a deficit of electron neutrino events, with SNO also measuring the predicted total number of neutrino events, as described in section 2.

Reactor neutrino experiments (such as Daya Bay [14], Double Chooz [15], Kam-LAND [16] and RENO [17]) measure electron antineutrino disappearance from nearby nuclear reactors. These experiments are sensitive to θ_{13}, as well as θ_{12} and Δm_{21}^2.

Accelerator based experiments (such as T2K [18], NOVA [19] and MINOS+ [20]) use a proton accelerator to produce a predominantly muon (anti)neutrino beam. These neutrinos have significantly higher energies ($\sim$ GeV) and as such require long baselines of a few hundred kilometres. These experiments are designed with a near detector to measure the unoscillated beam and reduce systematic uncertainties related to the flux, and a far detector located at the first oscillation maximum. These experiments make measurements of both muon neutrino disappearance and electron neutrino appearance and are sensitive to θ_{13}, θ_{23}, Δm_{32}^2 and δ_{CP}. The sensitivity to δ_{CP} is increased by using both ν_μ and $\bar{\nu}_\mu$ enhanced beams.

Solar Parameters

The Solar Neutrino Problem was finally settled in 2002 by the Sudbury Neutrino Observatory (SNO) [22]. SNO was different from previous experiments in that it used a tank of heavy water, deuterium oxide. SNO was sensitive not only to ν_e Charged Current (CC) events, but also Neutral Current (NC) and elastic scattering interactions, both of which are sensitive to all three neutrino flavours. The number of CC ν_e interactions was still a third of the value predicted by solar models, however, the

Parameter	Unit	Normal Ordering	Inverted Ordering
θ_{12}	$^\circ$	$33.56^{+0.77}_{-0.75}$	$33.56^{+0.77}_{-0.75}$
θ_{23}	$^\circ$	$41.6^{+1.5}_{-1.2}$	$50.0^{+1.1}_{-1.4}$
θ_{13}	$^\circ$	$8.46^{+0.15}_{-0.15}$	$8.49^{+0.15}_{-0.15}$
Δm^2_{21}	$\times 10^{-5}$ eV^2	$7.50^{+0.19}_{-0.17}$	$7.50^{+0.19}_{-0.17}$
Δm^2_{32}	$\times 10^{-3}$ eV^2	$+2.524^{+0.039}_{-0.040}$	$-2.514^{+0.038}_{-0.041}$
δ_{CP}	$^\circ$	261^{+51}_{-59}	277^{+40}_{-40}

Table 2.1: Global values for the six neutrino mixing parameters for both normal and inverted mass orderings [21]. Two sets of results are present due to the unknown ordering of the neutrino mass states, discussed in section 2.3.

NC events showed no deficit, thereby showing that electron neutrinos are oscillating to muon and tau neutrinos on their way from the Sun. NC events are the simplest test of the total neutrino flux as the interactions are independent of neutrino flavour whereas electron neutrinos have an extra elastic scattering mode from interactions with electrons. Both solar and reactor neutrino experiments are sensitive to θ_{12} and Δm^2_{21} and the best fit combining solar measurements with KamLAND data is shown in figure 2.2.

Atmospheric Parameters

These parameters are measured through ν_μ disappearance, while θ_{23} can also be measured via ν_e appearance. The first measurements came from atmospheric neutrino observations, with accelerator neutrino measurements also now contributing. The 2D contours for θ_{23} and Δm^2_{32} are shown in figure 2.3. This shows good agreement between the atmospheric results, from Super-K [24] and IceCube [25], and the accelerator results from T2K [18], NOVA [19] and MINOS+ [20].

Accelerator Parameters

Neutrino oscillations successfully explained the observed anomalies and provided measurements of four of the six expected mixing parameters. However, the value of the third mixing angle, θ_{13}, was still unknown. By the time it was successfully measured, it had been shown to be relatively small compared to the other two mixing angles.
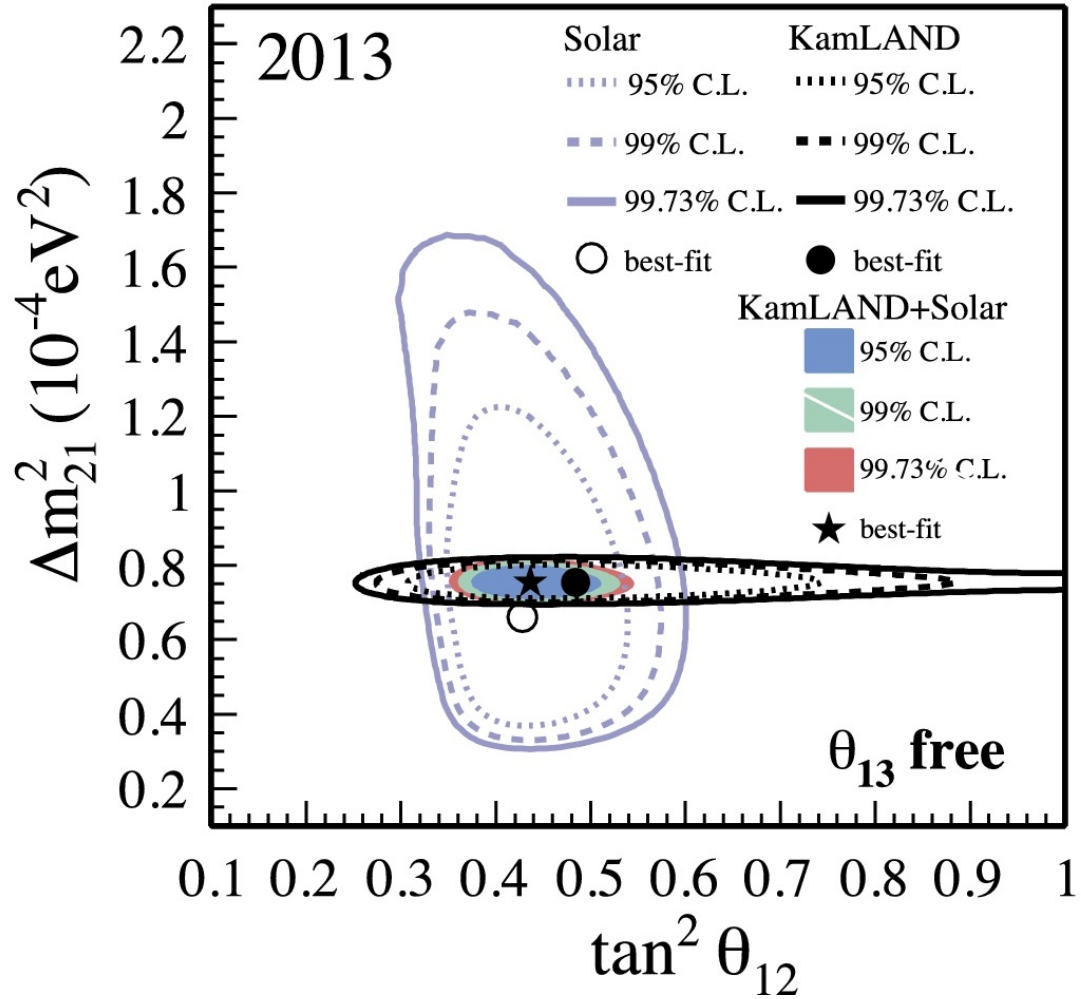
Figure 2.2: 2D contours for $|\Delta m_{21}^2|$ and $\tan^2 \theta_{12}$ combining solar measurements with data from KamLAND. Figure from [23].

The smaller the value of θ_{13} the more challenging it would be to measure the final matrix parameter, a CP violating phase, δ_{CP}. The first measurement of θ_{13} was by Daya Bay [14], a reactor experiment measuring high statistics electron antineutrino disappearance. This was then followed in 2013 by T2K, with the first measurement of electron neutrino appearance in a muon neutrino beam [27].

The final mixing angle, θ_{13}, was found to be towards the larger end of the allowed region from previous searches. As δ_{CP} appears with a factor of $\sin \theta_{13}$, as shown in equation 2.4, this result means that there is a realistic chance of measuring the CP
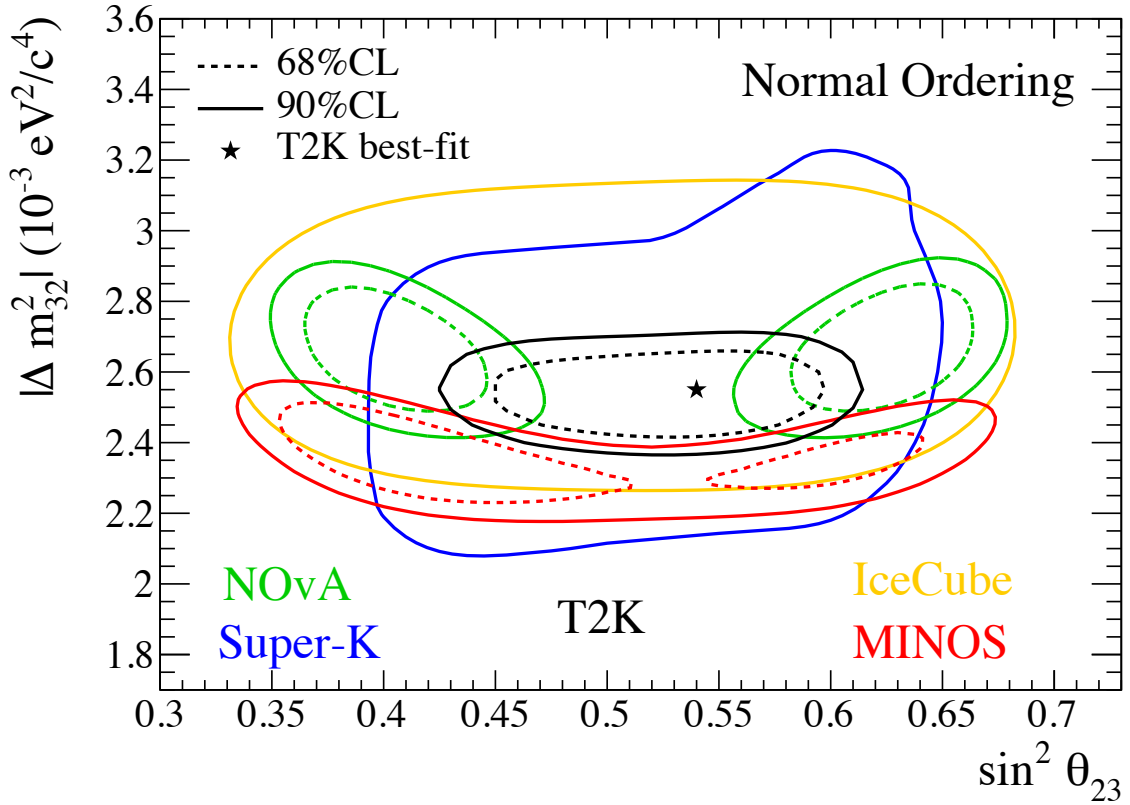
Figure 2.3: 2D contours for $|\Delta m_{32}^2|$ and $\sin^2 \theta_{23}$ from various accelerator (MINOS+, T2K, NOVA) and atmospheric (Super-K, ICECUBE) experiments. Figure from [26].

violating phase. Figure 2.4 shows the T2K best fit point and contours for both normal and inverted mass orderings. The global best fit for θ_{13} is also shown and is dominated by reactor experiments such as Daya Bay [14] and RENO [17].

2.2 Neutrino Interactions

Neutrinos interact with other particles only through the weak force either through the exchange of a $W^\pm$ or Z^0 boson. These are referred to as Charged Current (CC) and Neutral Current (NC) respectively.

The charged current events used in this analysis can be broken down by reaction type, with the cross section for each having a different dependence on neutrino energy, as shown in figure 2.5. For low neutrino energies (< 1 GeV), the cross section is

(a)

(b)
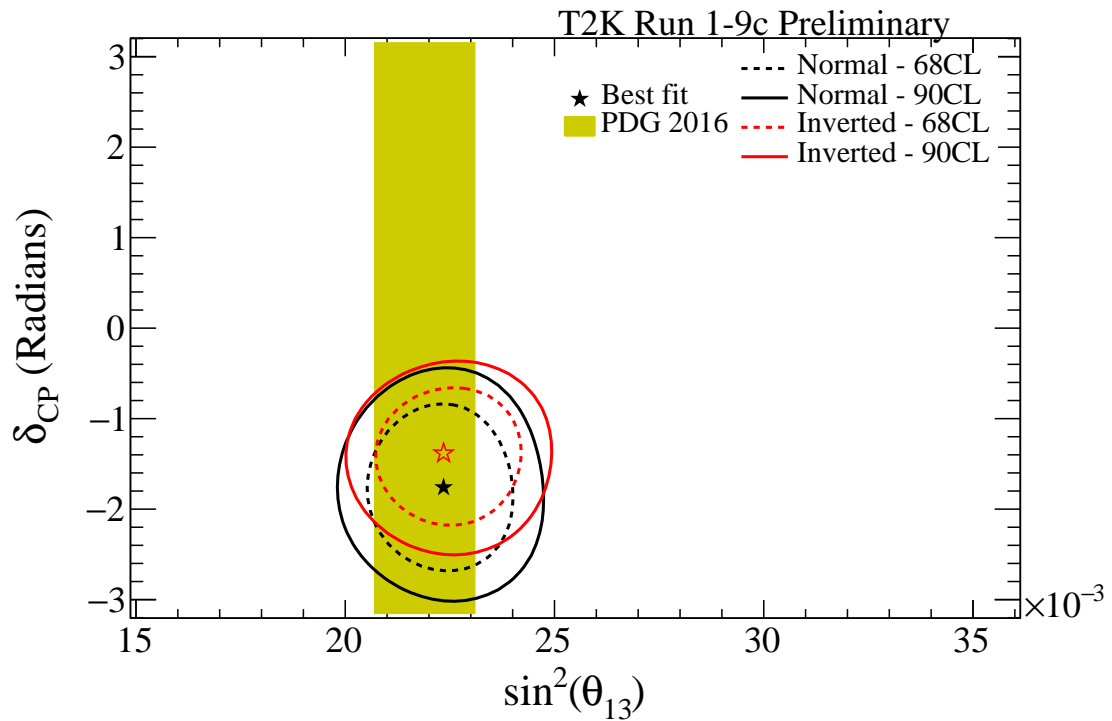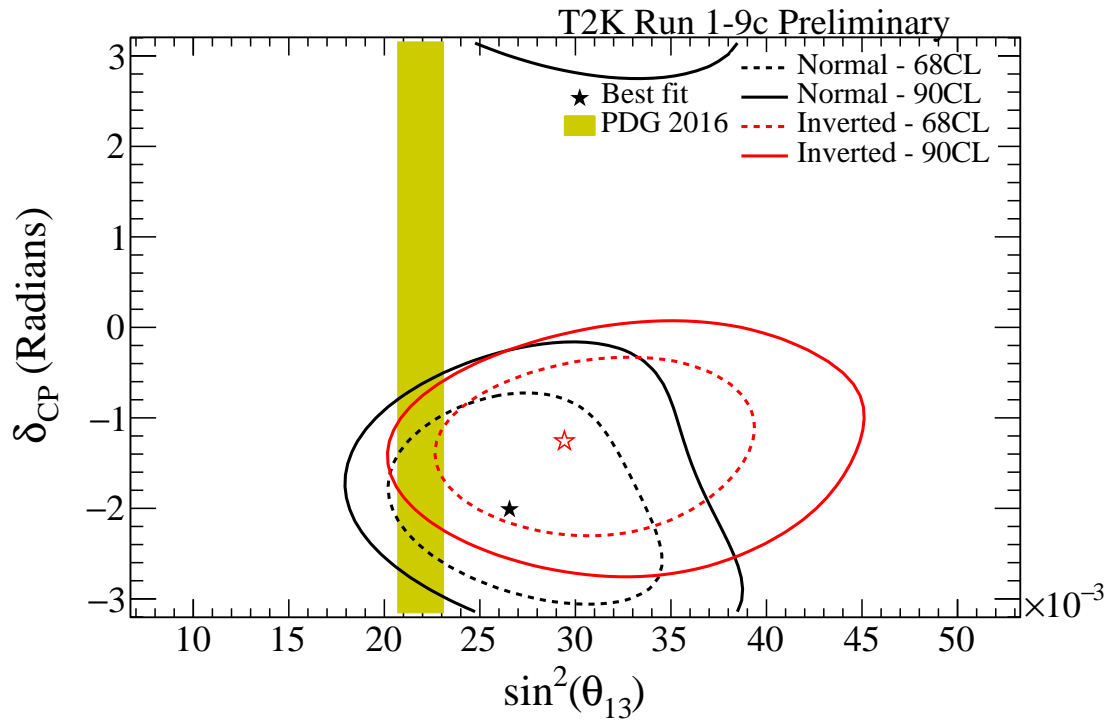
Figure 2.4: T2K best fit point and 2D contours for δ_{CP} and $\sin^2\theta_{13}$ without (a) and with (b) constraints from reactor measurements of $\sin^2\theta_{13}$. Figure from [28].

dominated by the Quasi-Elastic (QE) contribution shown in figure 2.6a. At these energies it is not possible to break a nucleon apart, but instead the neutrino can be considered to be interacting with an entire nucleon. This interaction is described by:

$$\nu_l + n \rightarrow l^- + p, \tag{2.23}$$

where l denotes one of the three lepton flavours. In these events the charged lepton would be observed, potentially along with the nucleon.

At intermediate neutrino energies ($\sim$ 1-5 GeV) there is a significant contribution from interactions which proceed via a resonant state, as shown in figure 2.6b. These resonant states then decay to nucleons by emitting a single pion. In this case it is likely that if a charged pion is produced it will be detected in addition to the charged lepton. Above these energies the dominant interaction mode is Deep Inelastic Scattering (DIS) in which the neutrino interacts with an individual quark, breaking the nucleon apart and generally resulting in multiple particles being produced.

Interactions with free nucleons are relatively easy to understand. However, as all current and planned experiments use larger nuclei as targets the effects of the rest of the nucleus on both the target nucleon and outgoing particles must also be understood.

2.2.1 Interactions with Nuclei

Unsurprisingly, the rest of the nucleus has significant effects on the interactions. These can be divided into two parts, the first alters the interaction cross-section itself, whereas the second affects the particles which leave the nucleus.

The nucleons within a nucleus are not at rest and the initial state movement is known as Fermi motion. The motion of the individual nucleon is unknown for a given interaction and this motion provides a boost to the event in the lab frame. Spectral functions are models used to describe this motion and one commonly used example is the Relativistic-Fermi-Gas (RFG) model [30] in which the nucleons behave as an ideal gas of fermions which move freely within the nucleus. Due to Coulomb repulsion, protons and neutrons will behave differently. The result of this is that the potential
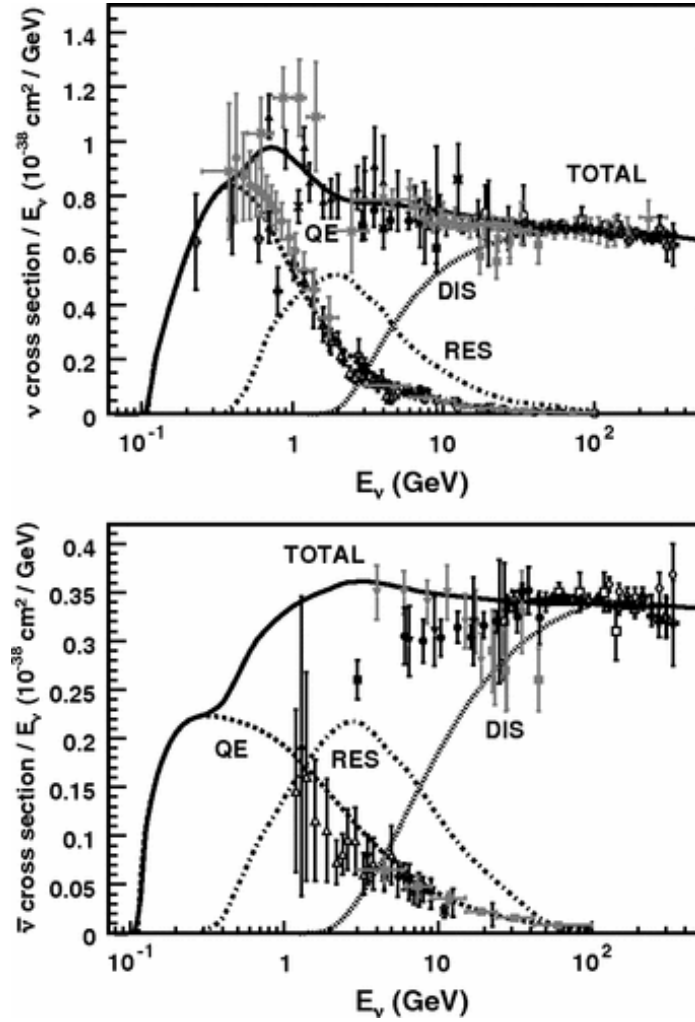
Figure 2.5: Charged current cross section measurements for ν_μ (top) and $\bar{\nu}_\mu$ (bottom) as a function of neutrino energy [29]. The total cross section is broken down showing the contributions from Quasi-Elastic (QE), resonant (RES) and Deep Inelastic Scattering (DIS). The curves show the theoretical predictions and the data points show a range of experimental results. The values shown are per nucleon for an isoscalar target.
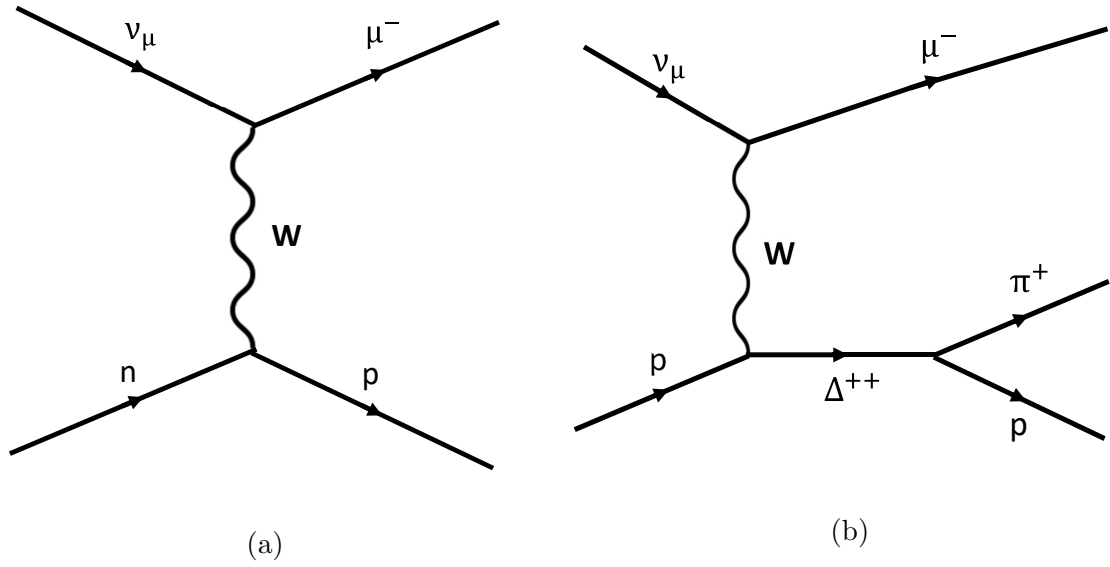
Figure 2.6: Feynman diagrams for CCQE (a) and resonant pion production (b).

well for protons is shallower than that for neutrons, as shown in figure 2.7. With the nucleus in the ground state, all energy levels are filled up to the Fermi momentum, p_f. This means that for an interaction to occur a nucleon must be excited to a state above this momentum, a process known as Pauli blocking. This reduces the phase space and therefore the cross section. The simplest implementation of a RFG model assumes a constant density within the nucleus, resulting in a constant p_f, something known to be incorrect from electron scattering measurements [31] however local Fermi gas models account for non-uniform density within the nucleus. The value of p_f as a function of radial distance within the nucleus is shown in figure 2.8 for global and local Fermi gas models. The drawback of these models is that nucleons are still treated as non-interacting.

Assuming that nucleons are non-interacting is overly simplistic, as through electron scattering data nucleon-nucleon interactions are known to alter the initial nucleon kinematics significantly [32] [33]. Corrections can be made to help account for this. The high momentum tails shown in figure 2.8 are created by repulsive short range correlations and allow for momenta above the Fermi momentum [34]. Another way to expand the reactions we consider is to allow neutrinos to interact with a bound pair
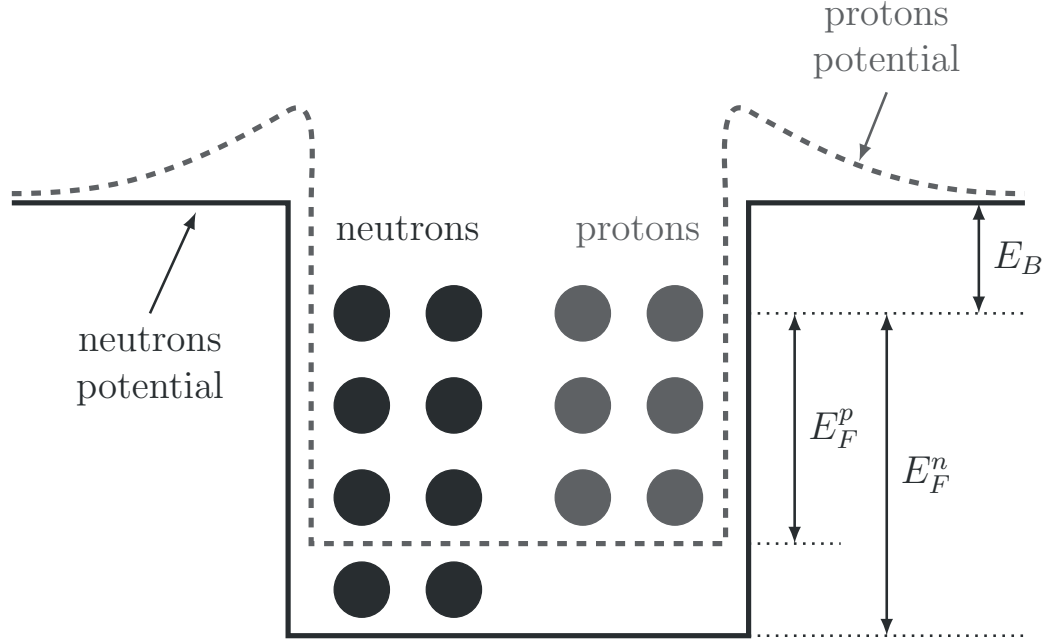
Figure 2.7: A schematic view of the potential wells for protons and neutrons within the nucleus. E_F^p and E_F^n are the Fermi energy for protons and neutrons respectively and the binding energy is given by E_B [37].

of nucleons [35] [36]. This produces two nucleons in the final state.

Before a particle produced in an interaction can be measured, it must first escape from the nucleus in which it is produced. Processes which alter the outgoing particle identities or kinematics are known as Final State Interactions (FSI). Each hadron is propagated independently from the interaction vertex through the nucleus in steps given by the particle's mean-free-path. During this the kinematic properties of the particle may change, as may the number and identity of the outgoing particles. A visual example of these processes is shown in figure 2.9. Details of the implementation of the models are described in [38][39][40].

Another correction which needs to be applied is the screening effect by the rest of the nucleus due to the effect it has on the electroweak propagator known as the Random Phase Approximation (RPA) [35] [36]. This produces a correction that is dependent on the 4-momentum transfer, Q^2.
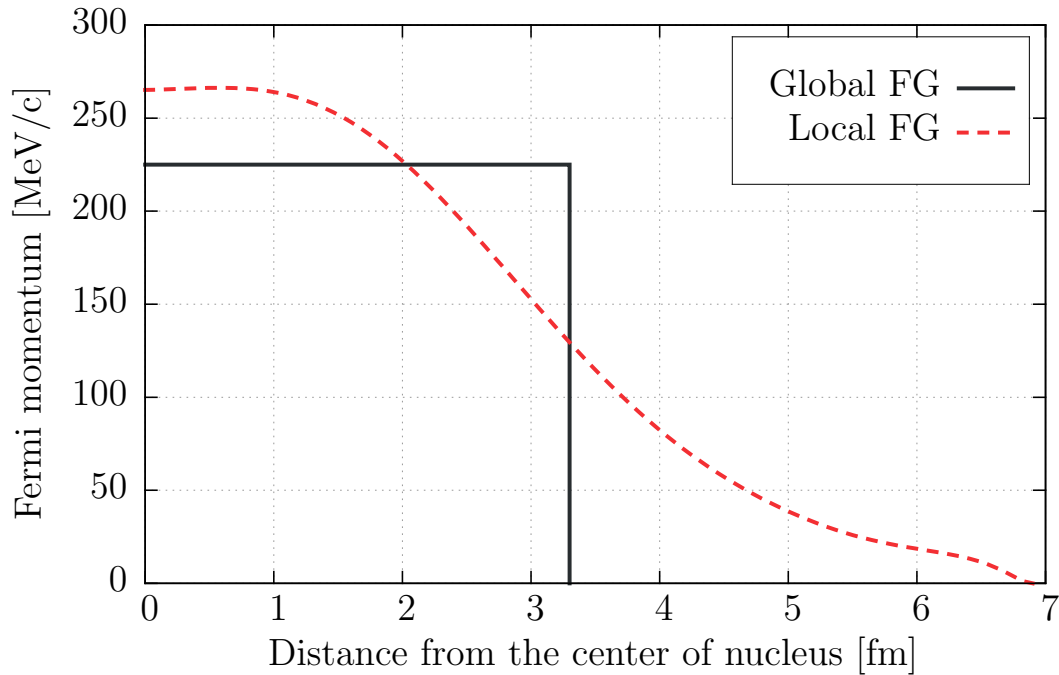
Figure 2.8: Fermi momentum as a function of radial distance within a carbon nucleus for 'global' and 'local' Fermi Gas (FG) models [37].

2.3   Open Questions

While many parameters have now been measured, there are still many questions about neutrinos left to answer. Many of these are the subject of current and the next generation of experiments. Some of the gaps in our knowledge are:

- Absolute neutrino mass:

  While neutrino oscillations are sensitive to mass squared differences between the three mass states, they provide no information about the absolute mass of neutrinos. There are a variety of methods which can be used to attempt to measure the absolute mass scale including cosmological measurements [41] as well as neutrinoless double beta decay searches [42] and measurements of the endpoint of the beta decay spectrum [43]. As yet the absolute mass is still unknown but with ever decreasing limits being set. A detailed overview of current measurements is given in [44].
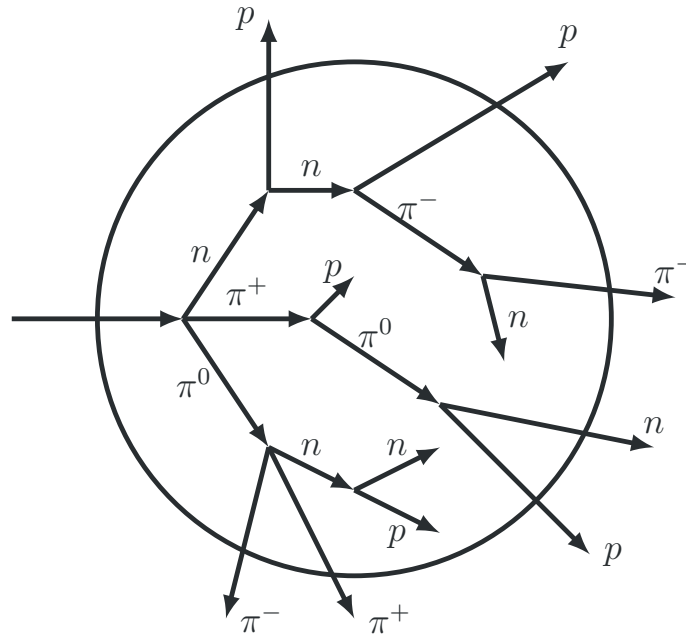
Figure 2.9: A visual example showing the effects of Final State Interactions [37]. These occur as particles propagate through the nucleus and affect the number and identity of the particles which can be detected as well as their kinematic properties.

- Mass ordering:

  Oscillation measurements provide the difference between the squared neutrino masses but the ordering of the masses is still possible through effects that occur when neutrinos pass though matter. The ordering of the first two mass states was determined from solar neutrino measurements but it is still unknown if the third mass state is above or below these two. In the case of quarks and charged leptons there are two light states and one significantly heavier state. For this reason, if the neutrino masses follow the same pattern it is known as 'normal ordering', and if the third state is significantly lighter it is known as 'inverted ordering'. The two possible mass orderings are shown in figure 2.10. It is expected that next generation long-baseline experiments will be able to measure the ordering within the next few decades, which will improve our understanding greatly as many parameters differ depending on which ordering is assumed
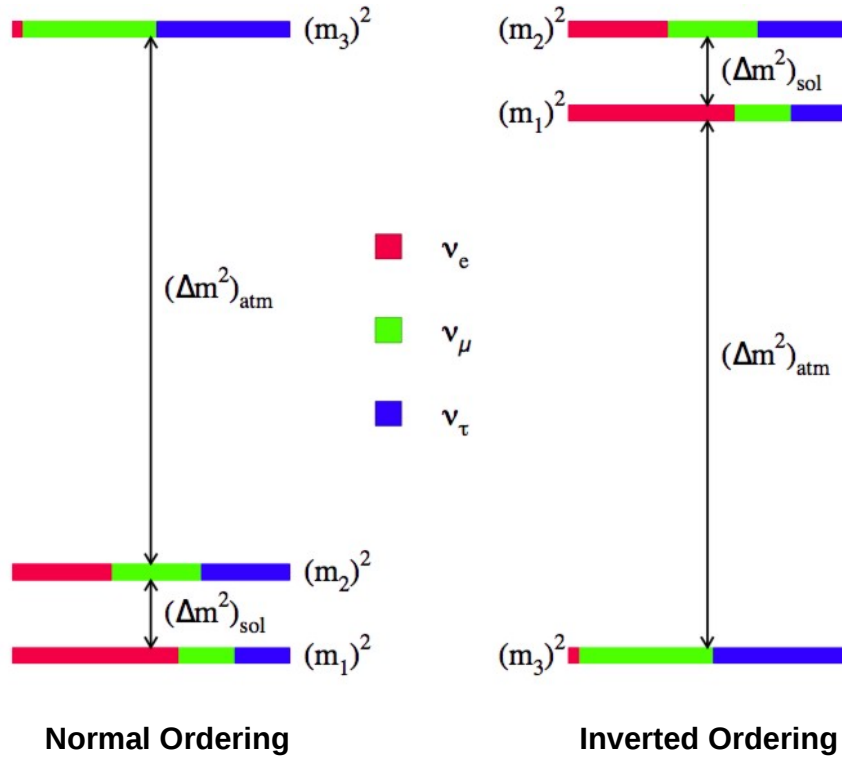
Figure 2.10: A visual representation of the possible mass orderings where Δm^2_{21} and Δm^2_{32} are shown as Δm^2_{sol} and Δm^2_{atm} respectively. Figure adapted from [45].

as shown in table 2.1. Recent T2K results show a preference for the normal neutrino mass ordering at the 2σ level [28], rising to $3\ \sigma$ when combined with NOVA and atmospheric results from SK.

- Dirac or Majorana?

  All fundamental fermions in the Standard Model, other than neutrinos, are known to have distinct particles and antiparticles. Particles such as these are known as Dirac particles. Due to their lack of electric charge it is possible that neutrinos and antineutrinos may not be distinct making them Majorana particles. This can be tested by searching double beta decays in which no outgoing neutrinos are produced. Double beta decay is observable when a given nucleus cannot energetically undergo a single beta decay but could undergo two simultaneously and is a known phenomenon, first observed in 1950 [46]. During
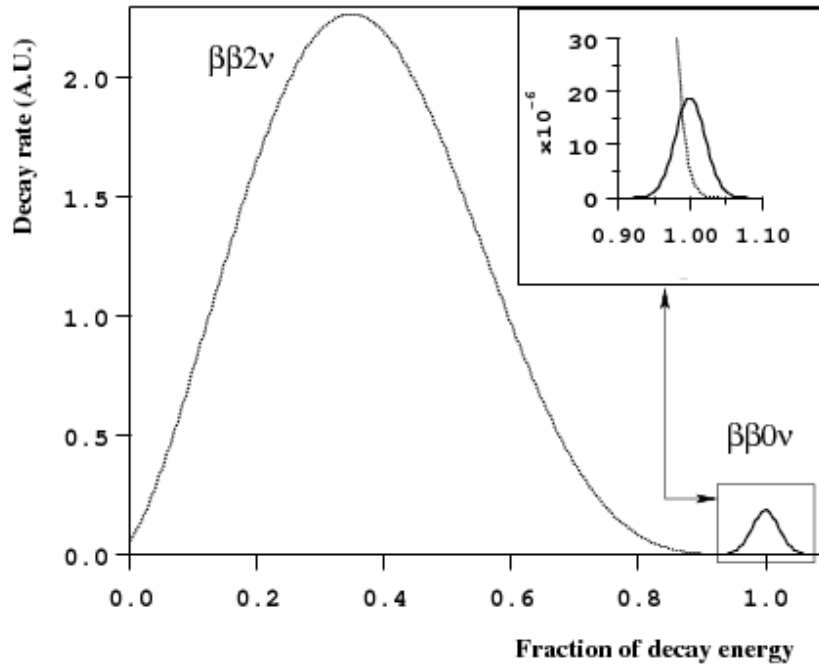
Figure 2.11: An example spectrum for outgoing electron energies for both two-neutrino and neutrinoless double beta decays. The main plot shows an exaggerated number of neutrinoless double beta decay events, with a more realistic signal shown in the insert [47].

this process much of the energy is carried away by the neutrinos however in the neutrino-less equivalent this is not the case and all energy would be given to the electrons. The relative electron energy spectra for both 2ν and neutrinoless double beta decay are shown in figure 2.11.

- Sterile neutrinos:

  Sterile neutrinos are additional neutrinos which do not couple weakly but could provide extra terms in oscillation equations. The first potential signal was observed by LSND as an excess of low energy ν_e events. Figure 2.12 shows allowed regions and limits from LSND [48], MiniBooNE [49], KARMEN [50], NOMAD [51] and ICARUS [52] as well as a global fit to all data sets. Recent results from MiniBooNE also show a significant low-energy excess at the 4.8σ level and 6σ level when combined with LSND results [53]. However, there are other ex-
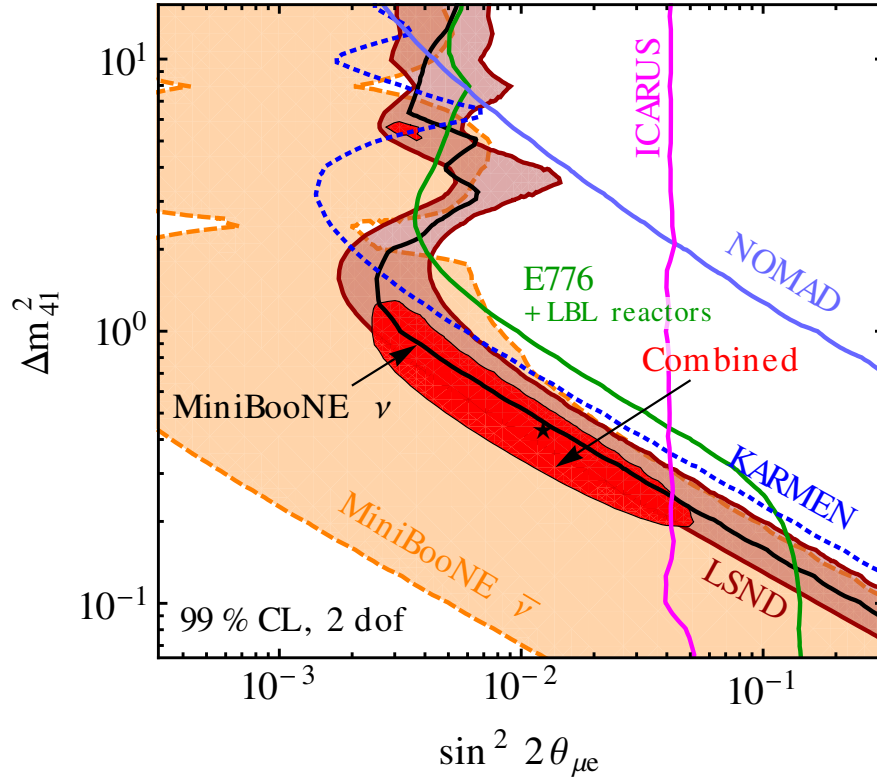
Figure 2.12: Allowed regions and limits at 99% CL for electron neutrino appearance measurements assuming a single sterile neutrino flavour. The red regions show the combined fit across all data sets with the best fit point marked by the star [57].

periments which do not agree with an excess in this region, such as MINOS+ [54].

The existence of sterile neutrinos is still very much an open question with experiments such as MicroBooNE [55] searching for the low energy excess seen by other experiments. The state of searches is described in [56].

Chapter 3

The T2K Experiment

The Tokai to Kamioka (T2K) experiment [18] is a long baseline neutrino oscillation experiment aiming to measure parameters of the PMNS matrix, described in section 2.1. This is achieved using measurements taken with neutrino and antineutrino beams, described in section 3.2.1. The experiment consists of a beamline and near detector complex located at the J-PARC facility in Tokai, on the east coast of Japan, and a far detector, Super-Kamiokande, 295 km away in the west of Japan as shown in figure 3.1.
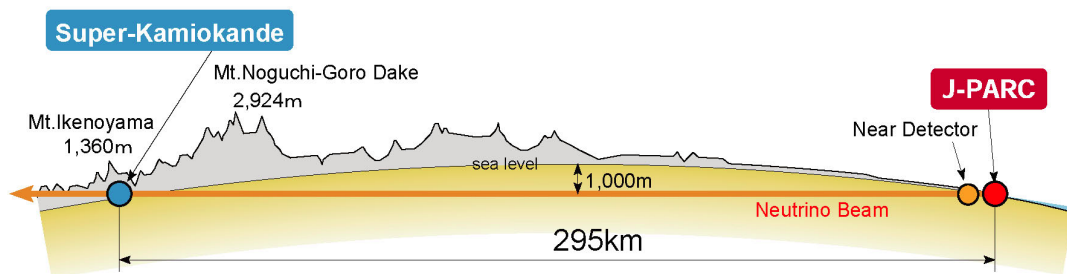
Figure 3.1: A schematic view of the T2K experiment [58].

The main aims of T2K are:

1. Measurement of θ_{13}

   θ_{13} is one of the three mixing angles in the PNMS matrix described in section 2.1 and is measured in T2K using electron (anti)neutrino appearance in a muon

(anti)neutrino beam. Before it was measured, it was assumed to be very small, if not zero. This would make it difficult to impossible to find CP violation through neutrino oscillations as the matrix elements containing δ_{CP} also contain a factor of $\sin\theta_{13}$ which would be small for small values of θ_{13}. Fortunately this was not the case. Not only was it found to be not zero, it was at the larger end of the allowed region [14] leaving the very real possibility for detecting CP violation. Some hints at this have been seen, however the 3σ range for the CP violating phase in the lepton sector, δ_{CP}, covers the full range of angles, as given by table 2.1. Reactor measurements are sensitive to θ_{13} through electron antineutrino disappearance but are not sensitive to δ_{CP} as this requires a cross generational transition.

2. Precision measurements of Δm^2_{23} and θ_{23}

   These parameters are measured using muon neutrino disappearance. Precise measurements are required as the uncertainties on these values affect the precision of other measurements, such as θ_{13}.

3. Measuring neutrino interaction cross sections

   The near detectors are used extensively for calculating cross sections using the unoscillated beam. The cross sections of some neutrino interaction processes are not well known, especially at the peak beam energy of T2K, and for the interaction materials used in the near and far detectors. The situation is even worse for antineutrinos. It is therefore important to measure cross sections using the near detectors. Measuring cross sections reduces the uncertainties on other neutrino measurements which benefits existing and future experiments as well as testing neutrino-nucleus interaction models. These models are not well known and their uncertainties limit the precision of current and future measurements.

The following sections describe the various parts of the T2K experiment in more detail and discuss the contribution from the NA61/SHINE experiment to the flux predictions for the T2K beam.

3.1   NA61/SHINE

The number of neutrino events produced by beam interactions is the product of the flux and cross section. As neutrino interactions have very small cross sections this makes it difficult to accurately measure the flux. In addition, large uncertainties on one result in large uncertainties on the other, making it difficult to increase precision. For this reason it is useful to find alternative ways to constrain the flux. This is often done by measuring particles that subsequently decay to produce the neutrinos as these are far easier to detect and have well known decay properties.

T2K uses measurements from the NA61/SHINE experiment to reweight the nominal MC predictions [1] [2]. NA61/SHINE is a fixed carbon target, hadron spectrometer with many detector components used from the NA49 experiment, including two superconducting magnets, four TPCs and two time-of-flight walls, as shown in figure 3.2. The aim is to measure the charged pions and kaons that emerge from the target when subjected to a proton beam of the same energy as that used by T2K. The results are separated by particle and binned in momentum and angle. This information is required when predicting the neutrino energy spectrum, as described in section 3.7. The particle identification is performed using the dE/dx values from tracks in the TPCs with help from the time-of-flight systems. The resulting 2D kinematic distributions are compared with the predictions, providing the reweighting factors.

The current results used to produce the T2K flux models are obtained from data taken with a thin target. Corrections are then applied to simulate the flux for the actual T2K target. As a result of this there are many sources of significant uncertainty, totalling around 10%. These include hadron interaction uncertainties, which are the dominant source of uncertainty for the T2K beam, as seen in figure 3.3. Recently, data has been taken with a replica of the T2K target which will be incorporated into the models reducing the flux uncertainties to around 5% [59].
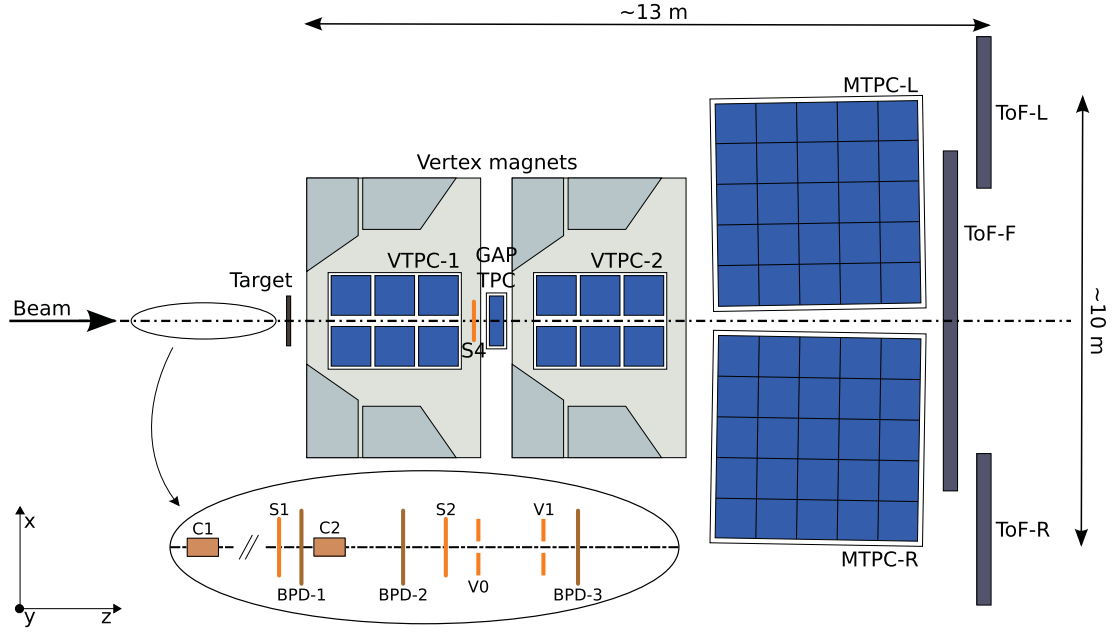
Figure 3.2: The layout of the NA61/SHINE experiment showing the incoming beam, Time Projection Chambers (TPCs) and time of flight (ToF) systems. Figure from [1]

3.2 J-PARC Accelerator Complex

The neutrino beam is produced by colliding 30 GeV protons with a graphite target [18]. This results in a shower of particles including charged pions and kaons which are focussed by magnetic horns, with the polarity determining whether the positively or negatively charged mesons are focussed. The horns are tuned to focus charged pions as these decay to produce a high purity muon (anti)neutrino beam. These mesons decay to charged leptons and neutrinos whilst moving through the decay volume. The branching ratios for the relevant decays are given in table 3.1. At the end of the decay volume is a beam dump which stops the remaining mesons and charged leptons. However some high energy muons pass through the beam dump and are detected by the muon monitor which measures the stability of the position and shape of the beam. As it is not possible to measure the neutrino flux directly at the start of the beam the number of Protons-On-Target (POT) is used instead as this is proportional to the number of neutrinos.

ND280: Neutrino Mode, ν_μ

(a)

ND280: Neutrino Mode, $\bar{\nu}_\mu$

(b)
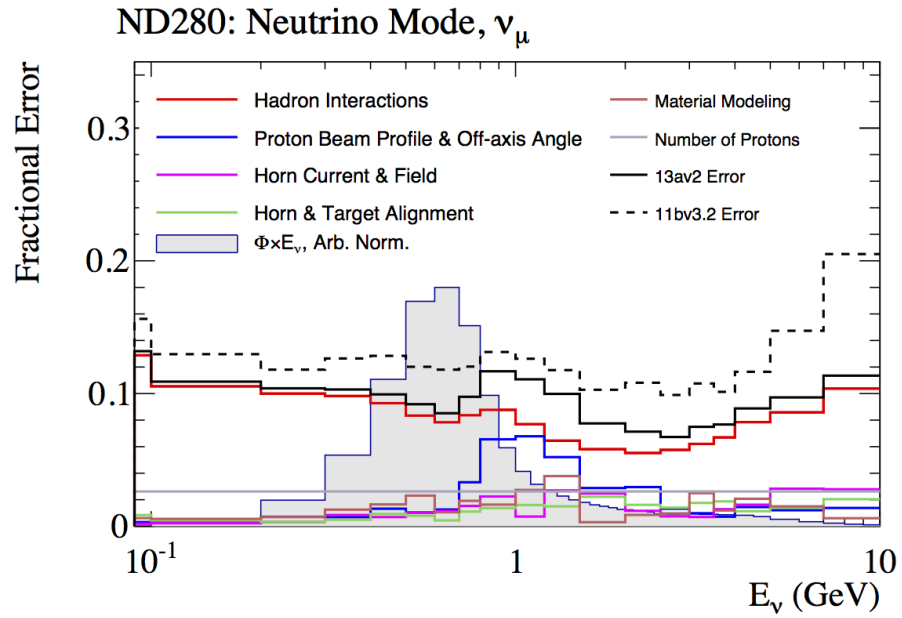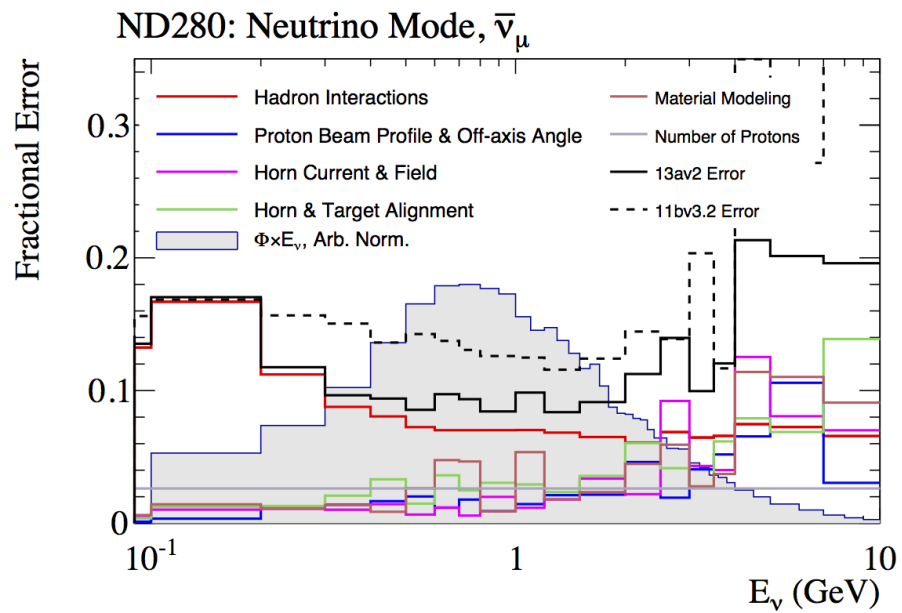
Figure 3.3: ν_μ (a) and $\bar{\nu}_\mu$ (b) flux uncertainties at ND280 broken down by source of uncertainty [60]. The solid and dashed lines show the total flux uncertainty for different flux tunings. The 13av2 tuning is used in this analysis.

Neutrino parent	Decay mode	Branching fraction
K^+	$\mu^+ + \nu_\mu$	63.56%
	hadrons	28.01%
	$\pi^0 + e^+ + \nu_e$	5.07%
	$\pi^0 + \mu^+ + \nu_\mu$	3.35%
π^+	$\mu^+ + \nu_\mu$	99.988%
	$e^+ + \nu_e$	0.012%

Table 3.1: Branching fraction for charged pion and kaon decays [61].
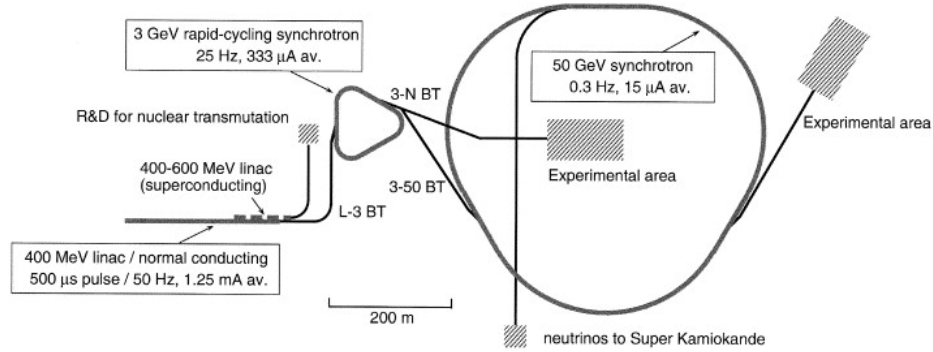
Figure 3.4: A schematic view of the accelerator complex at J-PARC [62].

3.2.1 Beamline

The protons are accelerated in three stages as shown in figure 3.4. First, a beam of H^- ions is accelerated by a liner accelerator (LINAC) to 400 MeV before passing through charge stripping foils which remove electrons to leave only protons. These protons enter the Rapid-Cycling Synchrotron where they are accelerated up to an energy of 3 GeV. Approximately 5% of these bunches are supplied to the Main Ring which accelerates them to an energy of 30 GeV. These are then extracted at the fast extraction point by five kicker magnets and passed into the neutrino beamline. Each T2K beam spill is composed of 8 bunches and has an associated GPS timestamp which is sent to each detector. This is used for triggering to remove continuous backgrounds, such as cosmic muons.

The neutrino beamline (figure 3.5) is broken down into two sections, the primary beamline (figure 3.6) directs the beam towards Kamioka and the secondary beamline (figure 3.7) consists of the graphite target and decay region in which the neutrinos

(1) Preparation section
(2) Arc section
(3) Final focusing section
(4) Target station
(5) Decay volume
(6) Beam dump
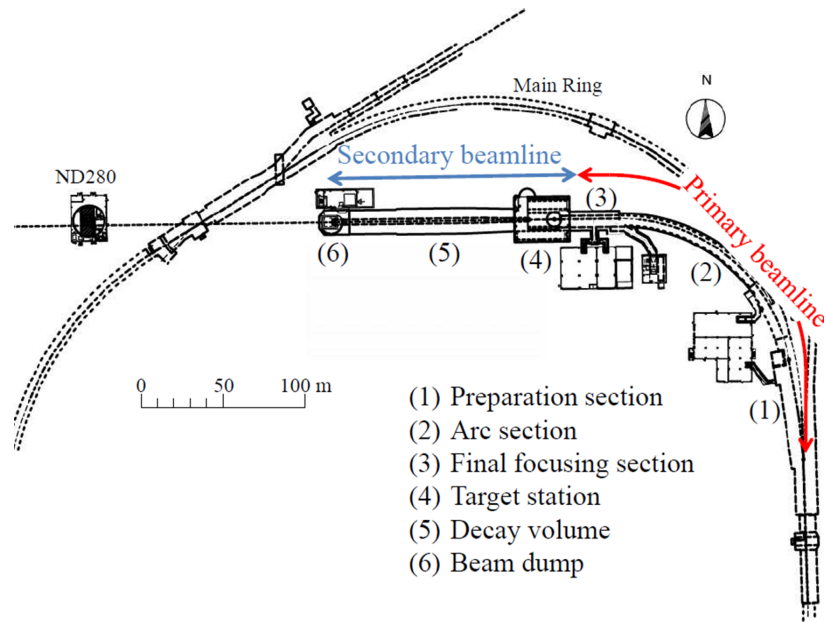
Figure 3.5: A view of the neutrino beamline showing the main components of the primary and secondary beamline as well as the location of the near detector complex [18].

Beam Monitor	Number
I : Intensity (CT)	5
C: Beam position (ESM)	21
P: Profile (SSEM)	19
P: Profile (OTR@target)	1
beam loss monitor	50
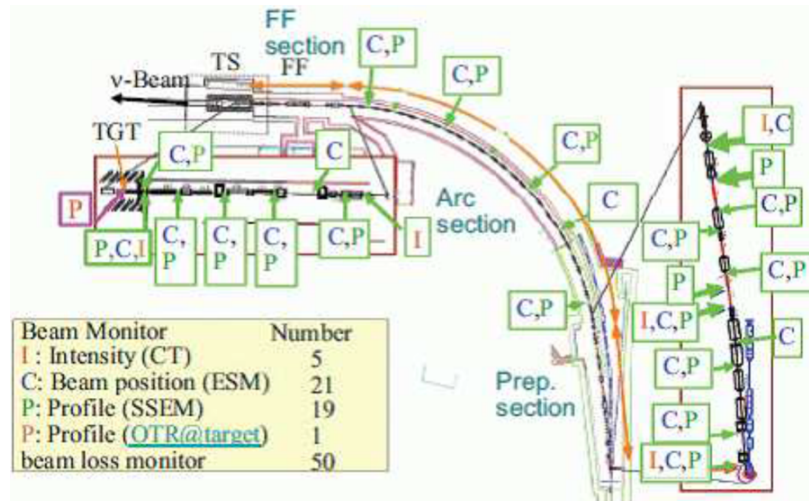
Figure 3.6: A more detailed view of the primary neutrino beamline, shown in figure 3.5, with the locations of the various beam monitors [18].
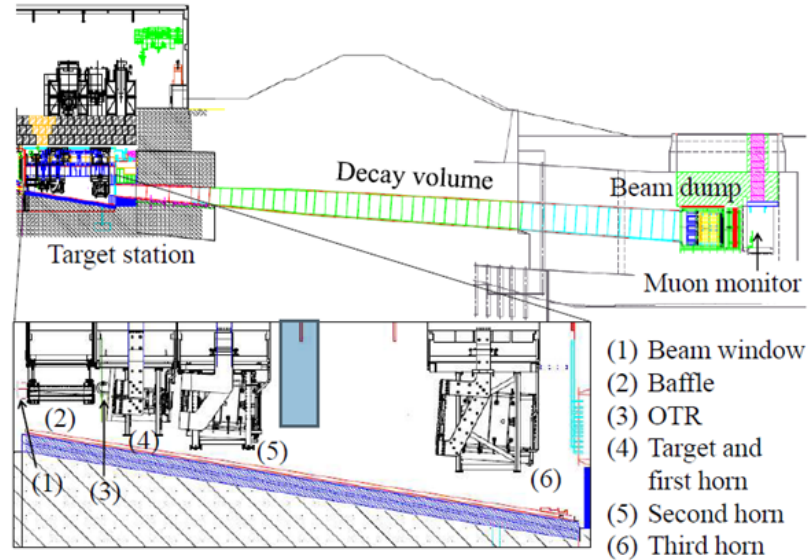
Figure 3.7: A more detailed view of the secondary neutrino beamline, shown in figure 3.5, with the locations of the major components marked [18].

are produced.

Neutrino Primary Beamline

The primary beamline itself can be considered as three further sections, as shown in figure 3.6. The first of these is the preparation section (54 m long), in which 11 normal conducting magnets steer and focus the proton beam such that it is accepted into the following arc section. Here the beam direction is changed by 80.7° over a distance of 147 m with a radius of curvature of 104 m. This is achieved using 14 doublets of superconducting magnets as well as 3 pairs of horizontal and vertical superconducting steering magnets for beam orbit correction. The last section is the final focussing section (37 m long) where 10 normal conducting magnets focus and steer the beam onto the target. They also direct the beam down by 3.637° relative to the surface of the Earth. Throughout this beamline there is extensive monitoring of the beam at locations shown on figure 3.6. The monitors used are:

1. Beam Intensity Monitor

The intensity of the beam is measured by five Current Transformers (CT) each of which is composed of a 50 turn coil around a ferromagnetic core. Each CT has a timing resolution of less than 10 ns and measures the absolute intensity with an uncertainty of 2% and the relative intensity with an uncertainty of 0.5%.

2. Beam Position Monitor

   Electromagnetic Monitors (ESM) are composed of four segmented cylindrical electrodes and determine the position of the beam through the asymmetry of the current induced on the electrodes. The ESMs measure the beam position to within 450 μm.

3. Beam Profile Monitor

   The beam profile is measured by Segmented Secondary Emission Monitors (SSEM) composed of two titanium foils stripped horizontally and vertically either side of a HV anode foil. Secondary electrons are emitted from the strips when hit by protons. These induce currents on the strips which are used to reconstruct the profile of the beam. As these monitors cause a small amount of beam loss (0.005%) they are inserted only during beam tuning.

4. Beam Loss Monitor

   Each Beam Loss Monitor (BLM) consists of a wire proportional counter filled with a mixture of argon and CO_2. If the signal across a given spill exceeds a threshold a beam abort interlock is triggered.

Neutrino Secondary Beamline

The secondary beamline is separated from the primary beamline by the beam window which consists of two He-cooled, 0.3 mm thick titanium alloy sheets. This is required as the primary beamline is kept under vacuum whereas the secondary beamline contains He gas at 1 atm. The secondary beamline begins with the target station. Within this there is the baffle, a graphite block with a very narrow hole (30 mm diameter) for the beam designed to admit only a very collimated beam to protect the magnetic

horns. Just before the target is an Optical Transition Radiation monitor (OTR) to measure the profile of the beam impacting on the target [63]. The OTR consists of a thin titanium alloy foil at 45° to the beam. As the protons pass through the foil visible light is produced which is reflected at 90° to the beam direction and collected to produce an image of the beam profile.

The target is a graphite cylinder, 91.4 cm long and 2.6 cm in diameter with a density of 1.8 g/cm^{-3}. The target material was chosen to be able to withstand the energy deposited by the beam. Outside this is a 2 mm thick graphite tube and 0.3 mm thick titanium case with He gas passing through the gaps between layers as coolant. The charged particles produced by interactions in the target are focussed by three magnetic horns, each with two coaxial conductors that produce a toroidal field with strength proportional to 1/r. A current of 250 kA produces a magnetic field that results in a 16 fold increase in flux at the far detector. The horns are run in either Forward Horn Current (FHC) mode, to produce a largely ν_μ beam, or Reverse Horn Current (RHC) mode, resulting in a largely $\bar{\nu}_\mu$ beam. The composition for the two beam modes is shown in table 3.2. The increased contamination in the RHC beam arises due to differences in the hadron production yields described in [1].

The focussed particles decay in the following 96 m long chamber. The chamber is lined with 6 m thick concrete and along the beam axis are 40 plate coils through which water flows as coolant. The length of the decay volume was chosen to maximise the flux of ν_μ or $\bar{\nu}_\mu$, depending on the horn polarity, while also reducing the ν_e and wrong-sign contamination. The majority of ν_μ are produced in the decays of the initial mesons, however these decays also produce muons, which if allowed to continue would produce the other types of neutrino through the reaction $\mu^+ \to e^+ + \nu_e + \bar{\nu}_\mu$. The predicted flavour composition of the neutrino beam is shown in table 3.2 and as a function of neutrino energy in figure 3.8 for both FHC and RHC beam modes. The FHC beam had a higher purity due to the relatively larger number of positively charged mesons produced at the target [1].

The beam dump lies at the far end of the decay volume to stop the remaining charged particles. The core consists of 75 t of graphite which stops all but the most

	ν_μ	$\bar{\nu}_\mu$	ν_e	$\bar{\nu}_e$
FHC	92.6%	6.2%	1.1%	0.1%
RHC	37.5%	60.1%	1.4%	1.0%

Table 3.2: The neutrino flavour composition for FHC (neutrino) and RHC (antineutrino) beam modes [64].

(a)

(b)
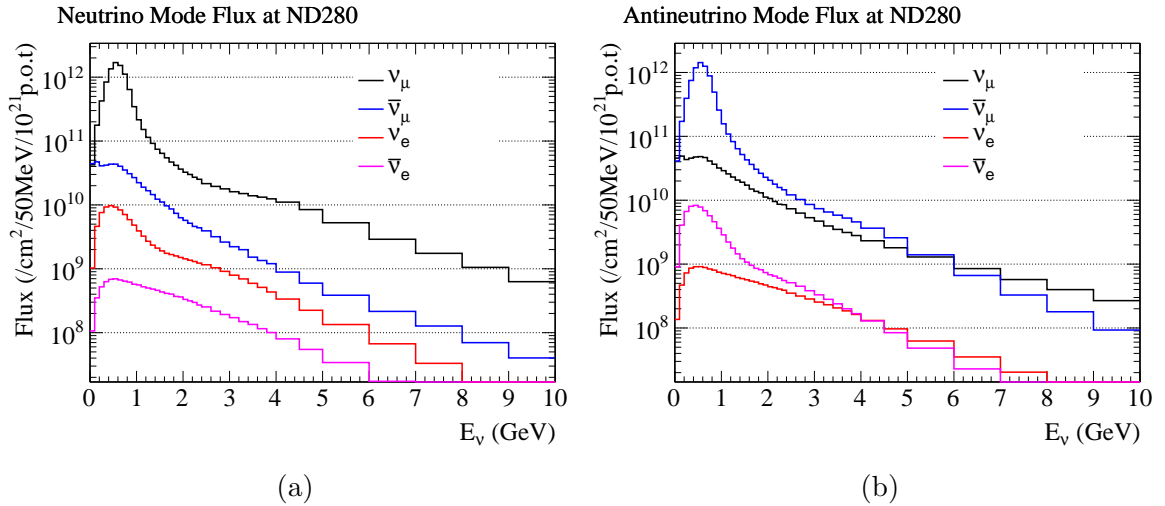
Figure 3.8: Neutrino flavour composition as a function of neutrino energy for FHC (a) and RHC (b) beam modes [65].

energetic muons (> 5 GeV). These muons are detected by the muon monitor which measures the intensity of the beam to a precision of 3% and the direction to within 0.25 mrad.

3.3   Near Detectors

Located 280 m downstream of the beam target are the two near detectors, the Interactive Neutrino GRID (INGRID) and ND280. INGRID is centred on the beam axis, whereas ND280 is 2.5° off axis, in line with Super-Kamiokande. These detectors measure the neutrino energy and flavour content of the unoscillated beam as well as a wide variety of neutrino interaction cross sections. INGRID also measures the flux and position of the beam axis, ensuring that the off-axis angle of the remaining detectors is accurately known. These results are used to calculate the expected

neutrino flux and energy spectrum, assuming no oscillations, at the far detector and constrain backgrounds for oscillation analyses, such as the intrinsic electron neutrino contamination of the beam.

3.4   INGRID

INGRID is located 280 m downstream of the beam target and is centred on the beam axis [66]. It provides daily measurements of the position of the beam centre and intensity as a function of off-axis position. The beam position is measured to within 10 cm, equivalent to a precision of 0.4 mrad. INGRID is composed of two sets of seven identical modules arranged in a cross and two other, off axis modules, as shown in figure 3.9. The modules are constructed from 9 layers of 6.5 cm thick iron and 11 layers of scintillator. Each scintillator layer is composed of an array of 24 horizontal bars followed by an array of 24 vertical bars. The scintillator bars have a rectangular cross section of size 1 cm $\times$ 5 cm and are composed of polystyrene with a titanium oxide coating. There is no iron layer between the last two scintillator layers due to weight restrictions, with the weight of iron per module at 7.1 tons. In addition to these layers, on the sides of each module are veto planes, allowing particles originating outside the module to be identified. As veto planes between modules can be shared each module has either three or four veto planes depending on its location.

There is a further, 'proton', module positioned upstream of the central modules. In the other modules most particles other than muons are stopped by the layer of iron following the interaction vertex and therefore do not produce tracks. The proton module is composed entirely of scintillator, using a combination of the same bars used in the other INGRID modules and 1.3 cm $\times$ 2.5 cm bars to improve resolution [67]. It is designed to measure the muons and protons coming from charged current quasi-elastic (CCQE) interactions.
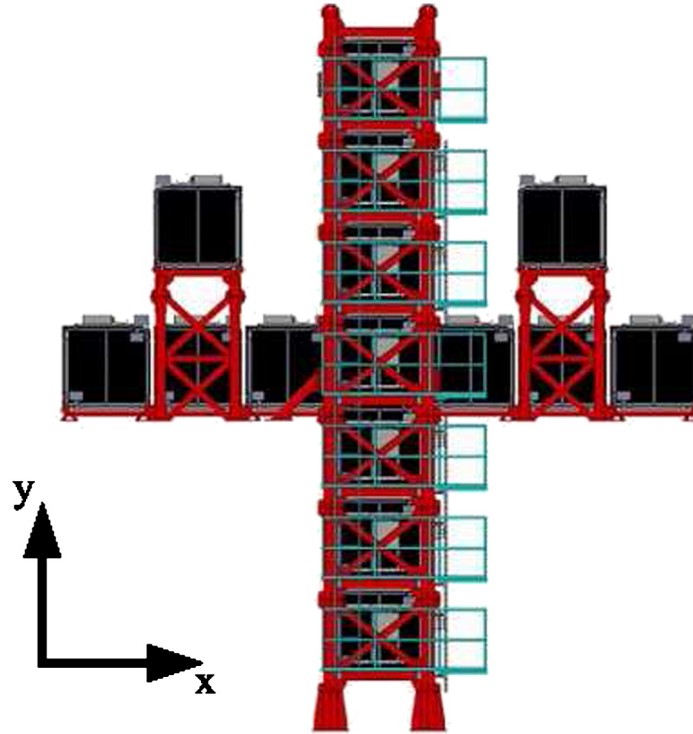
Figure 3.9: The INGRID detector, showing the 14 modules arranged in a cross, such that the beam passes through the two overlapping central modules, and the two separate off-axis modules [18].

3.5 ND280 Off-axis Detector

ND280 is the off-axis near detector, shown in figure 3.10, and consists of a Pi-zero Detector (P0D) and tracking region surrounded by Electromagnetic Calorimeters (ECals) and the magnet from UA1/NOMAD [18]. The tracker contains two Fine-Grained Detectors (FGDs), which act as an active target, and three Time Projection Chambers (TPCs), which identify particles and measure their momentum. The magnet yoke is instrumented with the Side Muon Range Detector (SMRD). ND280 aims to measure the unoscillated neutrino energy spectrum and flavour composition of the beam along the direction to the far detector as well as neutrino interaction cross sections.
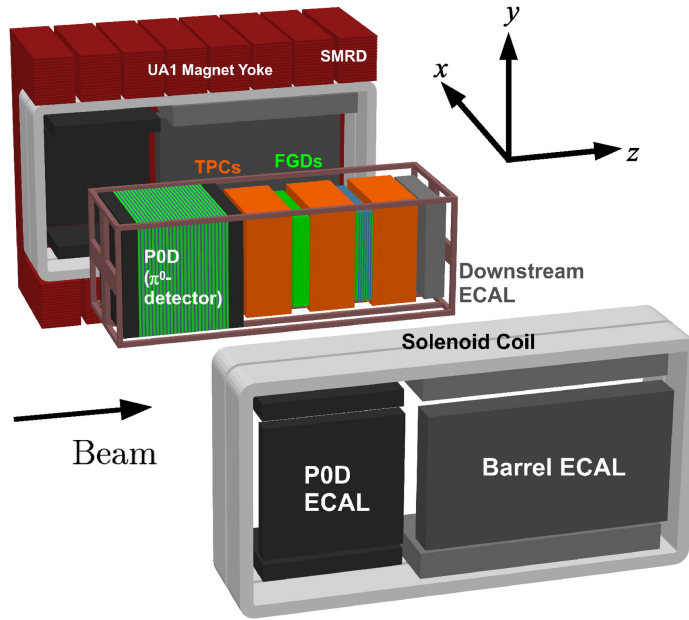
Figure 3.10: An exploded view of the ND280 detector, showing the five subdetectors and beam direction [18].

3.5.1 P0D

The P0D is designed to measure the rate of neutral current (NC) events in water in which a π^0 is produced [68]. This is a background to the ν_e appearance signal at the far detector.

The P0D is made up from four regions, moving from the upstream end they are the upstream calorimeter, upstream water target, central water target and central calorimeter. There are a total of 40 modules split between these regions and each module contains two perpendicular arrays of triangular cross sectioned scintillator bars.

The upstream and central calorimeters act both as containment for events within the P0D such as photons from the π^0 decays, and also as a veto for events not occurring within the P0D. Both ECals consist of seven modules layered with 4.5 mm thick lead sheets.

The water target modules alternate scintillator layers with 28 mm thick water bags followed by a 1.28 mm brass sheet. The upstream and central targets contain 13 and 12 modules respectively. The water bags can be used either empty or full and

once run in both states it is possible to use a statistical subtraction to extract the cross sections for events in water [69].

3.5.2   TPCs

The three TPCs are responsible for accurately measuring the momentum and identity of charged particles as well as determining the sign of the charge [70]. The TPCs have a double box design, as shown in figure 3.11. There is a central cathode in the Y-Z plane and copper strips at the edge, resulting in a uniform electric field running parallel to the magnetic field. The inner box is filled with gas composed predominantly of argon (95 Ar:3 CF_4:2 C_4H_{10}). As charged particles move through the TPC they ionise the gas. The electrons released drift away from the central cathode and are multiplied by micromegas at the walls to produce a signal. There are 12 bulk micromegas positioned on each readout surface, each of which is composed of 1728 pads. This design was chosen to combine practicality with reduced dead space between components, to maximise the sampling length of tracks. The information from these pads allows the position of the signal to be determined and this, in combination with timing information, allows 3D tracks to be reconstructed.

The TPCs are able to accurately reconstruct multiple tracks. The magnetic field within the detector causes the paths of charged particles to be curved. The curvature of the reconstructed tracks is used to calculate the momentum and charge of the particle. As it ionises the gas, the charged particle loses energy during its passage through the TPC. The rate of energy loss as a function of position is used, along with the momentum measurement, to identify the particle.

3.5.3   FGDs

The FGDs act as an active target with good spatial and timing resolution to accurately identify vertices and outgoing particles. They act as both a target mass for interactions to occur and also a tracker to detect the outgoing particles [71]. Neutrino interactions have very small cross sections meaning that the FGDs are required to have sufficient
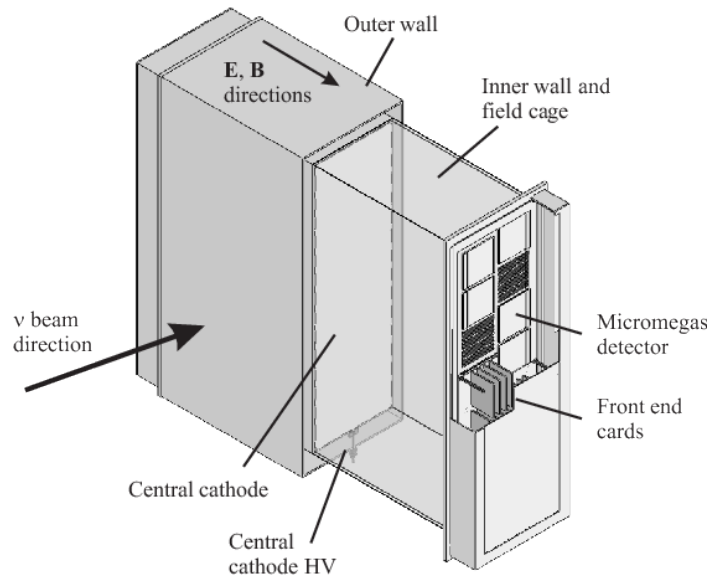
Figure 3.11: A cut away view of one of the TPCs, showing the major components. Figure from [18].

material for enough interactions to occur, however, as the best momentum and particle identification measurements are done by the TPCs we also require that the FGDs are thin enough such that most particles will escape from them. The main components of the FGDs are the extruded polystyrene scintillator bars (1 cm × 1 cm cross section) with a reflective titanium oxide coating, with a wavelength shifting fibre down the centre.

FGD1 is composed entirely of these scintillator bars, arranged in alternating horizontal and vertical layers. There are 15 pairs of these layers, with each layer containing 192 scintillator bars. For FGD2 there are only seven such pairs. Between each of these pairs there is a 2.5 cm thick water target. The water is kept below atmospheric pressure such that, if there is a leak, air is sucked in rather than water leaking out. Neutrinos entering FGD2 can interact with carbon and water, so using data from FGD1 it is possible to do a statistical subtraction and measure cross sections on water, which is useful for oscillation analyses as the same target material is used at the far detector [72] [73].

3.5.4 ECals

The P0D and tracking regions are surrounded by electromagnetic calorimeters on all but the upstream end. The P0D ECal surrounds the P0D and the barrel ECal (BrECal) surrounds the TPCs and FGDs. The downstream ECal (DSECal) covers the downstream end [74]. The purpose of these is to measure the energy of neutral particles exiting the tracking region, composed of the FGDs and TPCs. They also offer some amount of discrimination between particles that appears track-like and those which tend to form showers. They are also used to detect photons such as those produced by π^0 decays. The ECals are all composed of layers of lead and of scintillator bars with cross sections of 4.0 cm $\times$ 1.0 cm.

The barrel and downstream ECals have layers of scintillator bars in alternating directions and 1.75 mm thick lead sheets arranged with a single layer of scintillator bars between layers of lead. The downstream ECal has 34 such layers, each with 50 scintillator bars, with the first orientated with the bars lying along the X direction. For the barrel ECal the two orientations of the scintillator bars cover different lengths. There are 16 layers, including the one nearest the tracker, with the bars perpendicular to the beam direction alternating with 15 layers with the bars along the beam direction. The perpendicular bars are used to provide 3D reconstruction of tracks and showers which can be used to measure the identity of particles and the energy of electromagnetic showers.

The P0D is larger in the X-Y plane than the rest of the tracker and, due to the reduced space, the P0D ECal is thinner than the other ECals. There is only space for six layers, all bars of which run parallel to the beam direction, and in order to contain the electromagnetic showers the sheets of lead are 4 mm thick. The P0D ECal design can be different as it is not required to reconstruct 3D object but is used to check the containment of events originating in the P0D.

3.5.5   SMRD/Magnet

The other subdetectors are surrounded by the UA1/NOMAD magnet which provides a magnetic field of 0.2 T. The magnetic field causes the tracks produced by charged particles to be curved, allowing the momentum to be measured along with the sign of the charge. The magnet is formed in two halves which are placed together while taking data but can be opened for access to the inner subdetectors. Each half consists of iron sheets formed into eight c-shaped elements. Inside this structure there are two aluminium coils per magnet half, through which water is pumped as a coolant. One side of the magnet is shown in figure 3.10.

Due to its high density and size there will be many events which occur within the magnet. In addition to this there are events caused by cosmic muons entering the detector and also contributions from "sand muons", muons that originate from beam neutrino interactions in material not part of the detector. The magnet has 1.7 cm gaps between the iron sheets and as such it is possible to instrument it to veto these events. It can also help to track muons produced in the tracking region which exit the FGDs without passing through a TPC.

The SMRD is composed of scintillator modules that are placed in the gaps within the magnet elements, with the exact structure being location dependent to maximise the coverage. The top and bottom of all elements of the magnet yoke contain three modules whereas the sides vary with distance along the beam direction [75]. For elements 1-5 there are three modules, element six has four modules and the remaining two have six modules.

3.6   Super-Kamiokande

Super-Kamiokande (SK) is a water-Cherenkov detector [24] located 295 km from the beam target and is used for oscillation analyses by comparing the number of muon- and electron-like events with the predicted flux extrapolated from near detector data assuming no oscillations. The detector consists of an inner and an outer detector, separated by a cylinder which is lined with photomultiplier tubes (PMTs). The inner

volume has a height of 36.2 m and a diameter of 33.8 m and is instrumented by 11,129 50 cm diameter PMTs facing inwards. The cylindrical structure between the detectors is approximately 50 cm wide and consists of a stainless steel structure supporting plastic sheets, such that the regions are optically separated. The plastic facing the inner detector is black to absorb any photons that hit it whereas that facing the outer detector is highly reflective to compensate for the lower coverage by the PMTs and increase the number of photons detected. The outer detector extends approximately 2 m outwards from the support structure and is instrumented by 1885 20 cm PMTs facing outwards. The detector has a total height of 41 m and a diameter of 39 m.

At the peak beam energy of 600 MeV, charged current quasi elastic events dominate, in which an incoming neutrino exchanges a W boson with a neutron resulting in only an outgoing charged lepton and possibly a proton, given by:

$$\nu_l + n \to l^- + p, \tag{3.1}$$

where l is either an electron or muon. If the charged lepton is produced moving faster than the phase velocity of light in the water it will emit a cone of Cherenkov radiation which is detected by the PMTs. The refractive index of water is 1.33 and the threshold for Cherenkov radiation is at a relativistic gamma factor of 1.52; therefore, the energy required for electrons, muons and taus are 0.775, 160.6 and 2701 MeV respectively. The energy spectrum for T2K is strongly peaked at around 600 MeV which is far below the threshold for producing taus with the required energy to produce Cherenkov radiation.

The position and timing of hit PMTs is used to reconstruct the location and type of event. T2K is searching for muon (anti)neutrino disappearance and electron (anti)neutrino appearance in the predominantly ν_μ beam. In order to do this there must be good particle identification (PID) for events at SK. This is done by analysing the shape of the rings observed. Electrons will produce an electromagnetic shower through Bremsstrahlung and pair production, and as such there are many particles producing Cherenkov cones, therefore resulting in a diffuse ring shape, as shown in figure 3.12a. Muons, however, being much heavier, scatter less and produce a

(a) Electron-like ring   (b) Muon-like ring
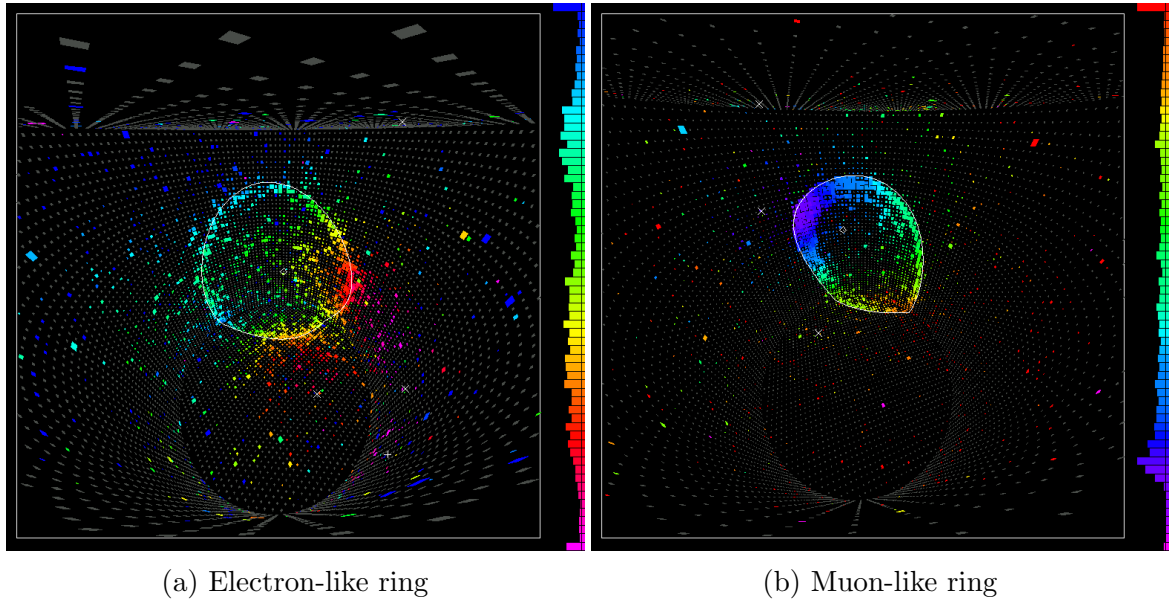
Figure 3.12: Event displays for (a) electron-like and (b) muon-like events. Each coloured point represents a hit PMT, where the colours show the relative timing of the hit, with blue hits being early and red being later [77].

sharp, well defined ring, as shown in figure 3.12b. The separation between muons and electrons is very good, with misidentification probabilities of 0.7% and 0.8% respectively [76]; however, other particles, such as neutral pions, can pose problems. They decay to two photons which can each produce an electron-like ring. If one of these ring fails to be reconstructed then it will mimic the signal expected from a ν_e interaction.

3.7 Meson Decays

The neutrino flavour composition and energy spectrum of the beam depends on the particles that decay within the decay volume, their momentum and the angle of the neutrino relative to the meson direction. Due to helicity conservation, pions decay almost exclusively to muons and muon neutrinos. However, due to their higher mass, kaons can decay to a three body state containing pions. The dominant kaon decay mode is still the two body decay to muons, but around 5% of decays produce electron neutrinos instead. The branching fractions for charged pions and kaons are detailed in

table 3.1. Kaon decays are the dominant source for the high-energy intrinsic electron neutrino contamination in the beam. Previous measurements of the pion and kaon yields using runs 1+2 [78] and runs 2+3 [79] found no significant discrepancies from the flux models based on the NA61 results described in section 3.1. This analysis fits the pion and kaon yields for FHC data including the larger run 4 data set in addition to runs 2 and 3 as well as performing a similar fit to RHC data in runs 5 and 6.

The energy of a neutrino produced in a two body decay is given by:

$$E_\nu = \frac{m_{\pi,K}^2 - m_\mu^2}{2(E_{\pi,K} - p_{\pi,K}\cos(\theta))}, \tag{3.2}$$

where $m_{\pi,K}, E_{\pi,K}, p_{\pi,K}$ are the mass, energy and momentum of the parent meson and θ is the angle of the emitted neutrino relative to the parent meson's path. Due to the mass differences we expect to get different neutrino energy spectra for each parent particle, which will also then vary differently with off-axis angle. When the neutrino is produced directly along the parent's path the neutrino energy increases linearly with parent energy. In the case where the neutrino is produced at an angle relative to the parent's path the dependence on parent energy is different. Now there is a maximum neutrino energy that can be achieved which depends on the mass of the parent and the off-axis angle. The neutrino energy as a function of its parent's energy is shown in figure 3.13 for charged pion and kaon decays with neutrinos produced at relative angles of 0° and 2.5°. This shows that in an off-axis beam, the low energy neutrinos arise predominantly from pion decays and higher energy ones from kaon decays. The result of this in the T2K beam is that the neutrinos produced by pion decays have energies strongly peaked around 600 MeV at 2.5° off-axis. However, due to the larger kaon mass, neutrinos from these decays have a much broader energy distribution and account for the high energy tail.

Reconstructed neutrino energy is not used in this analysis as it is highly model dependent and relies on identifying and correctly reconstructing all the final state particles. The true neutrino energy and reconstructed muon momentum distributions for FHC and RHC are shown in figures 3.14 and 3.15 respectively. The (anti)neutrino energy plots show the energy of (anti)neutrinos that produce true CC events in FGD1.
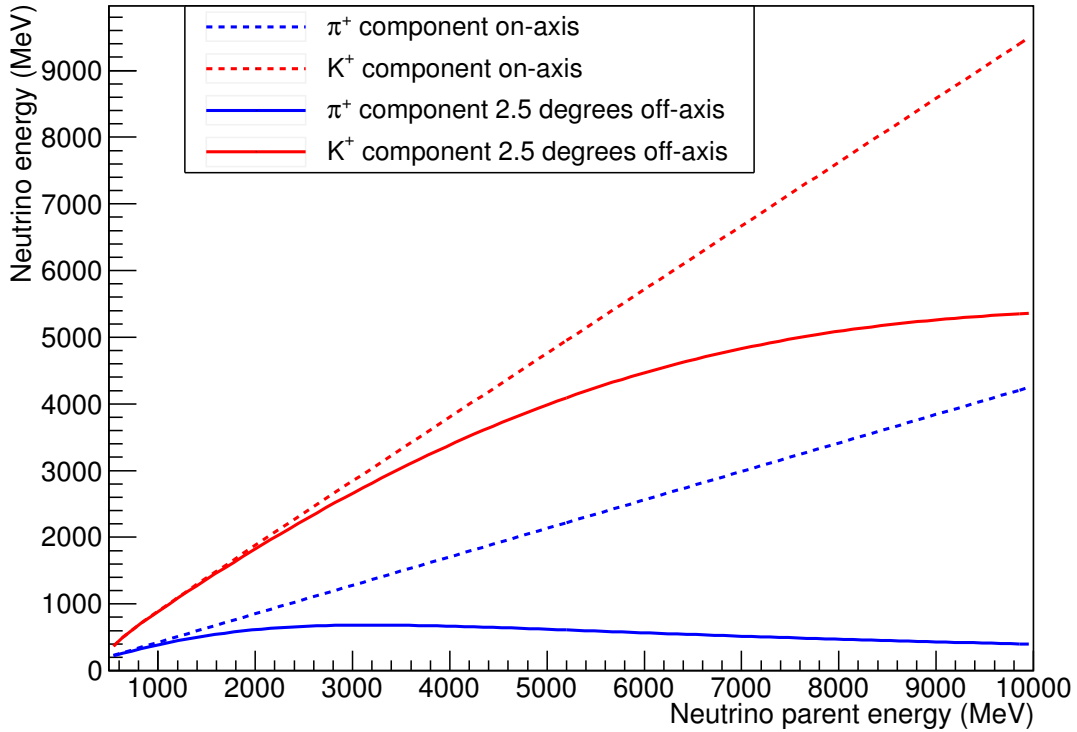
Figure 3.13: Neutrino energy as a function of neutrino parent energy shown for neutrinos produced in charged pion and kaon decays at angles of 0° and 2.5° relative to the parent's path.

In the RHC plot the two parts are divided into neutrino and antineutrino only plots. The reconstructed muon momentum distributions (figures 3.14 and 3.15, (c) and (d)) show the true CC events in FGD1 that pass the selection and all selected events respectively. These plots show that in the events that pass the selection given in section 4.1 the momentum of the muon shows good separation between the main neutrino parents.

As the off axis angle increases the flux decreases and the peak in the energy spectrum of the neutrinos occurs at lower energies, as shown in figure 3.16.
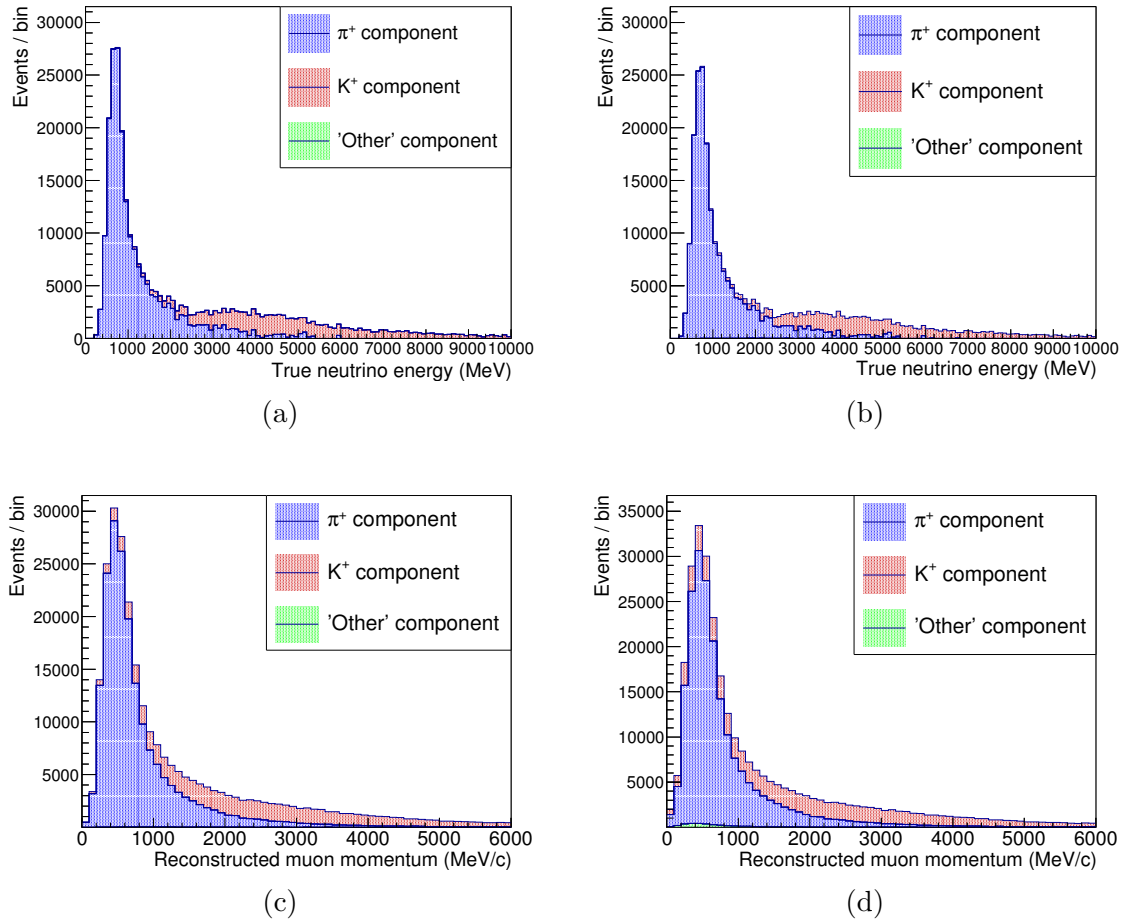
Figure 3.14: True neutrino energy in FHC for true CC events in FGD1 which (a) pass only the preselection cuts (cuts 1 and 2 of section 4.1) and (b) pass the full selection, given in section 4.1, separated by neutrino parent. (c) Reconstructed muon momentum for true CC events in FGD1 that pass the selections detailed in section 4.1 and (d) all events that pass the selection. The 'other' sample contains all events not contained by the remaining samples.
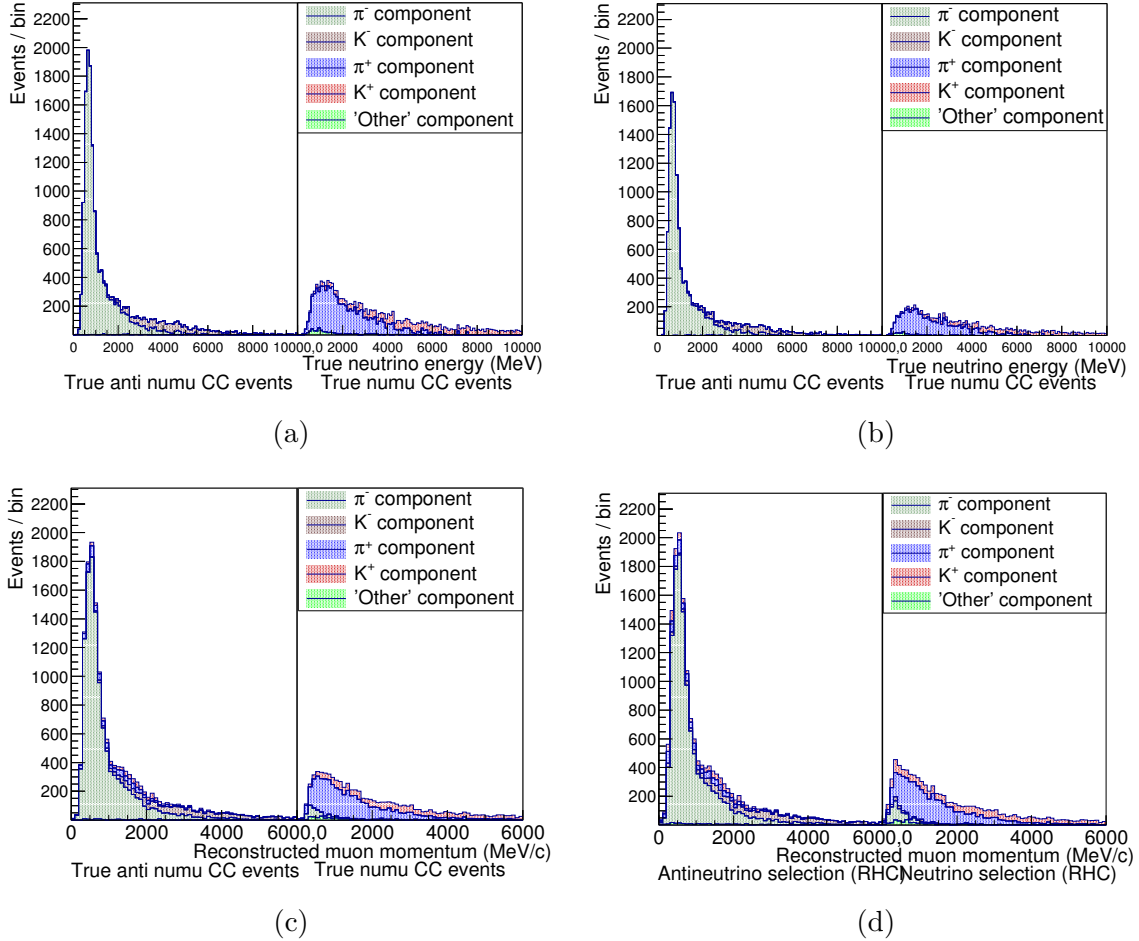
Figure 3.15: True neutrino energy in RHC for true CC events in FGD1 which (a) pass only the preselection cuts (cuts 1 and 2 of section 4.1) and (b) pass the full selection, given in section 4.1, separated by neutrino parent. The left side shows events from true antineutrino interactions and the right shows events from true neutrino interactions. (c) Reconstructed muon momentum for true CC events in FGD1 that pass the branched selection detailed in section 4.1 and (d) all events that pass the selection. There are some wrong-sign events that pass each branch of the selection due to the muon candidate being misreconstructed or misidentified. The 'other' sample contains all events not contained by the remaining samples.
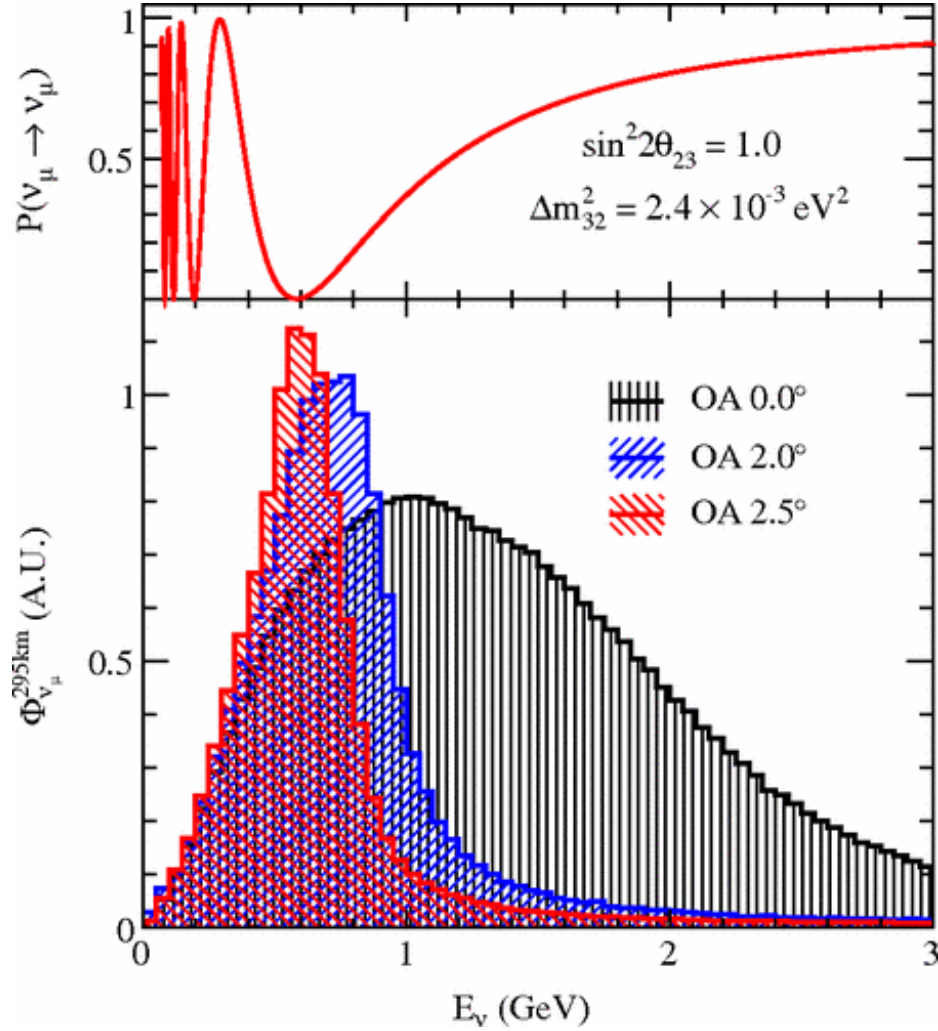
Figure 3.16: The expected neutrino flux as a function of energy for off-axis angles of zero (black), two (blue), and 2.5 (red) degrees respectively. Figure from [64]

3.8 T2K Future Plans

T2K has so far collected 3.0×10^{21} POT of an expected 7.8×10^{21}. Recent results [80] are beginning to suggest non-CP conserving values of δ_{CP} as well as favouring the normal mass hierarchy. There is also a proposal to continue running up to 20.0×10^{21} [81] increasing the statistics for the oscillation measurements significantly. The proposal also includes near detector upgrades, with the aim of reducing systematic uncertainties, as well as upgrades to the beamline, which will continue to be used for the Hyper-Kamiokande experiment [82].

This analysis aims to provide an *in-situ* cross-check of the hadron production

yields used in the T2K neutrino flux models, which is based on NA61/SHINE results. The results of this analysis are presented in section 7.

Chapter 4

Overview of the Neutrino Parent Analysis

External measurements by the NA61/SHINE experiment are used to constrain the neutrino flux for the T2K beam, as described in section 3.1. The current T2K flux model uses data collected with a thin graphite target, which is then corrected to account for differences due to the increased length of the T2K target as well as any mismodelling of other components, such as the magnetic horns. This leads to significant uncertainties, largely due to hadron interactions. The other difference between the targets used by NA61 and T2K is that over time the T2K target has received a much greater number of incident protons allowing the possibility of a change in performance. The target was designed for beam powers of at least 750 kW [18] which is significantly higher than the current beam power of around 500 kW meaning that any change in performance is unlikely but should be ruled out using data. This analysis provides an *in-situ* cross-check of flux models by measuring the number of observed events from neutrinos that are produced from different hadronic decays. The POT for each sample used in this analysis is given in table 4.1.

Hadronic decays responsible for producing the neutrino beam are described in section 3.7 which explains how different decays produce neutrinos with different energy distributions and flavour. As the intrinsic ν_e contamination and high energy neutrino interactions are large backgrounds to the ν_e appearance measurement it is important

Beam mode	Run	Data POT	MC POT	Run period
FHC	2	7.93×10^{19}	1.97×10^{21}	18/11/2010 - 11/03/2011
	3	1.36×10^{20}	9.60×10^{20}	08/04/2012 - 09/06/2012
	4	3.43×10^{20}	6.72×10^{21}	19/10/2012 - 08/05/2013
RHC	5	4.35×10^{19}	2.19×10^{21}	21/05/2014 - 26/06/2014
	6	3.42×10^{20}	1.31×10^{21}	01/11/2014 - 03/06/2014

Table 4.1: POT for all data and MC samples used in this analysis.

that the flux is well understood. Similar work has been performed by the NOVA experiment [83] which also uses external hadron production measurements to produce flux models [84]. The results show a 2.2% excess in neutrinos from pion decays and a 6.3% deficit from kaon decays relative to the nominal predictions. These results demonstrate the importance of performing independent tests of the flux models. This analysis uses the statistical separation seen in reconstructed muon momentum described in section 3.7 to determine the yields of the various neutrino parents.

4.1   Selection

This section describes the selections used during this analysis. This consists of a ν_μ CC inclusive selection for FHC running along with both ν_μ and $\bar{\nu}_\mu$ CC inclusive selections for RHC running. An inclusive selection is used in order to select events from all neutrino energies as the exclusive cross sections each dominate at different energies. FGD1 is used as the target for this analysis with TPC2 being used for momentum measurement and particle identification. FGD2 is not included in this analysis as it also contains water. Different cross sections result in changes to the muon momentum distributions meaning that it would be treated independently. Due to the higher uncertainties associated with the additional target material it is unlikely that FGD2 would significantly improve the result.

4.1.1 Neutrino Analysis

The FHC analysis is performed in FGD1 using the official T2K ν_μ CC inclusive selection [85]. This selection consists of six selection criteria and is described below.

1. Event quality

   The event must have a good data quality flag, meaning that it occurred within a time period covering a beam bunch and that each subsystem of the ND280 detector was operating correctly. This greatly reduces the chance of observing a cosmic muon or delayed signals from a previous bunch such as Michel electrons from muon decays.

2. At least one reconstructed TPC track

   We require at least one track to be reconstructed in the TPC following FGD1 (TPC2) as the tracks are more likely to be forward going. The TPCs are used to calculate the momentum and also for particle identification and are therefore necessary for this analysis. The TPCs are used for these measurements as the increased size and lower density allow for longer tracks and an easier measurement of track curvature.

3. TPC track quality and FGD1 fiducial volume

   The TPC track must pass through 18 TPC nodes. This is because the longer the track within the TPC the more accurately its momentum and identity can be determined.

   The Highest Momentum Negative Track (HMNT) must also have a reconstructed start position in the FGD1 fiducial volume, defined as: -874.51 mm $\leq x \leq$ 874.51 mm , -819.51 mm $\leq y \leq$ 929.51 mm, 136.875 mm $\leq z \leq$ 446.955 mm [85]. This volume is defined to reduce backgrounds from events originating outside the FGD. It is likely that the HMNT will be the muon as in CCQE interections no other negative particles will be produced and in other cases there will often be several particles, each with some fraction of the total energy.

4. TPC1 veto

   Events with a track in TPC1 are rejected. As particles are predominantly produced in the forward direction this largely removes events originating upstream of FGD1, including from the PØD, ECals and SMRD. Due to the largely forward-going nature of these events this cut has little effect on events originating in FGD1.

5. Broken track cut

   In order to remove events in which a single track is misreconstructed as two tracks, a cut is applied on the muon candidate start position if there is also a FGD-only track present. In this case the muon candidate track start position must be within 425 mm of the upstream edge of the FGD.

6. Muon TPC PID

   The TPC PID uses the rate of energy loss per unit length of the TPC track. For any given particle at the momentum measured we can calculate the expected dE/dx value. We then use this to calculate the pull by taking the difference between the measured and expected dE/dx values and dividing through by the error. The pulls, given by:

$$\mathrm{Pull}_i = \frac{dE/dx_{measured} - dE/dx_{expected,i}}{\sigma_{(dE/dx_{measured} - dE/dx_{expected,i})}}, \qquad (4.1)$$

   are calculated for muon, electron, proton and pion hypotheses and then combined to form likelihood variables, L_μ given by:

$$L_i = \frac{e^{-\mathrm{Pull}_i^2}}{\Sigma_l e^{-\mathrm{Pull}_l^2}}. \qquad (4.2)$$

   Cuts are applied to muon and Minimal Ionising Particle (MIP) likelihood variables, given by:

$$L_\mu > 0.05 \qquad (4.3)$$

and L_{MIP} given by:

$$L_{MIP} = \frac{L_\mu + L_\pi}{1 - L_p} > 0.8, p_{HMNT} < 500 \text{ MeV/c},$$ (4.4)

where p_{HMNT} is the momentum of the highest momentum, negatively charged track [86]. The efficiency and purity of this selection are given in table 4.2.

4.1.2 Antineutrino Analysis

The antineutrino selection contains a larger background from wrong-sign events. This is due to the higher wrong-sign flavour contamination of the beam and the larger neutrino cross section compared to antineutrinos meaning that other neutrino parents make up a significant number of events. The neutrino selection can be used to help constrain these samples by using a branched selection. This is composed of the official ν_μ background and $\bar{\nu}_\mu$ CC inclusive selections for the reverse horn current mode detailed in [87] and [88] respectively. The are both based heavily on the selection detailed above using all the cuts described with the sign of the charge swapped for the anti neutrino selection. The same cuts are used as each branch of the selection is still aiming to identify a muon track. Following these steps the selections branch with a final cut which requires the muon candidate track to have the correct charge. This cut guarantees exclusivity between the two branches of the selection.

The TPC PID cut also differs slightly for these selections. The requirement for the $\bar{\nu}_\mu$ selection is given by:

$$0.1 < L_\mu > 0.7$$ (4.5)

and:

$$L_{MIP} = \frac{L_\mu + L_\pi}{1 - L_p} > 0.9, p_{HMNT} < 500 \text{ MeV}.$$ (4.6)

The requirement for the RHC ν_μ selection is given by:

$$0.1 < L_\mu > 0.8$$ (4.7)

Selection	Efficiency	Purity
ν_μ (FHC)	53.5%	89.7%
ν_μ (RHC)	55.1%	80.0%
$\bar{\nu}_\mu$ (RHC)	66.4%	81.3%

Table 4.2: Efficiency and purity of the FHC and RHC selections.

and:

$$L_{MIP} = \frac{L_\mu + L_\pi}{1 - L_p} > 0.7, p_{HMNT} < 500 \text{ MeV}. \tag{4.8}$$

The efficiency and purity of this selection are given in table 4.2.

Chapter 5

Fitting Method and Systematics

This chapter details the methods used in performing the analyses described in chapter 4. This includes a general description of the fitting method used and systematic uncertainty generation and propagation as well as differences between FHC and RHC analysis methods.

For a given event it is not possible to determine the particle which decayed to produce the neutrino. However, due to the separation seen in the muon momentum distributions in figures 3.14 and 3.15 it is possible to perform a statistical fit to determine the number of events from different neutrino parents.

5.1   Fitting Method

The fit is performed by minimising the χ^2 distribution described by:

$$\chi^2 = \sum_{i=1}^{\text{NBins}} (\text{D}_i - \text{MC}_i) \text{V}_{ij}^{-1} (\text{D}_j - \text{MC}_j), \tag{5.1}$$

where V_{ij} is a covariance matrix containing the relevant systematic and statistical uncertainties, which are input into the fit which gives uncertainties on the final parameters, i and j denote the ith and jth bin respectively. These uncertainties are described in more detail in section 5.2. D and MC are the binned data and MC

distributions respectively. The MC distribution, described by:

$$MC_i = \sum_{\text{parents}} (f_{\text{parent}} \times \text{parent}_i), \tag{5.2}$$

is the sum of the distributions for each parent, parent_i, multiplied by a scaling parameter, f_{parent} which is varied during the fit. During the fit it is required that the normalisation parameters are free to move to avoid imposing a bias on the results. This is achieved by only using 'shape-only' uncertainties in the fit which allows some bin-to-bin movement and the overall normalisation to change freely. The shape-only matrices are used to allow the fit to freely change the normalisations of the different templates.

The matrices are produced using multiple toy MC samples to build up a smooth variation in the muon momentum distributions by varying the underlying parameters. The shape-only condition is satisfied by normalising each toy MC relative to the nominal MC. Each bin of the matrix is then given by:

$$V_{ij} = \frac{1}{N_{toys}} \sum_{n=1}^{N_{\text{toys}}} \frac{N_i^n - N_i^{nom}}{N_j^n - N_j^{nom}}, \tag{5.3}$$

where N^n is the renormalised toy MC and N^{nom} is the nominal MC.

During the fit, normalisation uncertainties are neglected. These are not applied to the fitted values in this analysis as a similar analysis performed in a different variable could result in significantly different uncertainties. The normalisation uncertainties are instead applied to each bin of the MC distribution. The fit and normalisation uncertainties are then added in quadrature to give the total uncertainty. The normalisation uncertainties to be applied in this way come from the flux, cross-section and final-state-interaction (FSI) systematics. The detector systematics are produced as shape-only by default and therefore do not contribute here.

The binning scheme chosen for FHC runs was such that the statistical uncertainties were a similar size to the various sources of systematic uncertainty. This was done to maximise the shape separation of the different neutrino parent distributions without compromising the total uncertainty. For the FHC selection, 10 muon momentum

bins were used with edges at 0, 300, 400, 500, 600, 750, 1000, 1400, 2000, 3200 and 6000 MeV.

The RHC data contains two selections each with fewer events than seen in the FHC selection. It is necessary to maintain good separation between neutrino parent contributions despite the decrease in the number of events. As a result, statistical uncertainties dominate in this analysis. The $\bar{\nu}_\mu$ selection uses 13 muon momentum bins with edges at 0, 350, 425, 480, 550, 625, 725, 850, 1050, 1350, 1700, 2200, 3200 and 6000 MeV whereas the ν_μ selection consists of seven muon momentum bins with edges at 0, 450, 750, 1100, 1500, 2100, 3100 and 6000 MeV.

5.1.1   Goodness-of-fit

When performed, the fit outputs a value for each parameter and a χ^2 value. From these, a p-value can be calculated, which is used as a measure of how likely the observed level of agreement is. This is done by running toy data sets, described in section 6.1, with parent scale factors set to the best fit values to generate a distribution of χ^2 values. The p-value is given by the integral of this distribution above the χ^2 per degree of freedom value given by the initial fit.

The fit for both FHC and RHC selections are tested using fake data samples described in section 6.2. The p values from these tests should be evenly distributed between zero and one. If there are significantly more than the expected 10% of these at extreme values (<0.05 or >0.95) it shows that the fit is performing badly.

5.1.2   Neutrino Analysis

The vast majority of events that pass the selection given in section 4.1 arise from either π^+ or K^+ decays with around 1% from other decays such as muons or neutral kaons. As these represent such a small fraction of the events, the fit lacks the sensitivity to measure them independently, therefore these samples are combined to form a single 'other' sample. The reconstructed muon momentum distribution broken down into these templates is shown in figure 5.1 for run 4. The distributions are similar for the
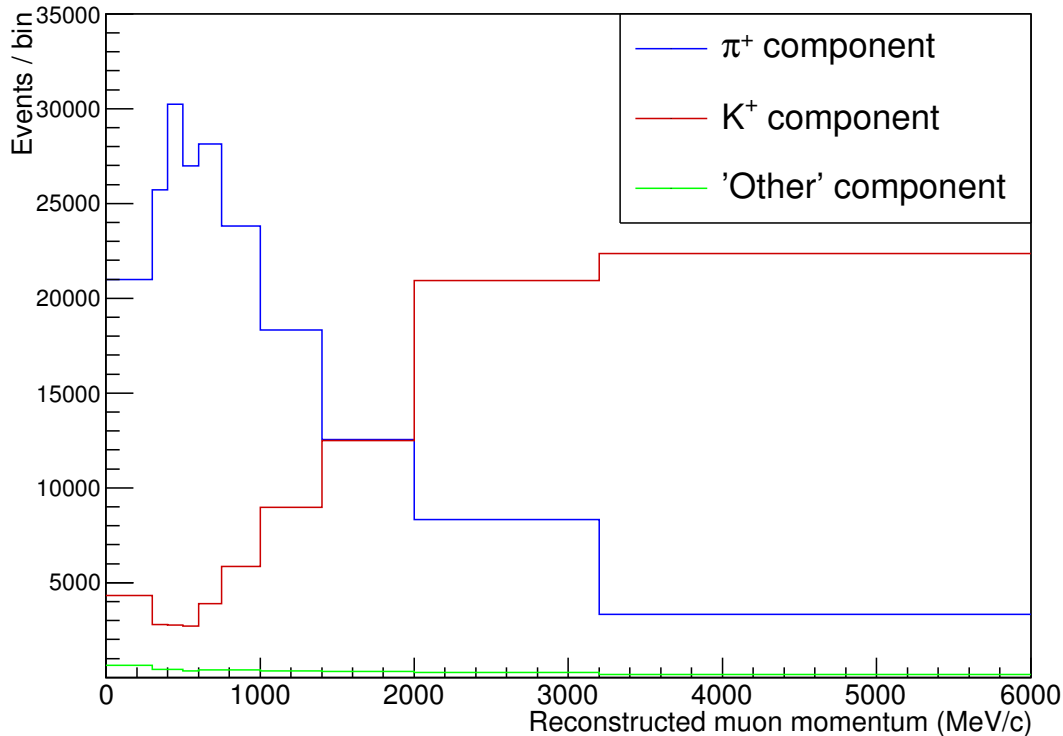
Figure 5.1: Distribution of muon candidate momentum for FHC run 4 MC (6.72×10^{21} POT of NEUT MC) separated by neutrino parent. The 'other' sample contains all events not included by the remaining samples.

remaining FHC runs, as shown in section 7.

5.1.3   Antineutrino Analysis

In RHC running there is a larger wrong-sign contamination to the neutrino beam which, combined with larger cross sections for neutrinos relative to antineutrinos, leads to more wrong-sign events being observed than in FHC running. The result of this is that both positive and negative pions and kaons produce significant fractions of the events. Events arising from other decays again contribute a very small fraction of the total number and are combined as done for the FHC analysis. The larger wrong-sign contamination made measuring the relative contributions more difficult. For this reason a joint ν_μ and $\bar{\nu}_\mu$ selection is used to help constrain the additional parameters. By using the joint selection, each of the four major templates has a distinct shape
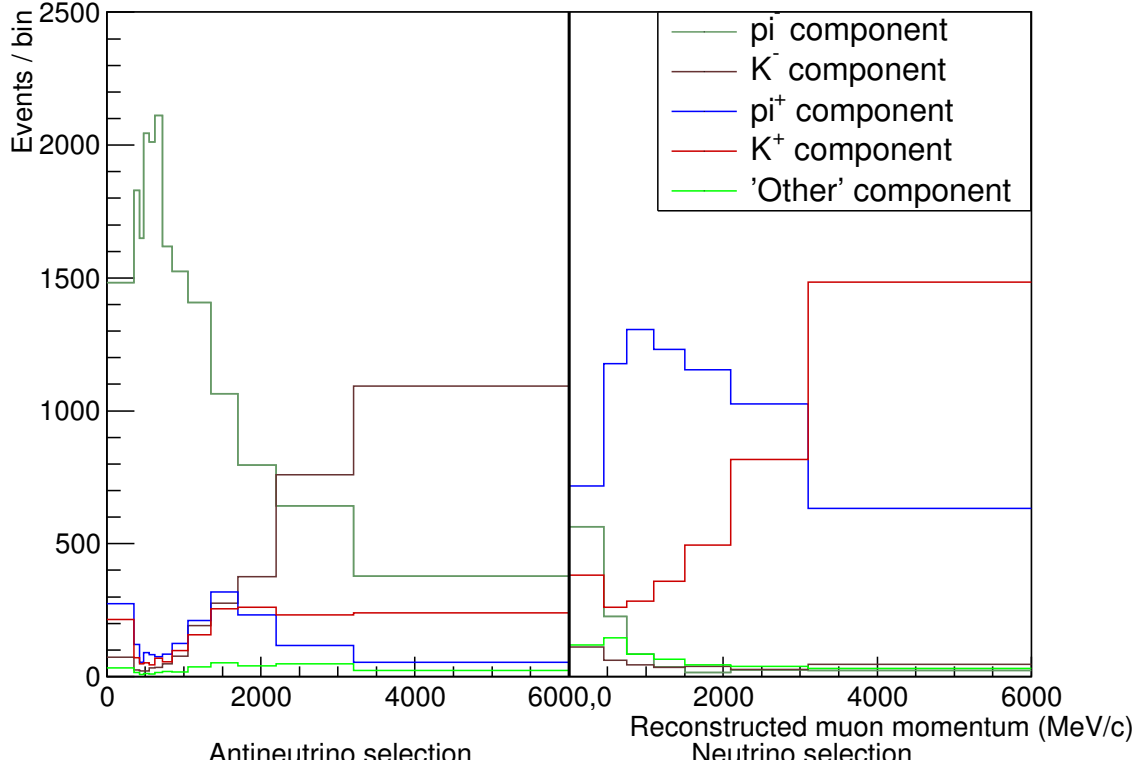
Figure 5.2: Distribution of muon candidate momentum for RHC run 5 MC (2.19×10^{21} POT of NEUT MC) separated by neutrino parent. The 'other' sample contains all events not included by the remaining samples.

and a simultaneous fit can be performed on all of them. The reconstructed muon momentum distribution broken down onto these templates is shown in figure 5.2 for run 5, with run 6 similar as seen in Section 7.

5.1.4 Merging runs

The statistical uncertainties can be reduced by combining data sets from different runs. This should provide the most powerful measurements of the neutrino parent yields. It is assumed that the yields are stable between runs which is tested by performing the fit to each run individually. When combining runs the MC samples for each run are scaled such that the POT ratio is the same as in the data samples. The MC distributions for each run are then used to convert the fractional covariance matrix for each run into an absolute covariance matrix. These matrices are added together

before being converted back to a fractional matrix for the combined MC. These steps make sure that any known changes between runs and systematic uncertainties are properly accounted for.

5.2 Error Propagation

The systematic and statistical uncertainties are be propagated through the fit as a covariance matrix. This is given by the sum of covariance matrices for the following sources of uncertainty: statistical, detector, flux, cross-section and FSI. The total shape-only systematic uncertainty covariance and correlation matrices are shown in figures 5.4- 5.8. For each run there are correlated bins in the low and high momentum regions with anticorrelations between these. This arises from shape uncertainties from the flux and cross-section models. The typical total uncertainties are around 8% for FHC runs and 10% for RHC (run 6). Run 5 has significantly higher uncertainties due to the very low statistics. The matrices for each source of uncertainty are shown in Appendix A.

5.2.1 Statistcal Uncertainties

These include uncertainties on both data and MC distributions. In both cases the absolute uncertainty on a given bin is the square-root of the value in the bin. The fractional uncertainty is then added to the diagonal elements of the covariance matrix.

5.2.2 Detector Systematic Uncertainties

The detector systematic matrix deals with uncertainties arising from processes after the neutrino interaction occurs. This includes both modelling and detector response uncertainties, described below, which are largely constrained using *in-situ* measurements of control samples, such as cosmic muons or test beam data gathered prior to installation in T2K. The detector response describes the expected raw signal observed

for a given event and understanding this is crucial for accurate reconstruction. The uncertainties relevant to this analysis are described below, separated by source.

- Particle kinematics and secondary interactions:

  The ability to reconstruct the kinematic properties of each particle accurately depends on understanding the detector response. In this selection the only momentum measurement is performed by the TPC due to its accuracy measuring the curvature of particle tracks. The momentum resolution uncertainty largely arises from uncertainties on the magnetic field. These uncertainties largely affect the momentum bin occupied by a given event, resulting in shape uncertainties of around 1-2%.

  Secondary interactions will also affect the measured kinematics of outgoing particles. These are interactions that occur after particles have left the initial nucleus and mainly affect pions and protons. Despite using an inclusive muon selection this is a significant source of uncertainty ($\sim 3\%$) due to misidentification of the muon candidate.

- Particle identification:

  Particle identification is performed using the TPC by comparing the measured rate of energy loss per unit distance along the path to different particle hypotheses. Theoretical curves along with data for positive and negative particles are shown in figure 5.3. As these are momentum dependent, the uncertainty on that measurement could result in wrongly identifying particles which leads to events migrating in or out of the selection. This is a small effect in this analysis as muons are easily differentiated from all particles other than charged pions. This confusion is most affect by pion secondary interactions resulting in small uncertainties ($<1\%$).

- Track matching:

  This selection requires a muon candidate produced in FGD1 with an associated track in TPC2. It is therefore important that the tracks in each detector are
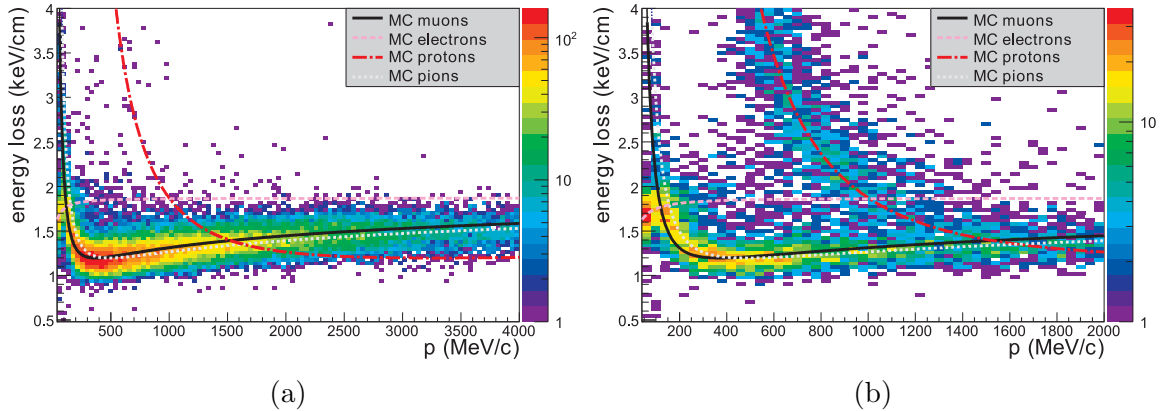
Figure 5.3: Theoretical energy loss (dE/dx) curves for different particles with data for negatively (a) and positively (b) charged particles produced in neutrino interactions.

correctly matched. Details of the matching process are given in [89]. Badly matched tracks will lead to events not being correctly reconstructed and failing the selection. This has a minimal (<1%) effect on this analysis.

- External backgrounds:

  These include any events occurring outside the FGD with a reconstructed vertex within the fiducial volume. These can originate either from other parts of the detector or the surrounding material. This is greatly reduced by requiring a lack of upstream activity but still contributes a $\sim 1\%$ uncertainty.

The detector systematic uncertainties are calculated using 1000 toy data sets generated using highland2/psyche [90]. This includes both weight uncertainties, where a new weight is applied to each event, and variation uncertainties in which variables are set to new values and the selection is then reapplied. These systematics cover various detector responses that cause events to migrate between bins, such as momentum resolution, and also charge mis-identification where the incorrect sign is applied to a track and the event would not pass the selection ($\sim 1\%$). The new weights and variables are then used to construct muon momentum distributions. These are used to calculate the covariance matrix.

5.2.3 Flux, Cross-section and FSI Systematic Uncertainties

These are calculated using an input matrix containing uncertainties on cross section parameters and the flux distribution, binned in true neutrino energy and flavour, to calculate new weights for each event. The matrices used in the fit contain the shape-only uncertainties. These control the relative behaviour of each bin but do not contain any information on the uncertainty of the overall normalisation.

- Cross-section Uncertainties

  The cross-section uncertainties cover uncertainties in the parameters that affect the signal and background interactions that are selected. These models determine what particles are produced at the interaction and their kinematic properties. Sources of cross section uncertainty include:

  1. Axial mass in resonant and quasi-elastic interactions

     The axial mass behaves as an effective nucleon radius and affects the cross section as a function of Q^2. In principle it should be the same for quasi-elastic and resonant interactions but is often considered separately.

  2. Fermi motion and spectral functions

     As described in section 2.2.1 these account for the change in properties between free nucleons and those within a nucleus. The nuclear models described in section 2.2.1 have large uncertainties associated with them.

  3. Interaction normalisations

     Cross section models are constrained using both internal and external measurements. Uncertainties arise from either the systematic errors on these results or from disagreement between them.

  The parameters used to propagate the cross section uncertainties are described in table 5.1.

- FSI uncertainties

Parameter	Type	Prior	Error	Validity range
M_A^{QE}	Signal shape	1.2	0.3	[0,999]
p_F^C	Signal shape	217	30	[200,275]
E_B^C	Signal shape	25	9	[12,42]
2p2h ν	Signal normalisation	1	1	[0,999]
C_A^5	Background shape	1.01	0.12	[0,999]
M_A^{RES}	Background shape	0.95	0.15	[0,999]
Bkg resonant	Background normalisation	1.3	0.2	[0,999]
DIS multiple pion	Background normalisation	0.0	0.4	[-999,999]
CC coherent on C	Background normalisation	1.0	0.3	[0,999]
NC coherent	Background normalisation	1.0	0.3	[0,999]
NC other	Background normalisation	1.0	0.3	[0,999]

Table 5.1: Cross-section parameters used in this analysis with type, prior, uncertainty and validity range [91].

FSI models are applied to the particles produced in an interaction as they propagate through the nucleus. These processes are described in more detail in section 2.2.1. The uncertainties on these models arise from:

1. Elastic scattering

   Elastic scattering changes the kinematic properties of a particle but does affect whether the particle continues to propagate. This would be likely to cause shape uncertainties in this analysis by changing the momentum of the muon candidate.

2. Inelastic scattering and absorption

   These effects alter the number and type of particles which escape the nucleus. As all selections used only require identifying a muon and do not depend on any other particles these effects will be small.

3. Charge exchange

   When a pion propagates through the nucleus there is a chance that the charge will be changed through reactions such as $\pi^+ + n \rightarrow \pi^0 + p$. As this does not affect muons it is unlikely to have any significant effect.

As FSI predominantly affects hadronic particles and this selection relies only

on the muon candidate kinematics it is likely that these uncertainties will be relatively small. The parameters used to propagate the FSI uncertainties are described in table 5.2.

Parameter	Type	Prior	Error	Validity range
Inelastic low energy $(p_\pi < 500 MeV/c)$	Shape	0.0	0.41	[-1.2,1.2]
Inelastic high energy $(p_\pi > 400 MeV/c)$	Shape	0.0	0.34	[-0.9,0.9]
Pion production	Shape	0.0	0.5	[-1.5,1.5]
Pion absorption	Shape	0.0	0.41	[-1.2,1.2]
Charge exchange low energy $(p_\pi < 500 MeV/c)$	Shape	0.0	0.57	[-1.8,1.8]
Charge exchange high energy $(p_\pi > 400 MeV/c)$	Shape	0.0	0.28	[-0.9,0.9]

Table 5.2: Pion FSI parameters used in this analysis with type, prior, uncertainty and validity range [91].

- Flux uncertainties

  The sources of flux uncertainty are shown in figure 3.3 and originate from three broad areas:

  1. Hadronic interactions

     These are the dominant part of the T2K flux uncertainties and include uncertainties on the initial proton interaction cross-section, the particles produced by these interactions and any secondary interactions which occur.

  2. Proton beam properties

     Uncertainties on the beam position and direction would have the effect of changing the off-axis angle which would alter the neutrino beam energy spectrum and flavour composition. There is also some small uncertainty on the number of protons hitting the target.

  3. Magnetic horns

     The magnetic horns are responsible for focussing hadrons which leave the target. If these are not well aligned or operating at a different current this could affect the off-axis angle and neutrino beam width.

The flux model uncertainty is calculated by varying the underlying parameters [64]. Where there are several correlated parameters in the flux model the values are varied simultaneously, taking the correlations into account, and where a parameter is not correlated it is varied independently.

The covariance matrices for each source of uncertainty are added together to give the total covariance matrix used in the fit. The following chapter describes the toy data tests used to check the performance of the fit with the total covariance matrix included as well as fake data tests with only the relevant uncertainties included.
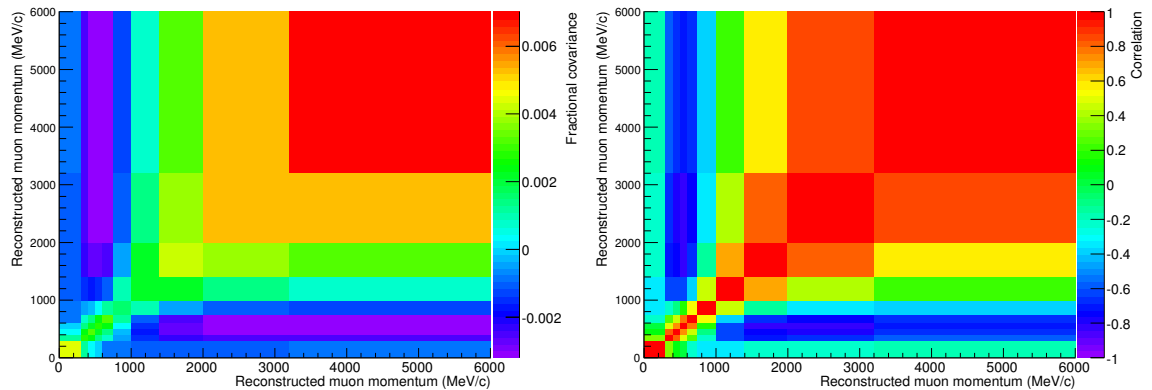
(a) Run 2 full, shape-only systematic uncertainty covariance matrix

(b) Run 2 full, shape-only systematic uncertainty correlation matrix
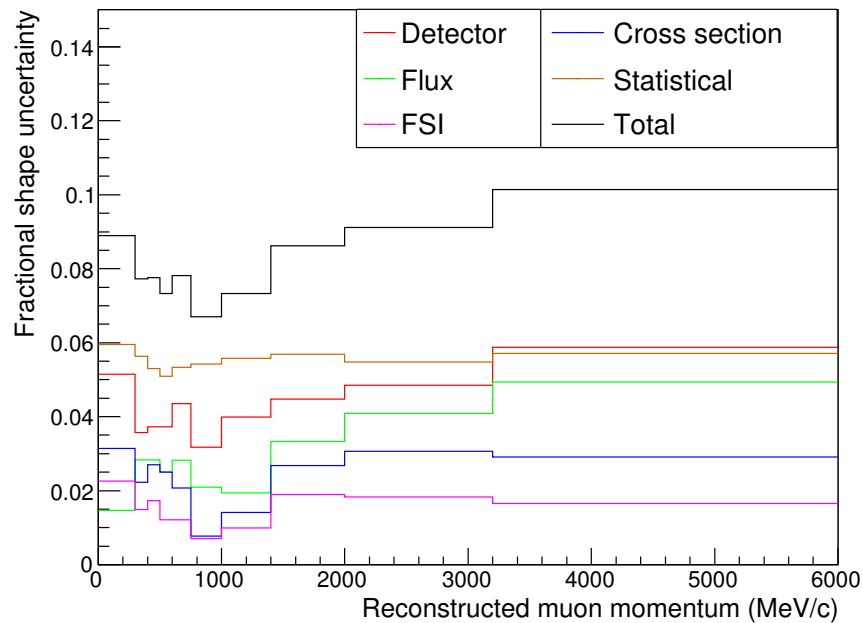
(c) Run 2 full, shape-only systematic uncertainties

Figure 5.4: The top plots show the shape-only, (a) fractional covariance and (b) correlation matrices for all run 2 (FHC) systematic uncertainties. The uncertainty on each bin (c) is the square root of the diagonal element of the covariance matrix and is shown both as a total uncertainty and broken down by type. The off-diagonal elements of (a) and (b) show the covariance and correlation between bins respectively.

(a) Run 3 full, shape-only systematic uncertainty covariance matrix

(b) Run 3 full, shape-only systematic uncertainty correlation matrix

(c) Run 3 full, shape-only systematic uncertainties

Figure 5.5: The top plots show the shape-only, (a) fractional covariance and (b) correlation matrices for all run 3 (FHC) systematic uncertainties. The uncertainty on each bin (c) is the square root of the diagonal element of the covariance matrix and is shown both as a total uncertainty and broken down by type. The off-diagonal elements of (a) and (b) show the covariance and correlation between bins respectively.
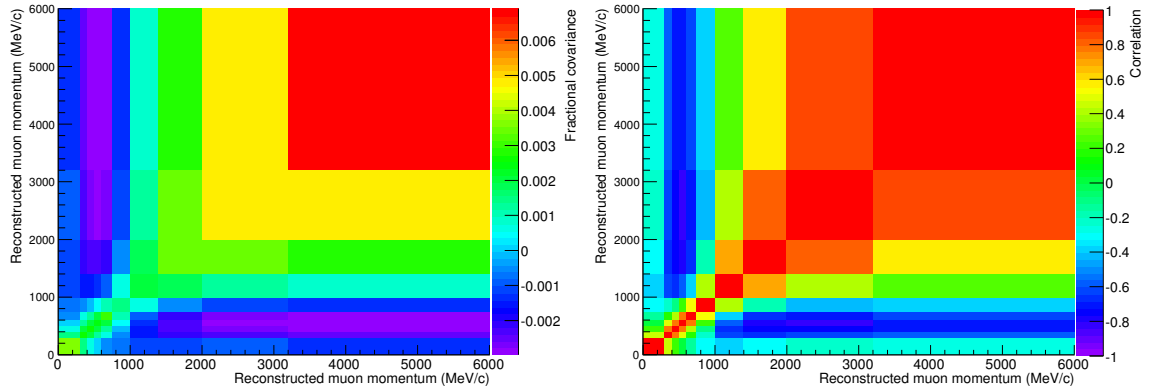
(a) Run 4 full, shape-only systematic uncertainty covariance matrix

(b) Run 4 full, shape-only systematic uncertainty correlation matrix
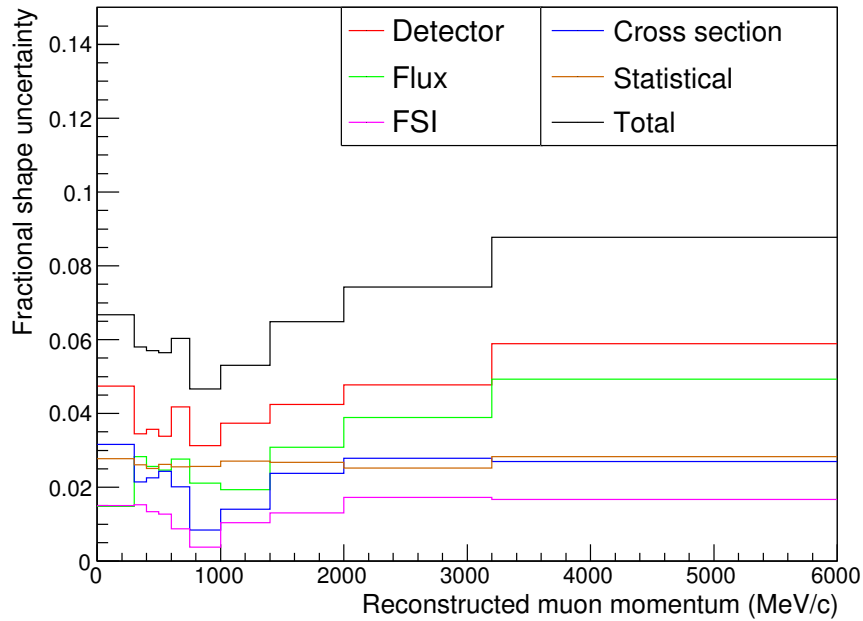
(c) Run 4 full, shape-only systematic uncertainties

Figure 5.6: The top plots show the shape-only, (a) fractional covariance and (b) correlation matrices for all run 4 (FHC) systematic uncertainties. The uncertainty on each bin (c) is the square root of the diagonal element of the covariance matrix and is shown both as a total uncertainty and broken down by type. The off-diagonal elements of (a) and (b) show the covariance and correlation between bins respectively.
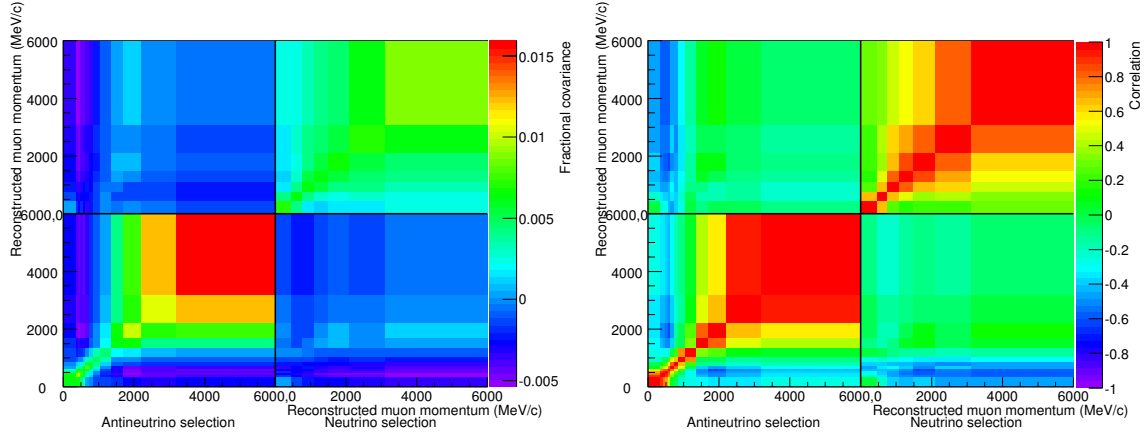
(a) Run 5 full, shape-only systematic uncertainty covariance matrix

(b) Run 5 full, shape-only systematic uncertainty correlation matrix
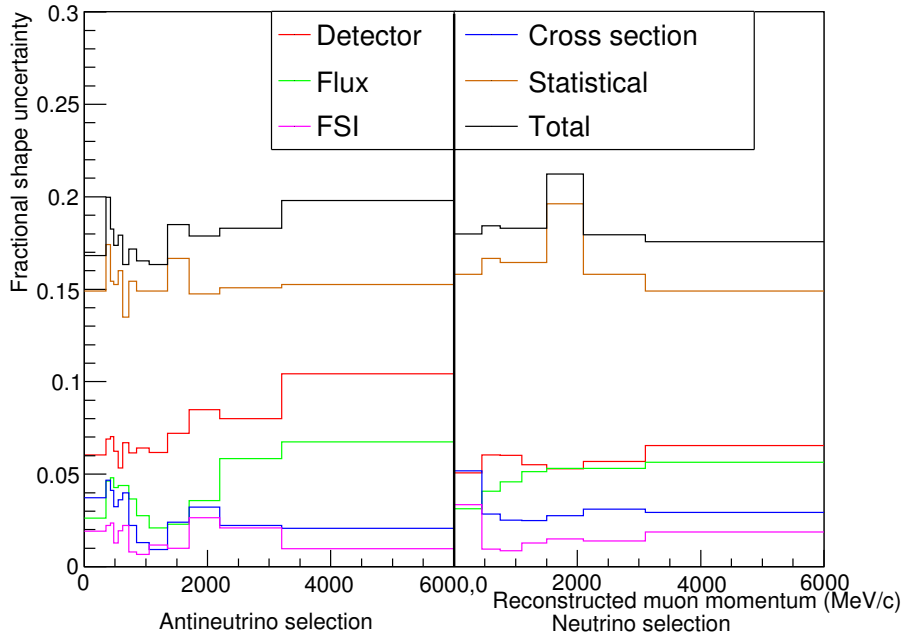
(c) Run 5 full, shape-only systematic uncertainties

Figure 5.7: The top plots show the shape-only, (a) fractional covariance and (b) correlation matrices for all run 5 (RHC) systematic uncertainties. The uncertainty on each bin (c) is the square root of the diagonal element of the covariance matrix and is shown both as a total uncertainty and broken down by type. The off-diagonal elements of (a) and (b) show the covariance and correlation between bins respectively.
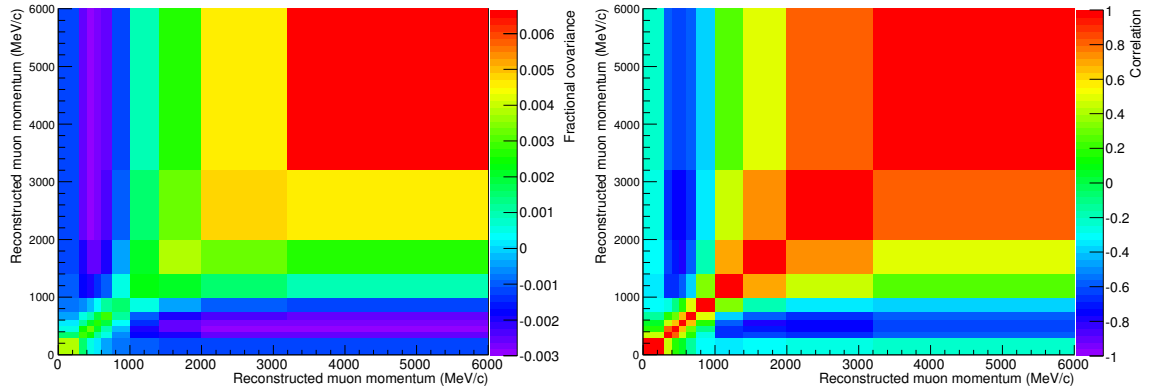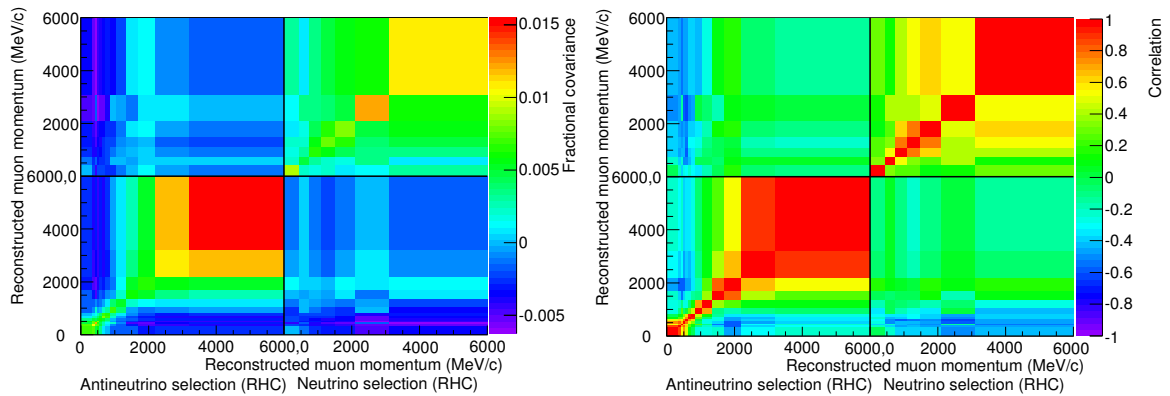
(a) Run 6 full, shape-only systematic uncertainty covariance matrix

(b) Run 6 full, shape-only systematic uncertainty correlation matrix
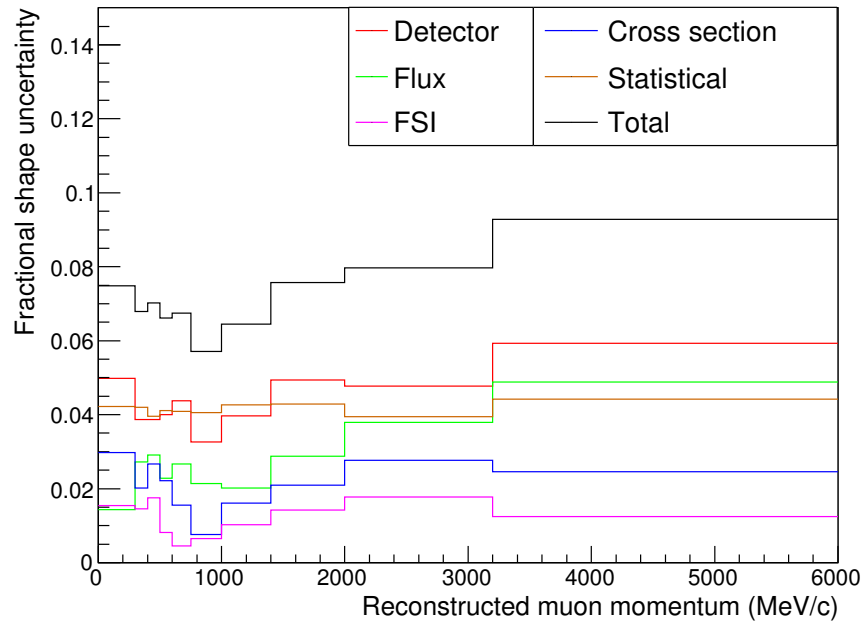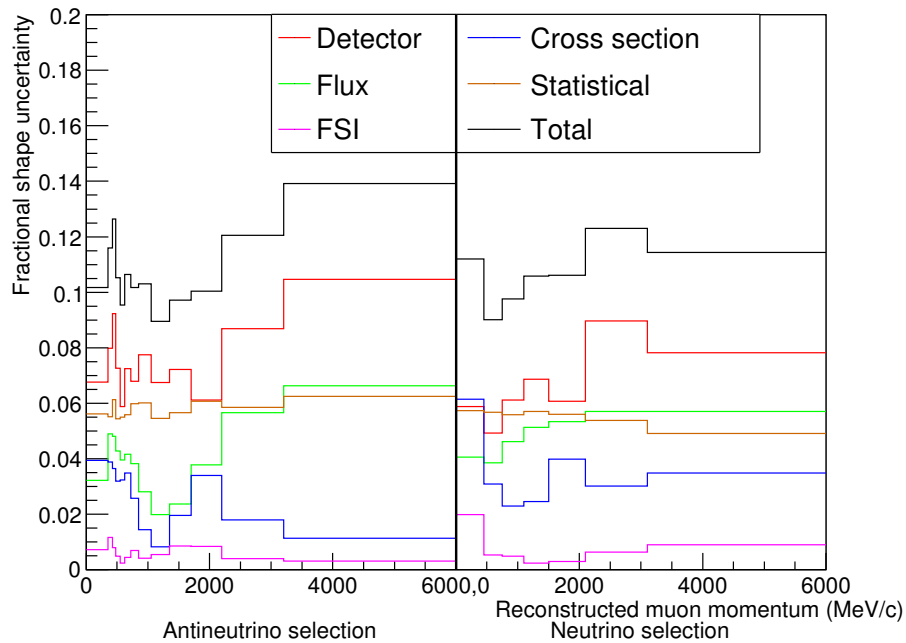

(c) Run 6 full, shape-only systematic uncertainties

Figure 5.8: The top plots show the shape-only, (a) fractional covariance and (b) correlation matrices for all run 6 (RHC) systematic uncertainties. The uncertainty on each bin (c) is the square root of the diagonal element of the covariance matrix and is shown both as a total uncertainty and broken down by type. The off-diagonal elements of (a) and (b) show the covariance and correlation between bins respectively.

Chapter 6

Fitter Validation

In order to check that the fit mechanism is working correctly, it is important to perform various tests. This analysis uses toy data sets followed by fake data sets taken from two different neutrino interaction MC generators to validate the fitter. These tests are detailed in the following sections.

6.1   Toy Data Tests

The first step in the validation was to generate toy data sets from the NEUT MC distribution by reweighting it using the systematic uncertainties.

The number of events in each muon momentum bin is multiplied by a new weight, W, given by:

$$W_i = \sum_{j=1}^{NBins} 1 + M_{ij}G_j, \tag{6.1}$$

where M is an error matrix formed by Cholesky decomposing [92] the full systematic covariance matrix and G is a vector of random numbers from a Gaussian distribution with a width of one and mean of zero. The reweighted MC is then used as the toy data set and the fit is performed. It is important that the distribution of results from these toy data sets matches the known input values and that no bias exists. In order to check that the fit is unbiased pull values were calculated using:

$$\text{Pull} = \frac{f_{\text{fit}} - f_{\text{true}}}{\sigma_{\text{fit}}}, \qquad (6.2)$$

where f_{fit} and σ_{fit} are the fitted value and its uncertainty and f_{true} is the true value of the parameter. Multiple tests are run and pull distributions constructed. If the fit is unbiased, the pull distributions should be Gaussian in shape with a mean of zero and width of one. Throughout this analysis the uncertainties are assumed to be Gaussian, however deviations from this could result in a small bias in the fit.

This is then repeated and the neutrino parent components are scaled relative to each other. These tests check that the fit is successful over a range of parameter values more extreme than the variations expected in the data.

During these fits it was noticed that, due to its relative lack of shape, the 'other' sample had a very wide range of fitted values. This often resulted in the fit returning unphysical negative values for this parameter. In order to prevent this impacting the remaining results, the scale factor was fixed to the nominal value, i.e. 1, in both FHC and RHC samples. This value was fixed for all test and data fits. Fits were performed to 10,000 toy data sets for each set of scalings given in table 6.1 for FHC runs and table 6.2 for RHC runs. The resulting fitted values are given in tables 6.3 and 6.4 for FHC and RHC runs respectively, the parameter value and pull distributions are shown in Appendix B. We see that the pull mean is much smaller than the pull width in almost all cases indicating that there is no significant bias. The exceptions to this are in the more extreme toy data sets (set 4). These are sufficiently far from the nominal prediction that such a change would have been clearly observed previously. The first toy set for run two is shown in figure 6.1 and the fit results appear Gaussian as expected with the pulls also matching the expected distribution of a Gaussian with a mean of zero and width of one.

Results from fits using the toy data sets show no indication of bias except in extreme cases, well beyond the realistic range of the parameters.

Toy set	π^+ scaling	K^+ scaling	Other scaling
1	1.0	1.0	1.0
2	0.7	1.5	1.0
3	3.0	1.0	1.0
4	1.0	0.1	1.0

Table 6.1: Four sets of values used as scalings for toys data sets for FHC runs, designed to test the fitter over a greater range than should be required. The first set of scalings is simply the nominal MC.

Toy set	π^- scaling	K^- scaling	π^+ scaling	K^+ scaling	Other scaling
1	1.0	1.0	1.0	1.0	1.0
2	0.7	1.2	1.5	0.9	1.0
3	3.0	1.0	0.8	2.0	1.0
4	1.0	0.1	0.4	1.3	1.0

Table 6.2: Four sets of values used as scalings for toys data sets for RHC runs, designed to test the fitter over a greater range than should be required. The first set of scalings is simply the nominal MC.

Run	Toy set	π^+ pull mean	π^+ pull width	K^+ pull mean	K^+ pull width
2	1	0.051	0.995	-0.054	0.981
	2	-0.043	0.990	-0.036	0.976
	3	0.021	0.995	-0.019	0.990
	4	0.086	0.992	-0.088	0.983
3	1	0.046	1.004	-0.046	0.992
	2	-0.047	0.997	-0.040	0.990
	3	0.052	1.005	-0.053	0.994
	4	0.061	1.008	-0.062	0.995
4	1	0.053	0.997	-0.051	0.989
	2	-0.036	0.996	-0.041	0.982
	3	0.061	1.000	-0.060	0.992
	4	0.169	0.998	-0.173	0.986

Table 6.3: Means and widths for pull distributions from the FHC toy data tests. In almost all cases the pull means are much smaller than the pull widths showing that there is no significant bias in the fit. The greatest disagreement comes in the more extreme toy data sets that lie well clear of where the data is expected to be. Any such differences would have been observed before this point.

Run	Toy set	π^+ pull mean	π^+ pull width	K^+ pull mean	K^+ pull width
5	1	0.009	0.974	-0.089	0.977
	2	0.022	0.979	-0.081	0.978
	3	0.019	0.983	-0.081	0.975
	4	0.013	0.972	-0.079	0.975
6	1	0.009	0.961	0.099	0.974
	2	0.013	0.974	-0.086	0.990
	3	0.032	0.982	-0.100	0.956
	4	0.031	0.984	-0.085	0.970
Run	Toy set	π^- pull mean	π^- pull width	K^- pull mean	K^- pull width
5	1	0.090	0.989	-0.078	0.965
	2	0.064	0.991	-0.055	0.967
	3	0.097	0.977	-0.077	0.975
	4	0.082	0.983	-0.061	0.985
6	1	0.107	0.976	-0.070	0.987
	2	0.074	0.979	-0.061	0.971
	3	0.102	0.976	-0.064	0.999
	4	0.086	0.981	-0.059	0.981

Table 6.4: Means and widths for pull distributions from the RHC toy data tests. In almost all cases the pull means are much smaller than the pull widths showing that there is no significant bias in the fit.

6.2 Fake Data Tests

Fake data tests allow a stronger test of the fitting method by using data with expected differences from the MC distribution. Tests are performed using a statistically independent NEUT sample and also a GENIE sample as fake data. In all cases NEUT is used as MC in the fit and the 'other' component is fixed at its nominal value.

The NEUT fake data test uses the same cross-section and FSI models for both fake data and MC whereas the GENIE fake data uses different models and provides a more thorough test of how the fit will behave when applied to data.

6.2.1 NEUT Fake Data

This test is performed by splitting the NEUT MC into two parts, using one part as fake data and the other as the fit templates. A sample is randomly selected from the total NEUT MC to be the fake data, and a larger, independent sample is used
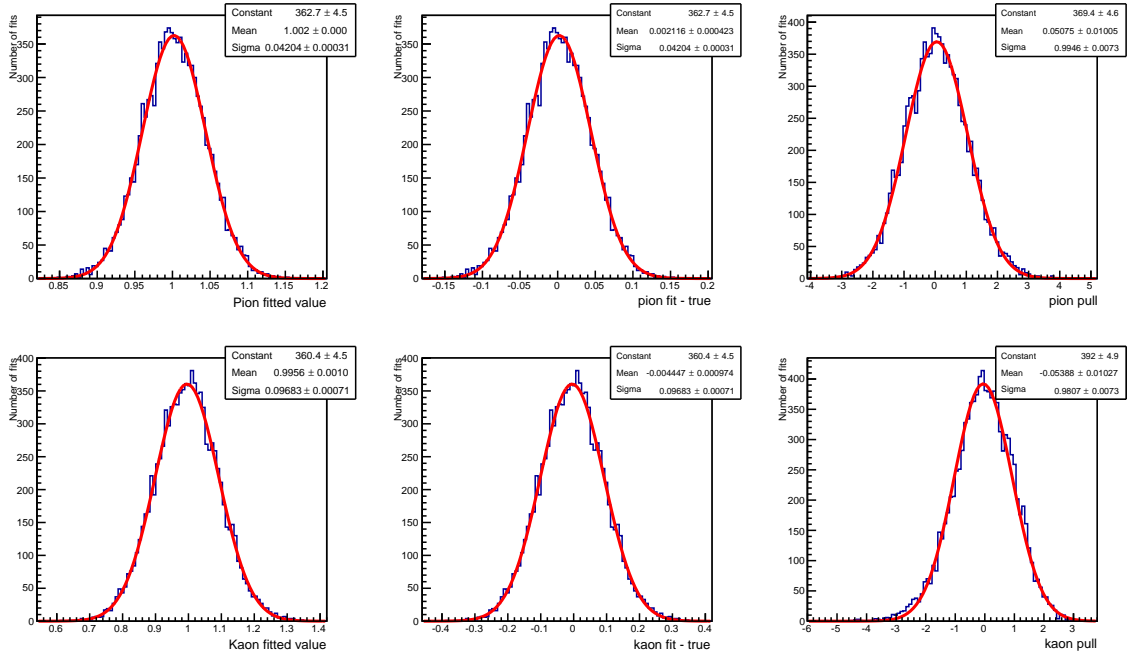
Figure 6.1: Run 2 toy data results from initial scalings given by toy set 1 from table 6.1. The fit results appear Gaussian as expected with the pulls also matching the expected distribution of a Gaussian with a mean of zero and width of one.

as the MC distributions. As this sample is drawn from the same generator the same cross-section and FSI models are used in both the fake data and MC distributions. The differences are purely statistical and as such, only statistical uncertainties are included in the covariance matrix during the fit. The results from these tests are summarised in tables 6.5 and 6.6. The results show good agreement between the fit results, shown in figures 6.2-6.6, and the expected value, given by the ratio of the true numbers of events between the fake data and MC, scaled by the relative size. The p-value for the run 5 fit is significant at the 0.05 level. As described in section 5.1.1, 10% of these values are expected outside of the limits at this significance level. As these results show one such value out of five, and two out of ten across all fake data fits, this is not significant.

Run	Parent	True value	Fitted value	Fit Uncertainty	χ^2/D.o.F	p value
2	π^+	0.996	1.002	0.014	6.74/8	0.565
	K^+	1.005	0.989	0.026		
3	π^+	1.000	0.984	0.021	5.95/8	0.653
	K^+	1.001	1.033	0.039		
4	π^+	1.004	1.007	0.008	6.77/8	0.562
	K^+	0.991	0.984	0.014		

Table 6.5: Run 2-4 NEUT fake data results. NEUT is used as MC with a statistically independent NEUT sample as the fake data set. The true values are the ratio of true events in the fake data set to the expected number calculated using the MC sample. The results for all runs agree well with the true values and the p-values indicate that all the fits have performed well.

| Run	Parent	True value	Fitted value	Fit Uncertainty	χ^2/D.o.F	p value
5	π^-	0.991	0.981	0.021	28.97/16	0.024
	K^-	1.049	1.109	0.083		
	π^+	1.014	1.078	0.055		
	K^+	0.971	0.898	0.084		
6	π^-	0.972	0.991	0.026	13.48/16	0.737
	K^-	1.160	1.180	0.111		
	π^+	0.984	0.995	0.067		
	K^+	1.040	0.965	0.101		

Table 6.6: Run 5-6 NEUT fake data results. NEUT is used as MC with a statistically independent NEUT sample as the fake data set. The true values are the ratio of true events in the fake data set to the expected number calculated using the MC sample. The results for all runs agree well with the true values. The first p-value appears to indicate some concern at the 0.05 significance level. One point at this significance is expected across the ten tests and as there are only two significant points across all tests this is not significant overall.
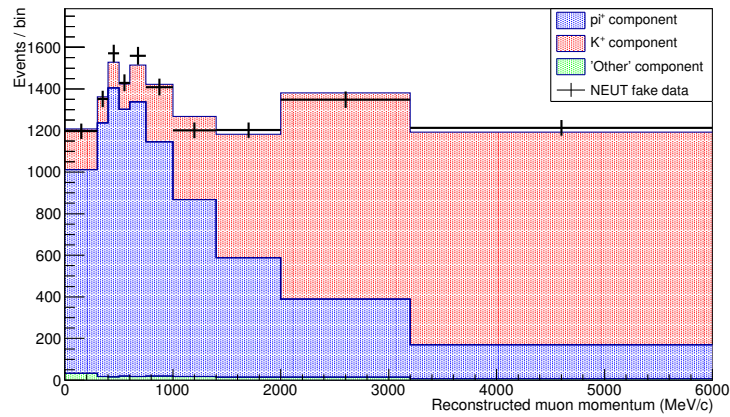
(a) Run 2 NEUT fake data prefit
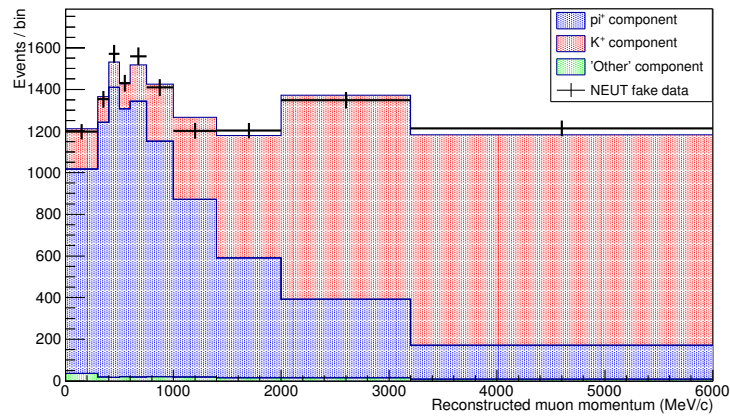
(b) Run 2 NEUT fake data postfit
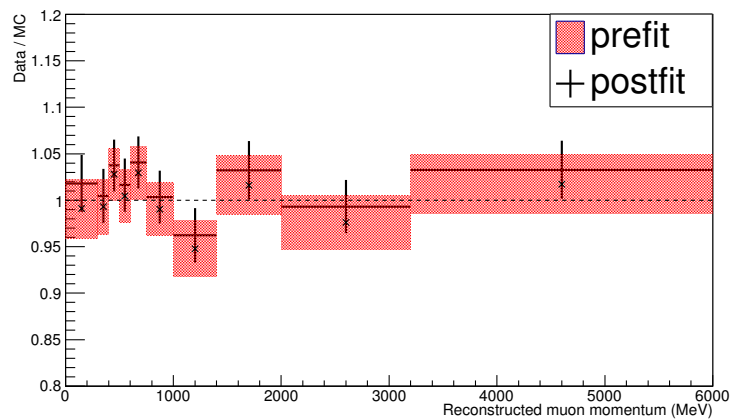
(c) Run 2 NEUT fake data/MC ratio

Figure 6.2: Run 2 prefit, postfit and data/MC distributions, using a fake data set drawn from the NEUT MC fitted using a statistically independent NEUT MC. As NEUT MC is used both as fake data and as MC the models are the same meaning that only statistical uncertainties are included in the fit.
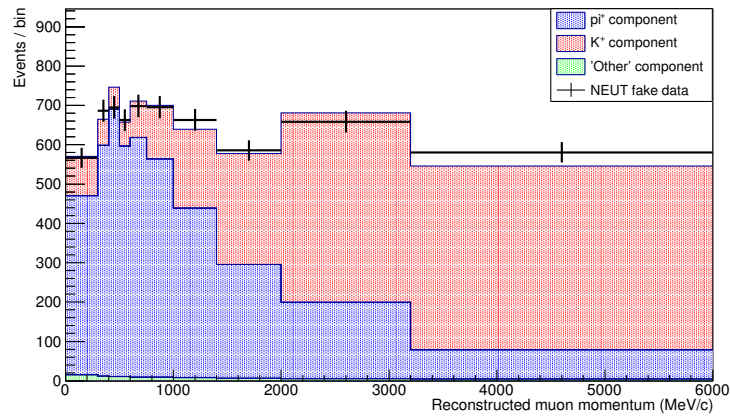
(a) Run 3 NEUT fake data prefit

(b) Run 3 NEUT fake data postfit

(c) Run 3 NEUT fake data/MC ratio

Figure 6.3: Run 3 prefit, postfit and data/MC distributions, using a fake data set drawn from the NEUT MC fitted using a statistically independent NEUT MC. As NEUT MC is used both as fake data and as MC the models are the same meaning that only statistical uncertainties are included in the fit.

(a) Run 4 NEUT fake data prefit

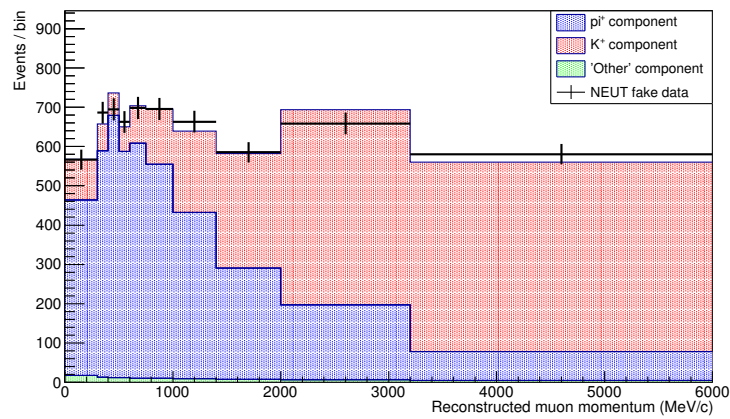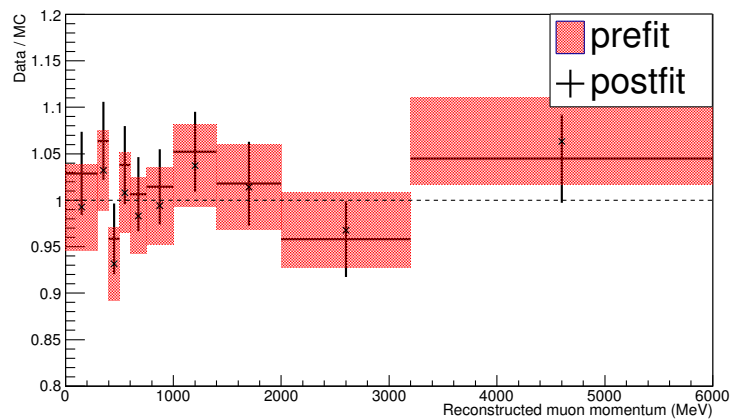(b) Run 4 NEUT fake data postfit

(c) Run 4 NEUT fake data/MC ratio

Figure 6.4: Run 4 prefit, postfit and data/MC distributions, using a fake data set drawn from the NEUT MC fitted using a statistically independent NEUT MC. As NEUT MC is used both as fake data and as MC the models are the same meaning that only statistical uncertainties are included in the fit.

(a) Run 5 NEUT fake data prefit

(b) Run 5 NEUT fake data postfit

(c) Run 5 NEUT fake data/MC ratio

Figure 6.5: Run 5 prefit, postfit and data/MC distributions, using a fake data set drawn from the NEUT MC fitted using a statistically independent NEUT MC. As NEUT MC is used both as fake data and as MC the models are the same meaning that only statistical uncertainties are included in the fit.
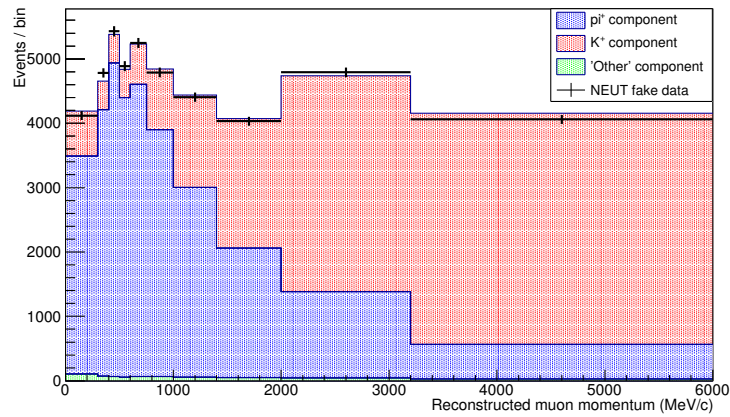
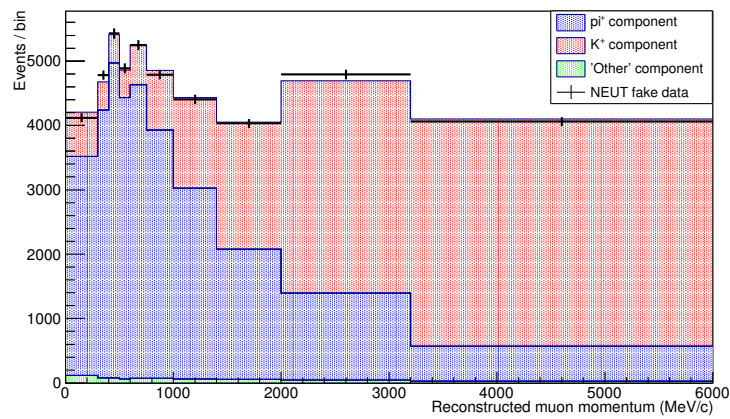(a) Run 6 NEUT fake data prefit

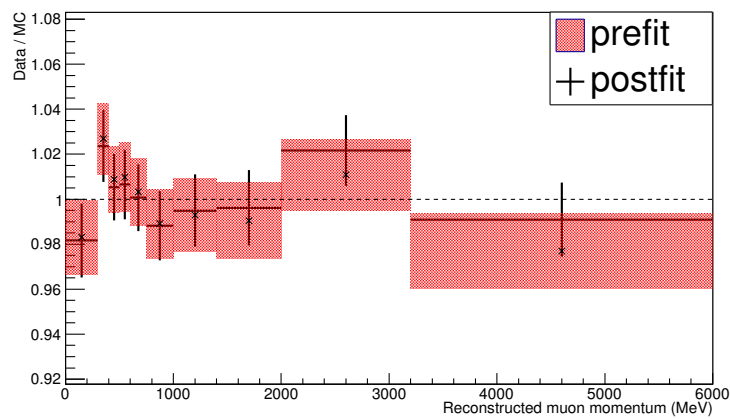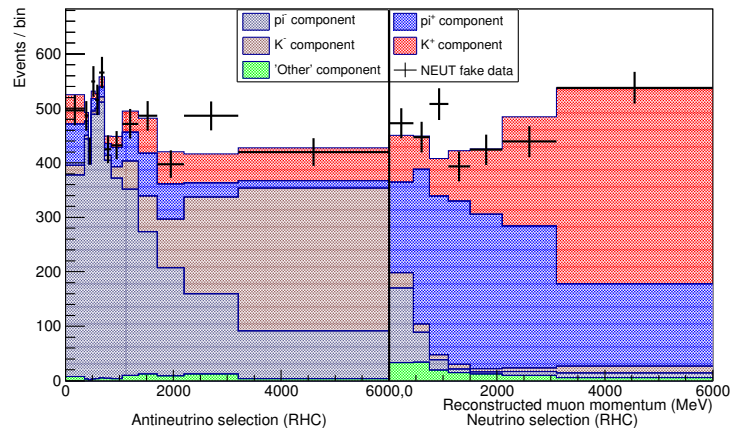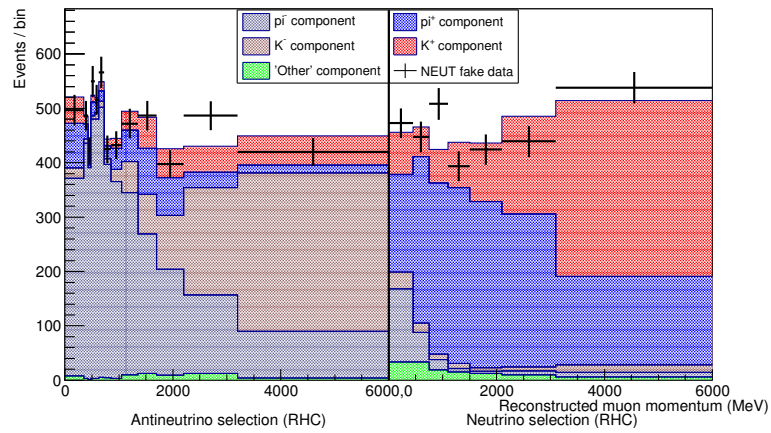(b) Run 6 NEUT fake data postfit
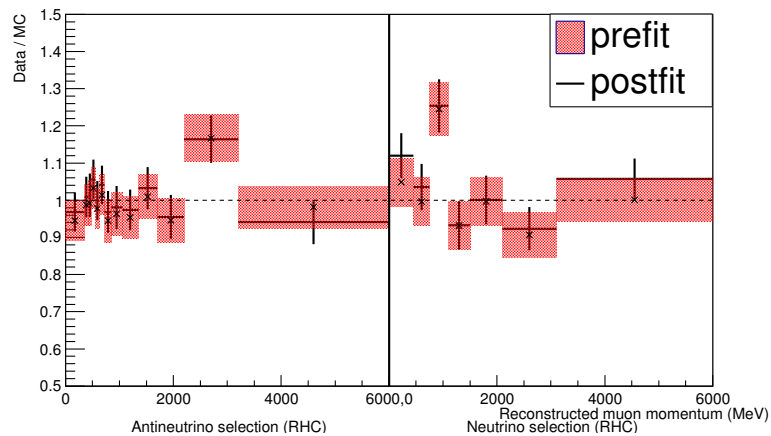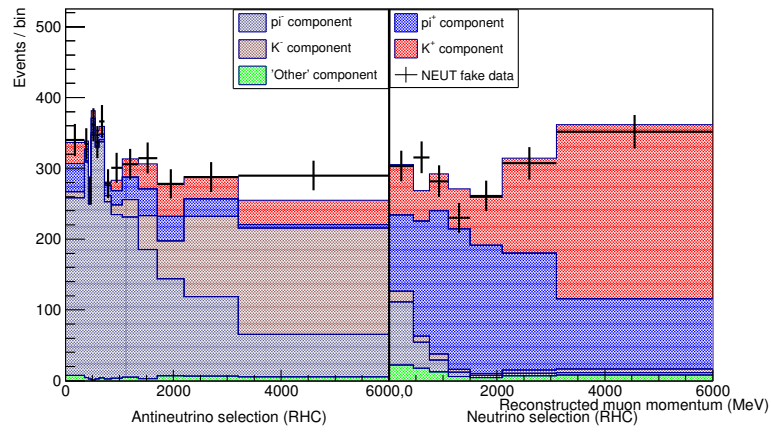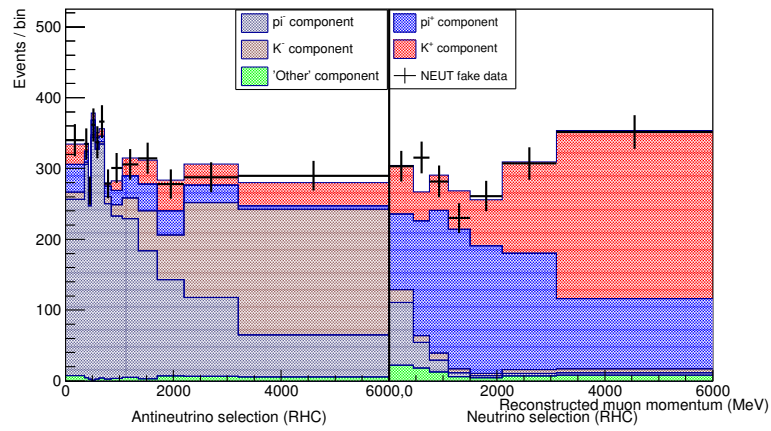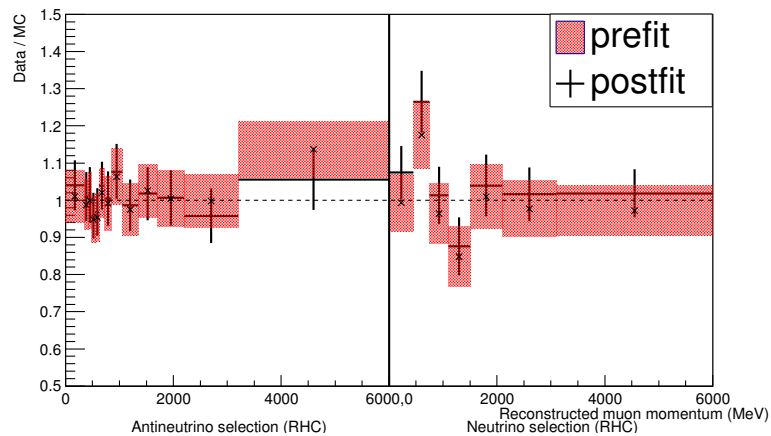

(c) Run 6 NEUT fake data/MC ratio

Figure 6.6: Run 6 prefit, postfit and data/MC distributions, using a fake data set drawn from the NEUT MC fitted using a statistically independent NEUT MC. As NEUT MC is used both as fake data and as MC the models are the same meaning that only statistical uncertainties are included in the fit.
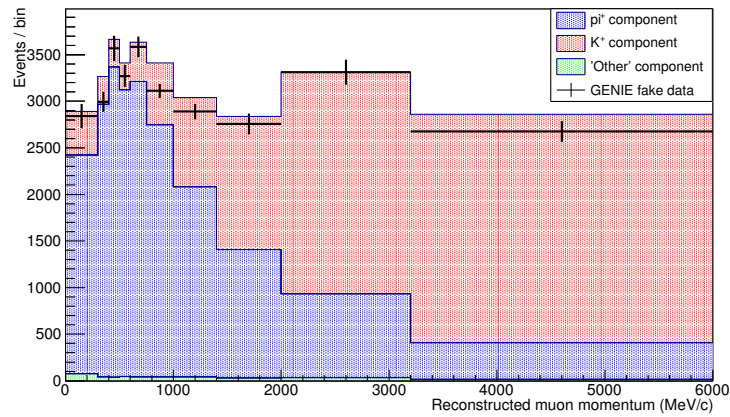
6.2.2 GENIE Fake Data

In this case GENIE MC is used as a fake data sample. This uses different cross section and FSI models from the NEUT MC and therefore the covariance matrices for these uncertainties are added to the statistical covariance matrix to account for shape changes arising from the different models. The flux inputs and detector response are the same for both generators, therefore these uncertainties are not included here. The use of the same flux model results in identical neutrino parent yields for neutrinos arriving at the detector. However differences in the energy dependence in the various cross section models then change the neutrino parent yields for the generated events.

These results, shown in figures 6.7-6.11, also agree well with the truth information for all runs, as seen in tables 6.7 and 6.8, confirming that the fit is performing as expected. The p-value for the run 2 fit is significant at the 0.05 level. As mentioned in section 6.2.1, the results from both sets of fake data tests show two results outside the limits defined in section 5.1.1. This is not significantly different from what is expected.

Run	Parent	True value	Fitted value	Fit Uncertainty	$\chi^2/D.o.F$	p value
2	π^+	0.938	0.973	0.019	18.68/8	0.017
	K^+	0.963	0.965	0.041		
3	π^+	0.880	0.875	0.022	13.80/8	0.087
	K^+	0.962	1.019	0.049		
4	π^+	0.949	0.977	0.019	10.21/8	0.251
	K^+	0.962	0.944	0.041		

Table 6.7: Run 2-4 GENIE fake data results. A GENIE sample is used as fake data with NEUT as MC and, due to the different models, cross section and FSI uncertainties are included in the fit. The true values are the ratio of true events in the data set to the expected number given by the MC and scaled by the relative size. The results for all runs agree well with the true values. The first p-value appears to indicate some concern at the 0.05 significance level. One point at this significance is expected across the ten tests and as there are only two significant points across all tests. This is not significant overall.

(a) Run 2 GENIE fake data prefit
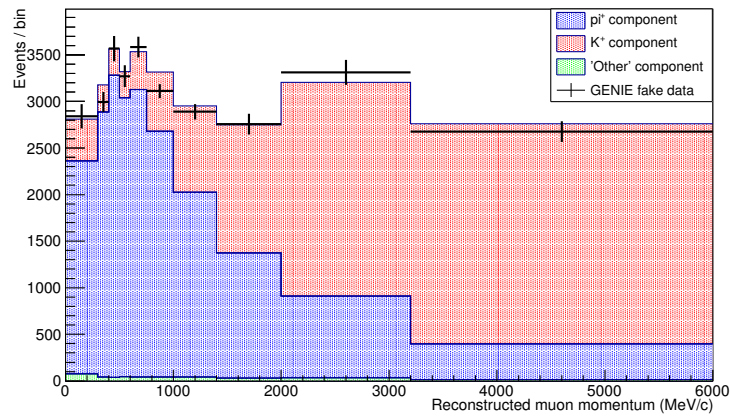
(b) Run 2 GENIE fake data postfit
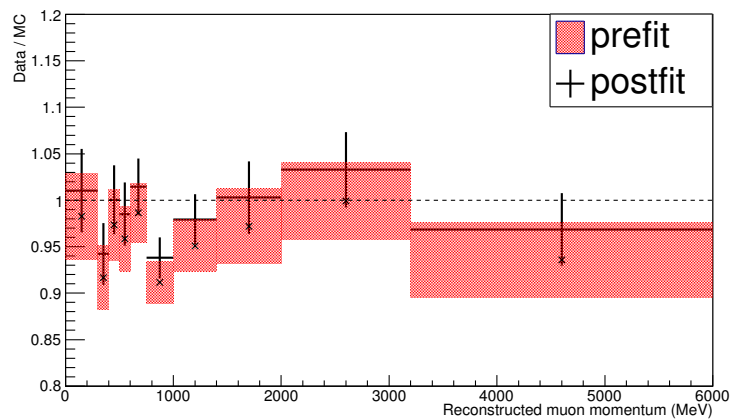
(c) Run 2 GENIE fake data/MC ratio

Figure 6.7: Run 2 prefit, postfit and data/MC ratio distributions with a GENIE fake data sample (7.47×10^{20} POT) and NEUT as MC. Due to the different MC generators the error bars shown here include cross-section and FSI uncertainties in addition to the statistical uncertainties.

(a) Run 3 GENIE fake data prefit

(b) Run 3 GENIE fake data postfit

(c) Run 3 GENIE fake data/MC ratio

Figure 6.8: Run 3 prefit, postfit and data/MC ratio distributions with a GENIE fake data sample (7.47×10^{20} POT) and NEUT as MC. Due to the different MC generators the error bars shown here include cross-section and FSI uncertainties in addition to the statistical uncertainties.

(a) Run 4 GENIE fake data prefit

(b) Run 4 GENIE fake data postfit

(c) Run 4 GENIE fake data/MC ratio

Figure 6.9: Run 4 prefit, postfit and data/MC ratio distributions with a GENIE fake data sample (7.47×10^{20} POT) and NEUT as MC. Due to the different MC generators the error bars shown here include cross-section and FSI uncertainties in addition to the statistical uncertainties.

(a) Run 5 GENIE fake data prefit
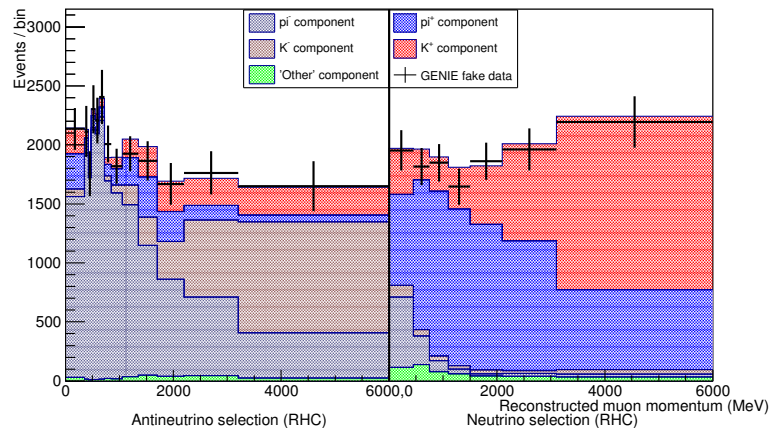
(b) Run 5 GENIE fake data postfit
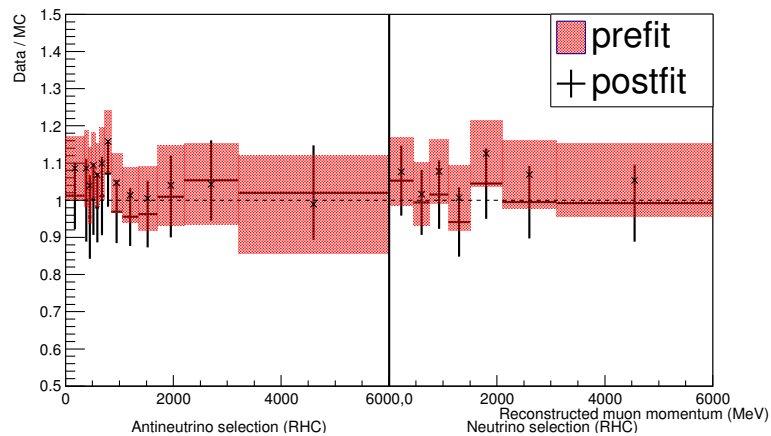
(c) Run 5 GENIE fake data/MC ratio

Figure 6.10: Run 5 prefit, postfit and data/MC ratio distributions with a GENIE fake data sample (7.47×10^{20} POT) and NEUT as MC. Due to the different MC generators the error bars shown here include cross-section and FSI uncertainties in addition to the statistical uncertainties.
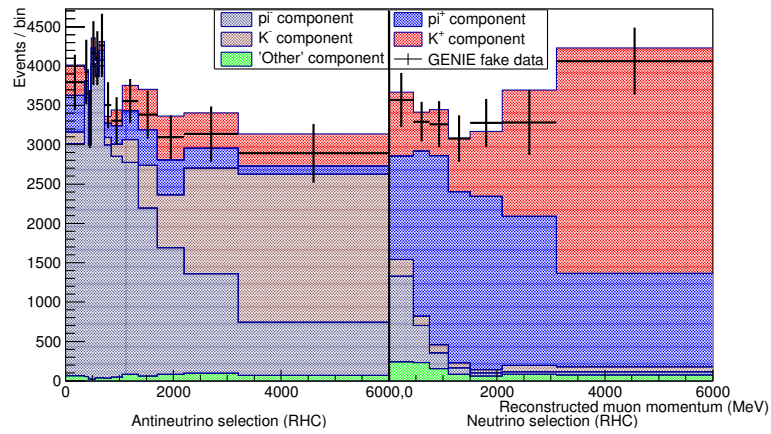
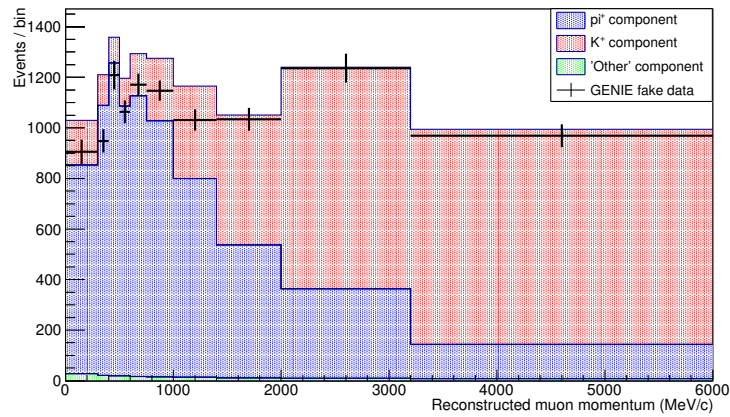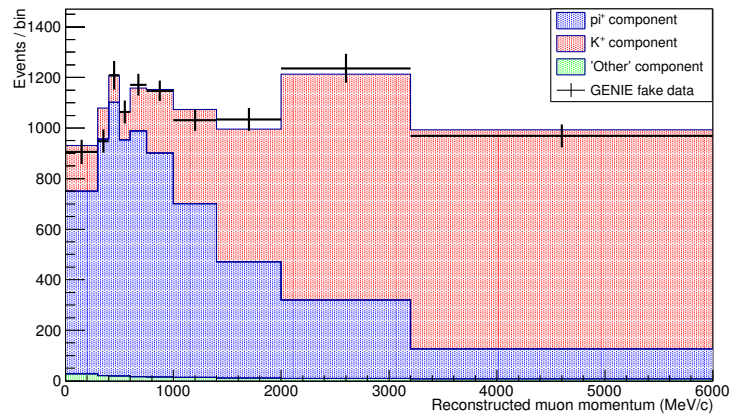(a) Run 6 GENIE fake data prefit
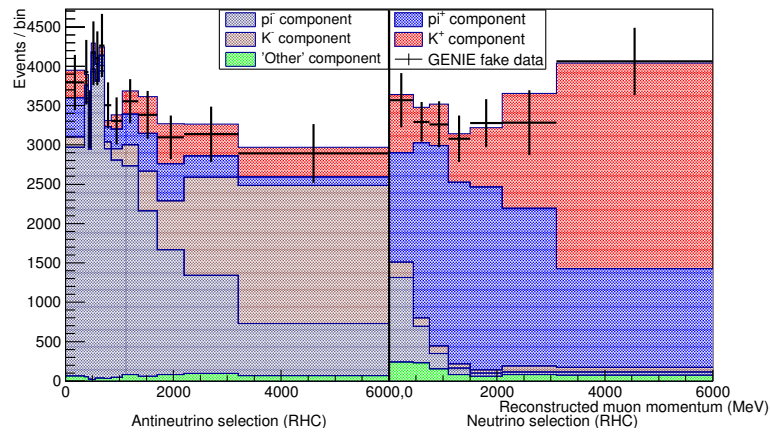
(b) Run 6 GENIE fake data postfit
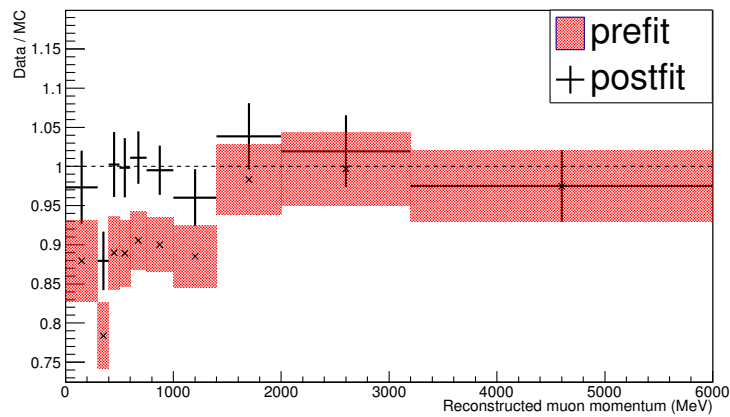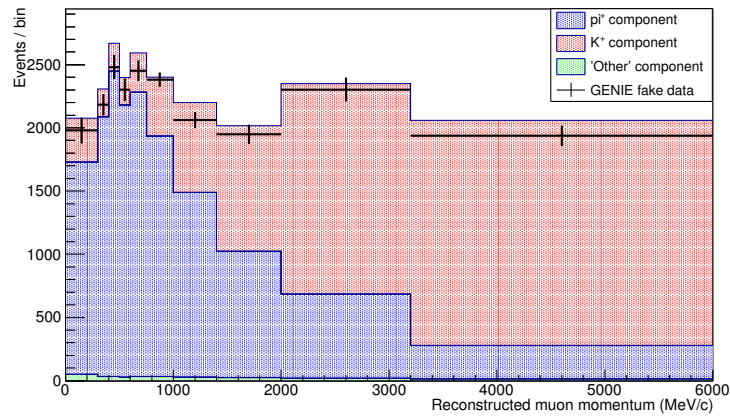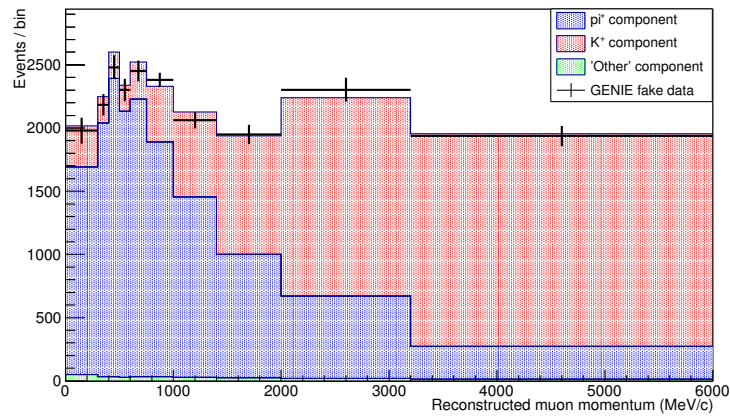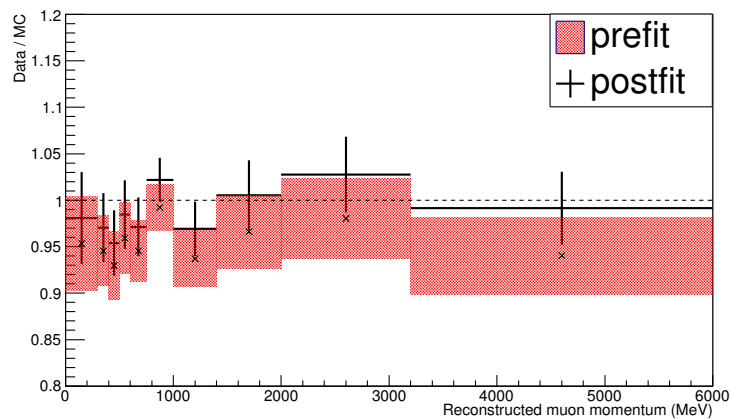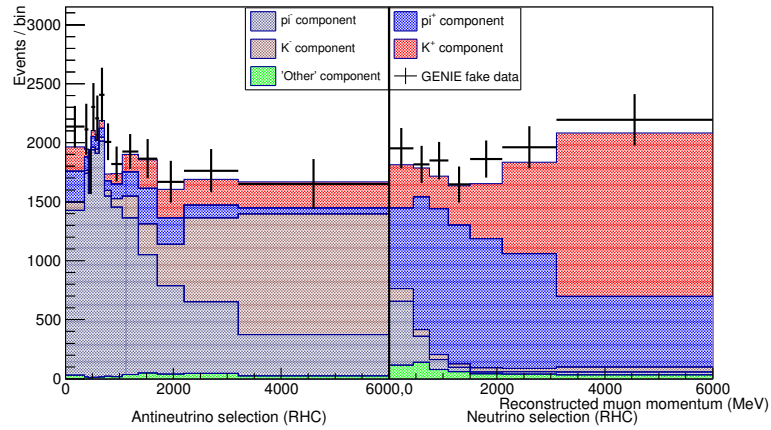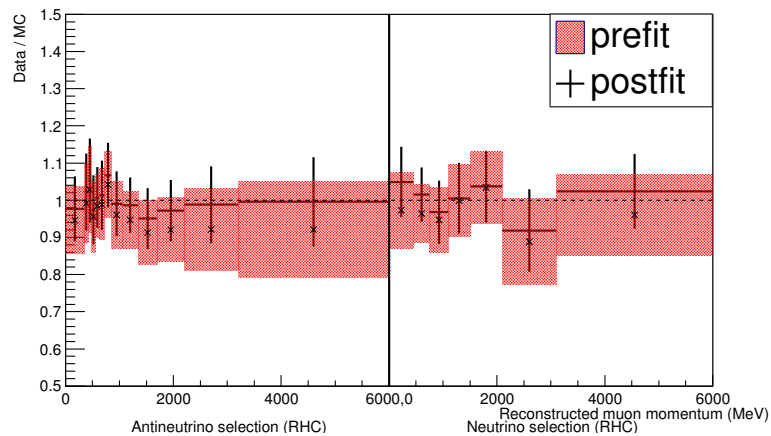

(c) Run 6 GENIE fake data/MC ratio

Figure 6.11: Run 6 prefit, postfit and data/MC ratio distributions with a GENIE fake data sample (7.47×10^{20} POT) and NEUT as MC. Due to the different MC generators the error bars shown here include cross-section and FSI uncertainties in addition to the statistical uncertainties.

Run	Parent	True value	Fitted value	Fit Uncertainty	$\chi^2/D.o.F$	p value
5	π^-	1.063	1.097	0.066	15.43/16	0.493
	K^-	1.040	0.919	0.211		
	π^+	1.032	1.131	0.107		
	K^+	1.119	1.060	0.148		
6	π^-	0.958	0.985	0.060	16.04/16	0.450
	K^-	0.987	0.931	0.200		
	π^+	0.962	1.058	0.098		
	K^+	0.973	0.910	0.143		

Table 6.8: Run 5-6 GENIE fake data results. A GENIE sample is used as fake data with NEUT as MC and, due to the different models, cross section and FSI uncertainties are included in the fit. The true values are the ratio of true events in the data set to the expected number given by the MC and scaled by the relative size. The results for all runs agree well with the true values and the p-values indicate that all the fits have performed well.

Chapter 7

Results and Conclusions

The FHC fit is performed for runs 2-4 individually and then collectively, using the method described in section 5.1.4. The results for runs 2-4, shown in figures 7.1-7.4, are given in table 7.1 and show agreement at the 1σ level with the data-MC ratios presented in [85].

The RHC fit results in table 7.2 show some differences between runs 5 and 6 in the antineutrino selection, shown in figures 7.5 and 7.6. The low statistics for run 5 result in uncertainties which are significantly higher than for run 6, leaving the results in agreement with each other and the nominal MC at the 1-2σ level. This difference is also seen in the data-MC ratios in [88].

Run	Parent	Fitted value	Fit uncertainty	$\chi^2/D.o.F$	p value
2	π^+	1.071	0.057	6.45/8	0.597
	K^+	0.989	0.116		
3	π^+	1.087	0.056	5.62/8	0.690
	K^+	1.089	0.120		
4	π^+	1.092	0.053	10.58/8	0.227
	K^+	0.970	0.108		
2-4	π^+	1.080	0.039	11.19/8	0.191
	K^+	0.981	0.080		

Table 7.1: Run 2-4 results. All fitted values for FHC running are consistent with the nominal MC at the two sigma level and also with the data-MC ratios in [85]. The p-values indicate that all the fits have performed well, as described in section 5.1.1.
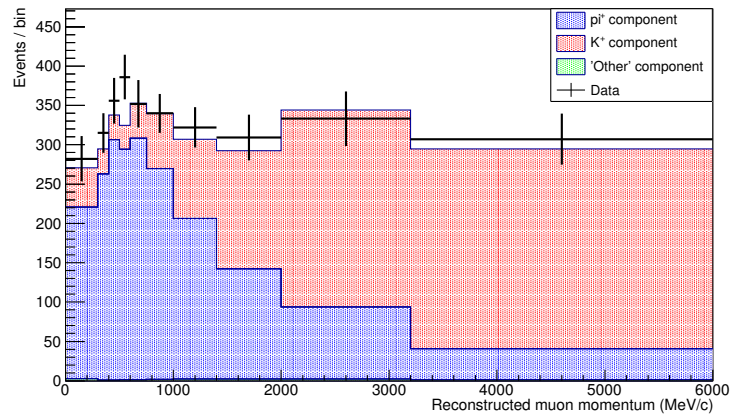
(a) Run 2 data prefit
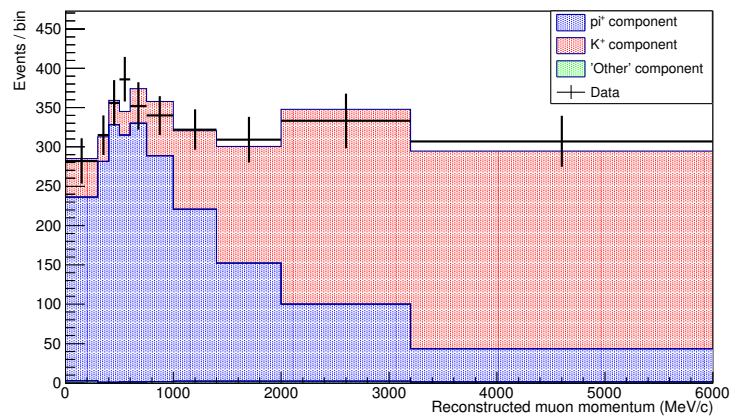
(b) Run 2 data postfit
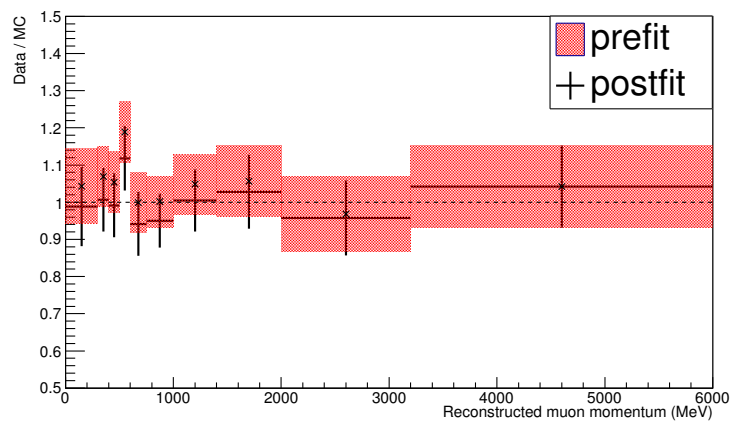
(c) Run 2 data/MC ratio

Figure 7.1: Run 2 data prefit, postfit and data/MC ratio distributions using NEUT MC to create the coloured templates. The errors shown are statistical plus the full shape-only systematic uncertainties.
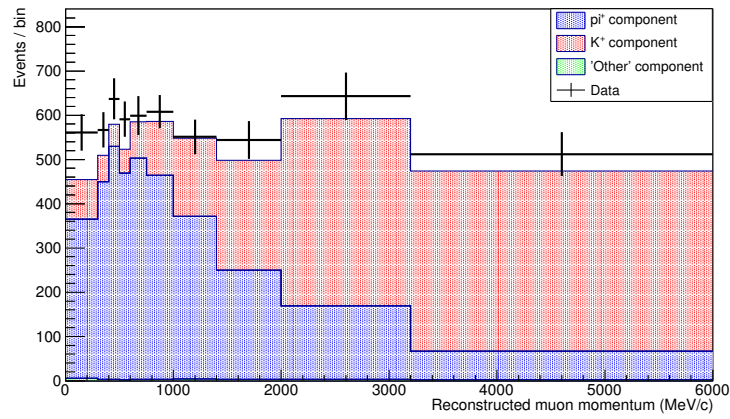
(a) Run 3 data prefit
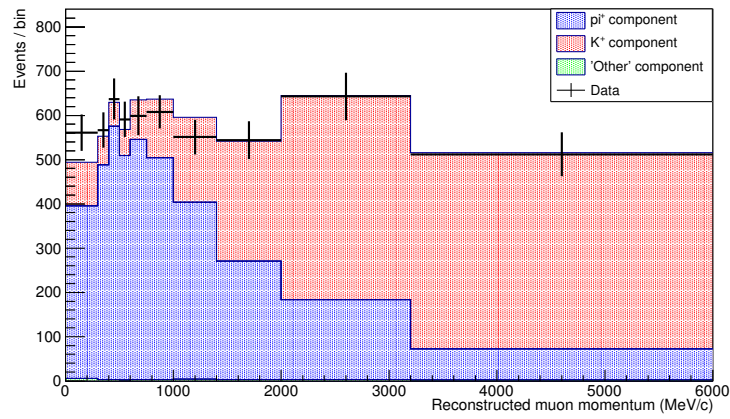
(b) Run 3 data postfit
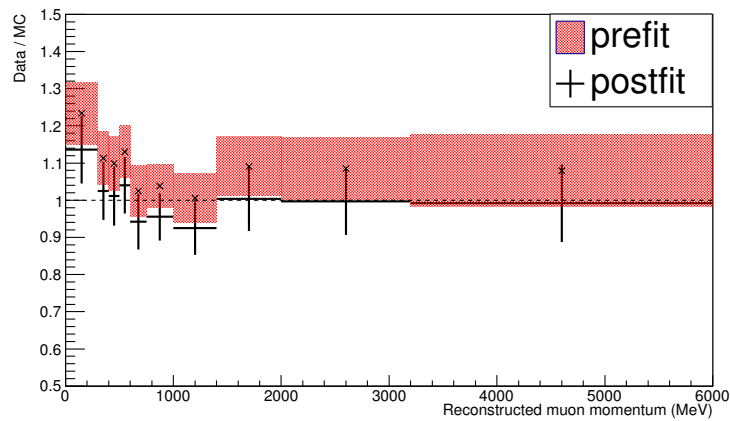
(c) Run 3 data/MC ratio

Figure 7.2: Run 3 data prefit, postfit and data/MC ratio distributions using NEUT MC to create the coloured templates. The errors shown are statistical plus the full shape-only systematic uncertainties.
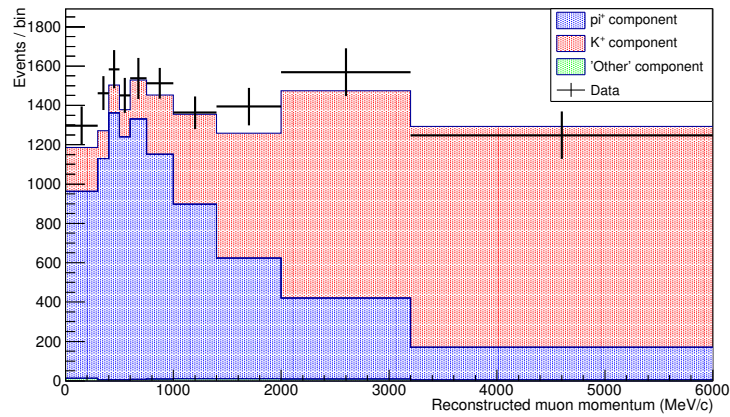
(a) Run 4 data prefit
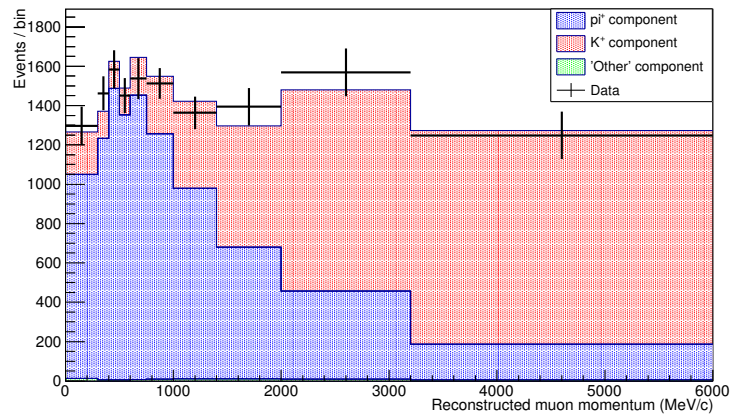
(b) Run 4 data postfit
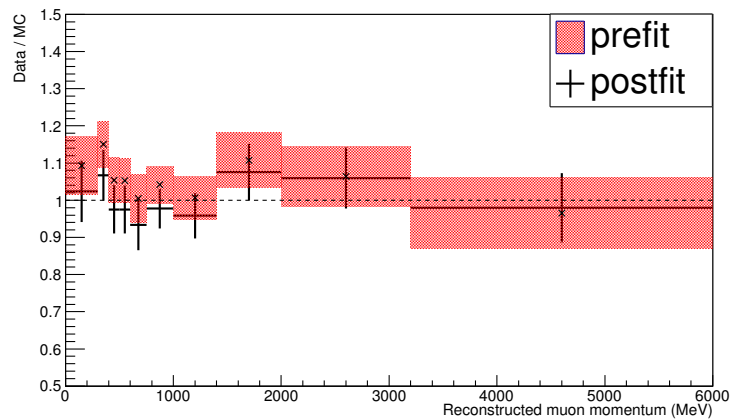
(c) Run 4 data/MC ratio

Figure 7.3: Run 4 data prefit, postfit and data/MC ratio distributions using NEUT MC to create the coloured templates. The errors shown are statistical plus the full shape-only systematic uncertainties.
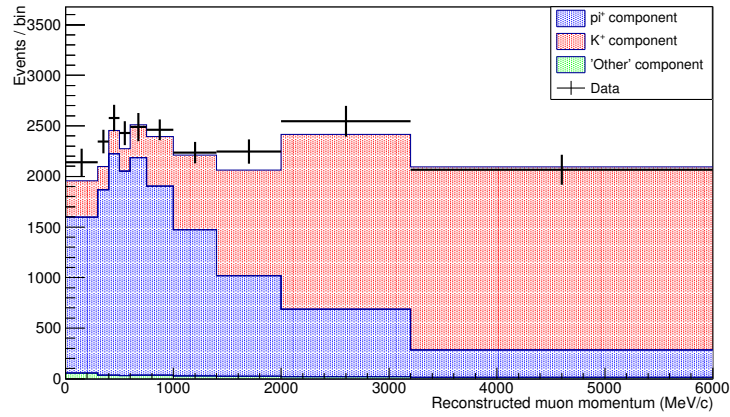
(a) Runs 2-4 data prefit
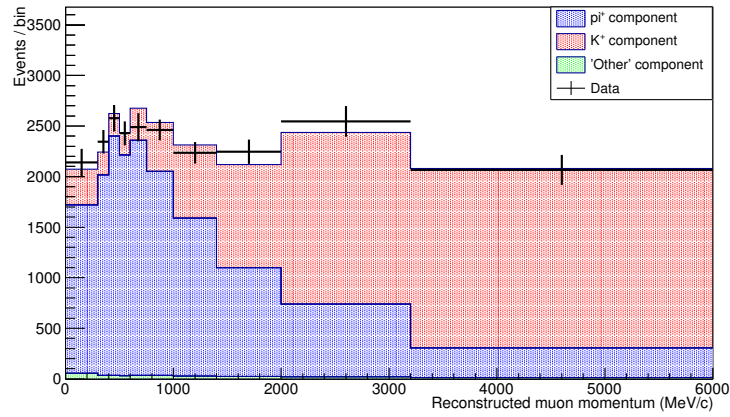
(b) Runs 2-4 data postfit
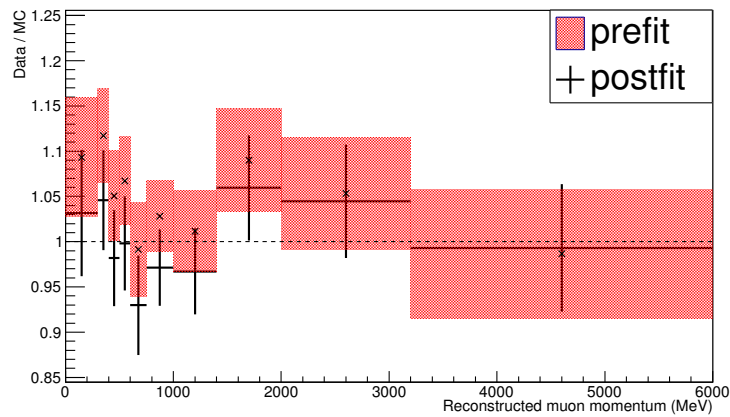
(c) Runs 2-4 data/MC ratio

Figure 7.4: Runs 2-4 data prefit, postfit and data/MC ratio distributions using NEUT MC to create the coloured templates. The errors shown are statistical plus the full shape-only systematic uncertainties.
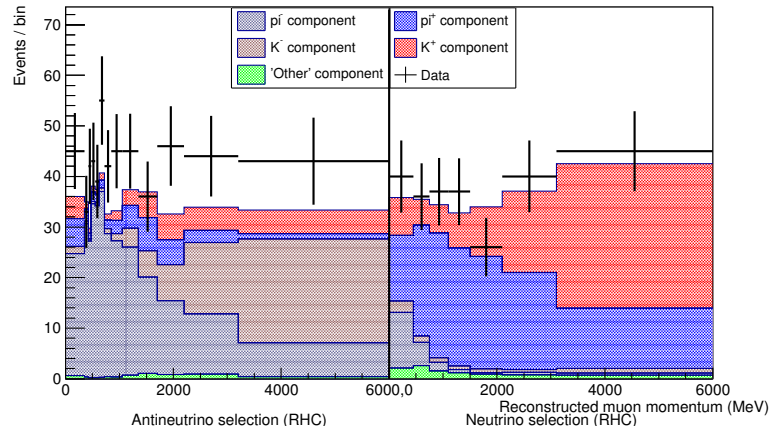
(a) Run 5 data prefit
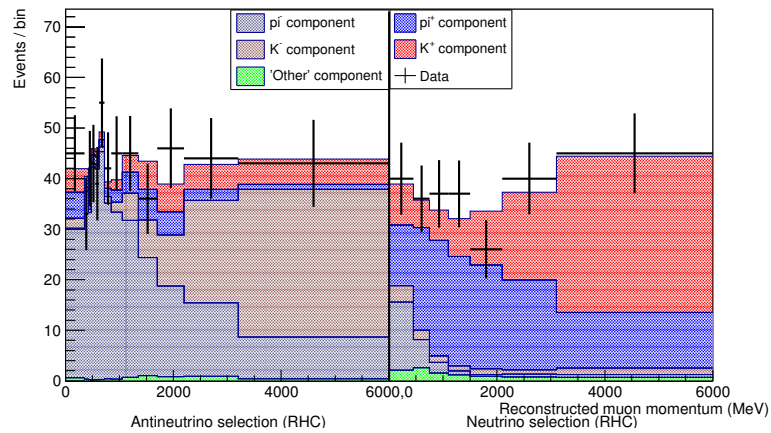
(b) Run 5 data postfit
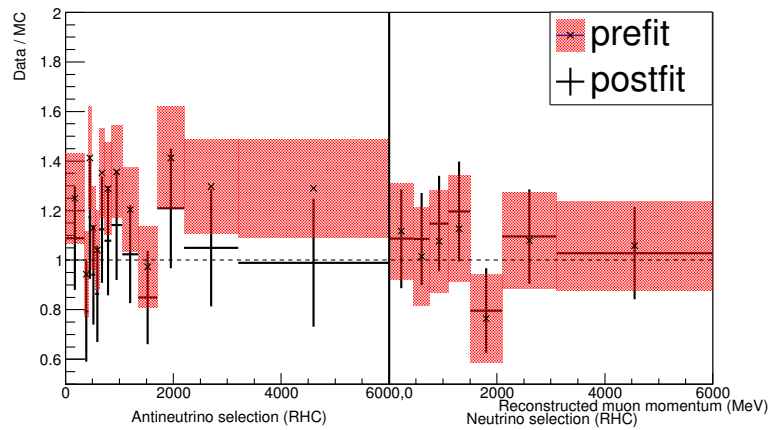
(c) Run 5 data/MC ratio

Figure 7.5: Run 5 data prefit, postfit and data/MC ratio distributions using NEUT MC to create the coloured templates. The errors shown are statistical plus the full shape-only systematic uncertainties.
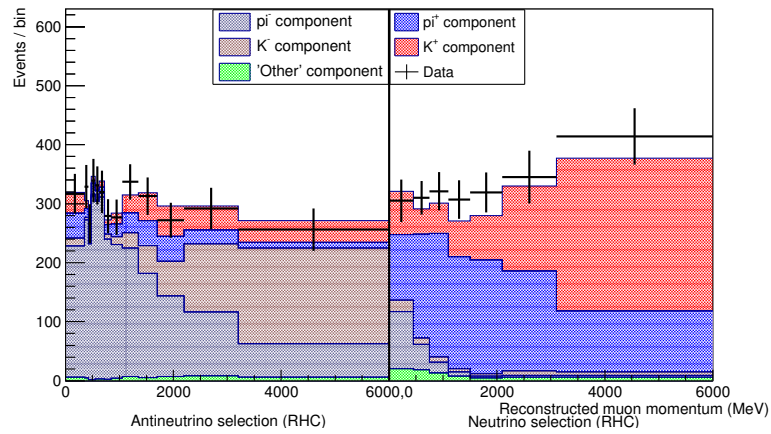
(a) Run 6 data prefit
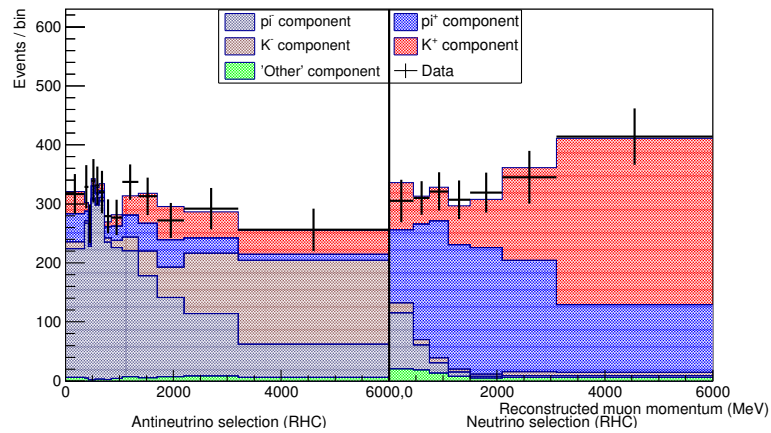
(b) Run 6 data postfit
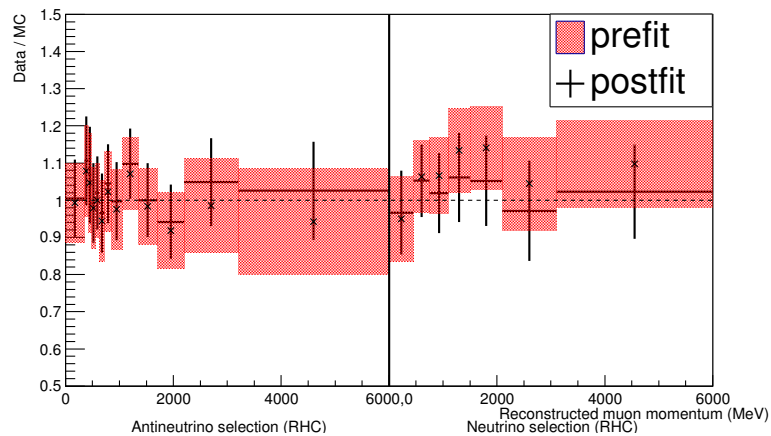
(c) Run 6 data/MC ratio

Figure 7.6: Run 6 data prefit, postfit and data/MC ratio distributions using NEUT MC to create the coloured templates. The errors shown are statistical plus the full shape-only systematic uncertainties.

| Run	Parent	Fitted value	Fit uncertainty	$\chi^2/D.o.F$	p value
5	π^-	1.225	0.115	11.04/16	0.807
	K^-	1.428	0.413		
	π^+	0.926	0.191		
	K^+	1.089	0.182		
6	π^-	0.980	0.069	6.34/16	0.984
	K^-	0.880	0.230		
	π^+	1.113	0.124		
	K^+	1.089	0.182		

Table 7.2: Run 5-6 results. All but one of the fitted values for RHC running are consistent with the nominal MC at the one sigma level and also with data-MC ratios in [88]. The p-value for run 6 indicates better than expected agreement at the 0.95 significance level however this is the only significant point from six data fits.

Figure 7.7 shows the fitted results and uncertainties for all runs. From this we see that the positive meson contributions are stable over time during the FHC running. For the RHC data it is not possible to draw conclusions on the stability due to the large uncertainties on run 5 due to the low statistics and only two data points.

The results show good agreement with the flux models based on the results from NA61, as shown in figures 7.8 and 7.9, and do not indicate any change in neutrino parent yields over time. The limiting factors are the normalisation uncertainties, discussed in section 5.1, on the MC which, at around 10-15%, are significantly larger than the uncertainties given by the fit which incorporates shape and statistical uncertainties. However, due to the normalisation uncertainties being fully correlated the relative yields of neutrino parents relative to each other is unaffected.

The normalisation uncertainties on the flux would be reduced when new results from NA61, using a replica T2K target, are incorporated into the flux models. This would then allow improved cross-section measurements, reducing the uncertainties further.
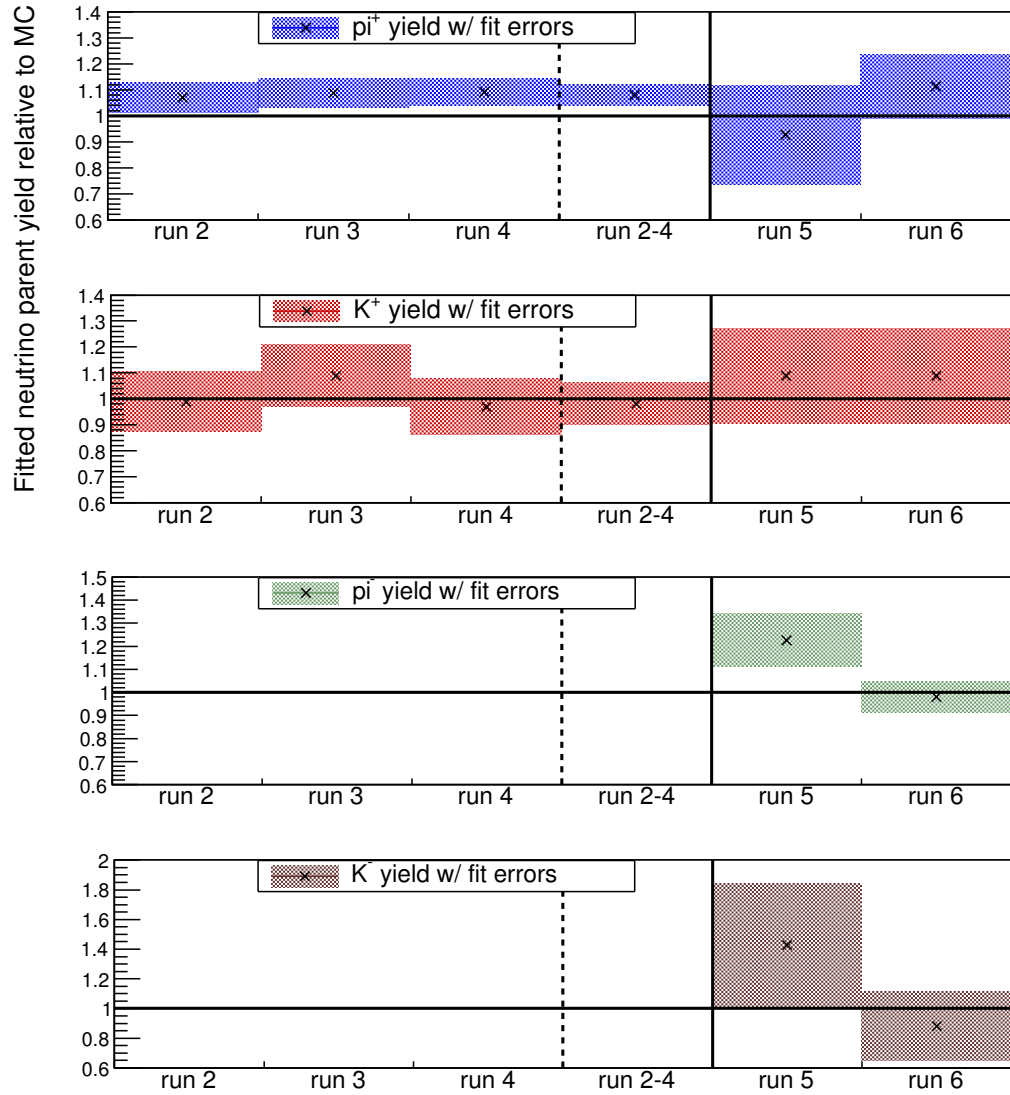
Figure 7.7: All fit results for runs 2-6 with total shape uncertainties shown.
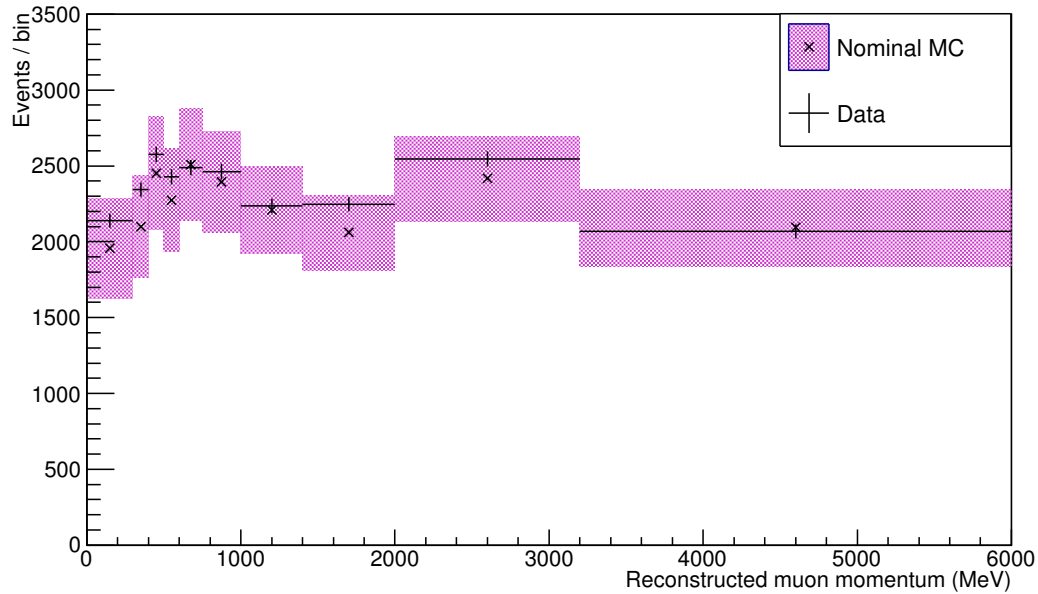
(a) Runs 2-4 prefit distribution with shape + normalisation uncertainties shown on MC and statistical uncertainties shown on data.
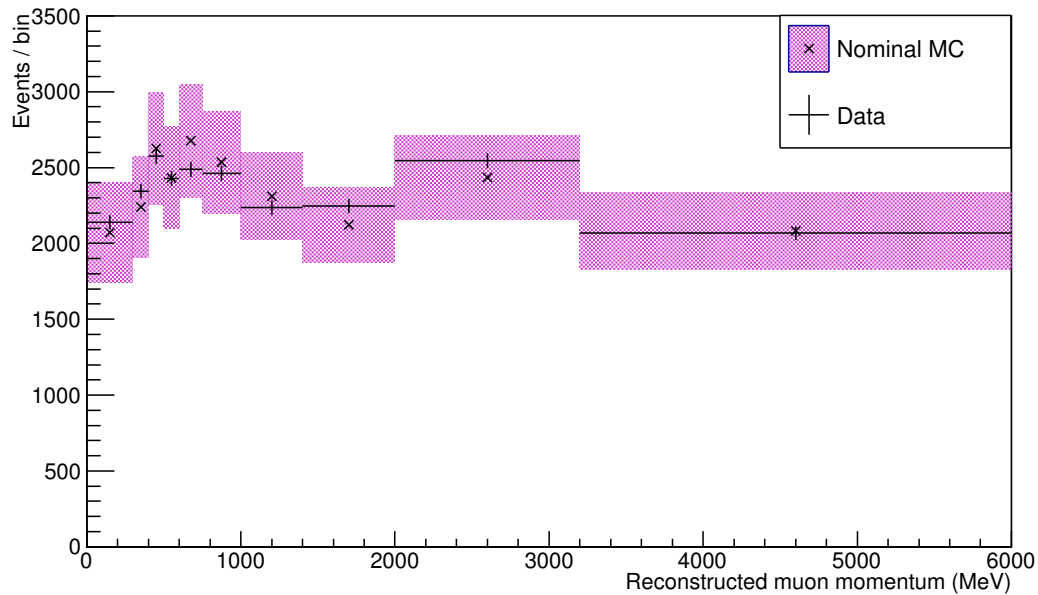
(b) Runs 2-4 postfit distribution with shape + normalisation uncertainties shown on MC and statistical uncertainties shown on data.

Figure 7.8: Runs 2-4 data prefit and postfit distributions using NEUT as MC. The errors shown on the data distribution are statistical and the MC has the full shape + normalisation systematic uncertainties applied. All data points lie within the uncertainties for both prefit and postfit distributions and therefore is consistent with the nominal flux models.
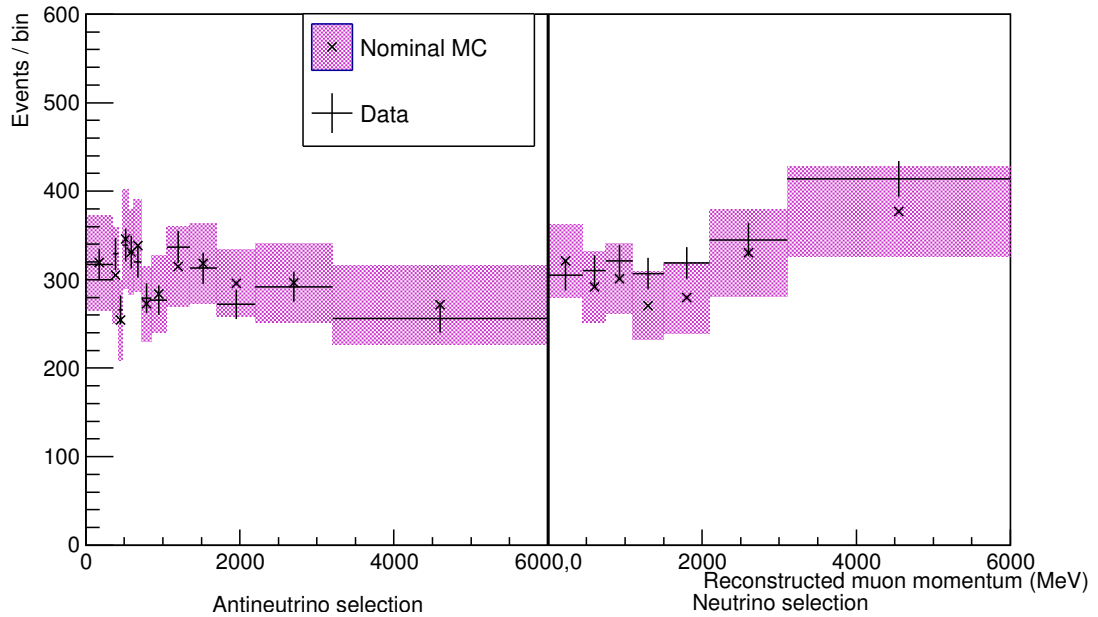
(a) Run 6 prefit distribution with shape + normalisation uncertainties shown on MC and statistical uncertainties shown on data.
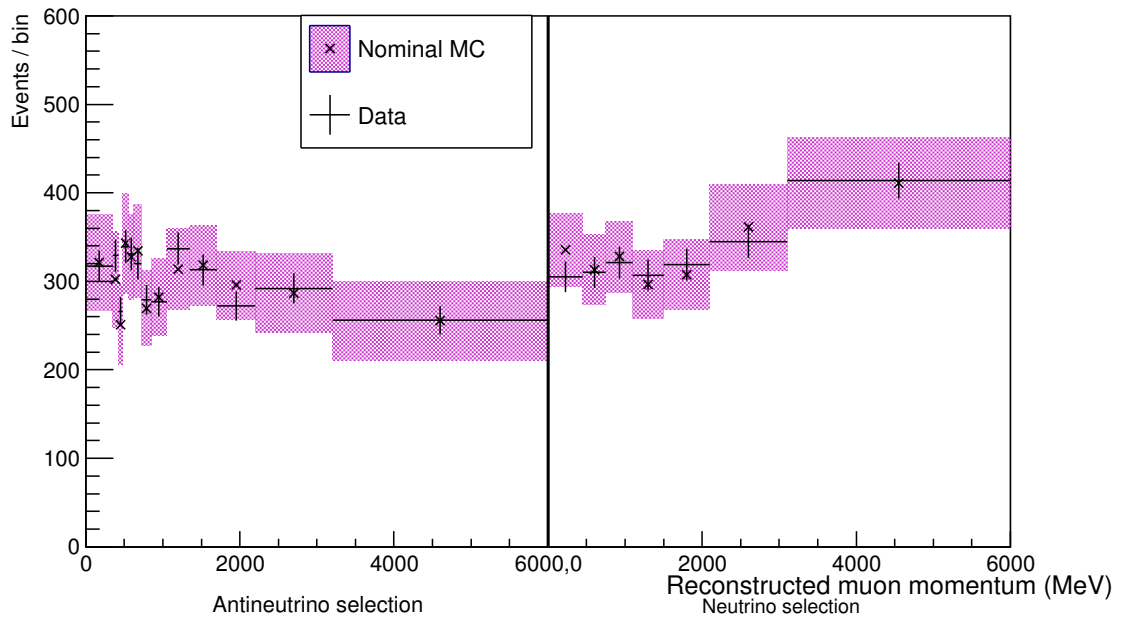
(b) Run 6 postfit distribution with shape + normalisation uncertainties shown on MC and statistical uncertainties shown on data.

Figure 7.9: Run 6 data prefit and postfit distributions using NEUT as MC. The errors shown on the data distribution are statistical and the MC has the full shape + normalisation systematic uncertainties applied. All data points lie within the uncertainties for both prefit and postfit distributions and therefore are consistent with the nominal flux models.

Chapter 8

Electron Neutrino Analysis

A reason for measuring the neutrino parent yields, is to measure the particles which are responsible for the electron (anti)neutrino contamination in the beam. This thesis has already determined the charged pion and kaon yields using ν_μ and $\bar{\nu}_\mu$ selections. The charged kaons measured are responsible for the majority of the high energy electron (anti)neutrinos. The muon (anti)neutrino analysis has the advantage over measuring the electron (anti)neutrinos directly due to the much higher statistics. Electron neutrinos make up approximately 1% of the total flux, as shown in table 3.2, making such a measurement more challenging. However there are other particles produced by the beam, such as muons and neutral kaons, which contribute to the electron (anti)neutrino signal which the muon (anti)neutrino analysis is not sensitive to. For this reason it is interesting to investigate whether a similar approach would work based around a ν_e CC inclusive selection. Run 4 was used first to determine the feasibility of this study as it is the largest FHC run used in this analysis.

8.1   Selection

This analysis is performed in FGD1 using the official T2K ν_e CC inclusive selection [93]. This selection consists of nine cuts and is described below. The first cut is identical to that used in the ν_μ analysis discussed in section 4.1.

1. Event quality

The event must have a good data quality flag and occur within a time region covering a beam bunch passing through the detector. This greatly reduces the chance of observing a cosmic muon or some delayed signal from a previous bunch, such as electrons produced by decaying muons.

2. At least one reconstructed TPC track

   The highest momentum negative track which enters the TPC is selected and required to have a momentum greater than 200 MeV/c. Below this momentum the selection is dominated by γ backgrounds in which a photon produces an electron-positron pair.

3. FGD Fiducial Volume

   The start point of the candidate track must have a reconstructed start position in the FGD1 fiducial volume, as given by: -874.51 mm $\leq x \leq$ 874.51 mm , -819.51 mm $\leq y \leq$ 929.51 mm, 136.875 mm $\leq z \leq$ 446.955 mm.

4. TPC track quality

   The candidate track must have at least 35 reconstructed nodes within the TPC. This ensures a sufficiently long track for the particle's identity to be accurately determined.

5. Particle Identification

   Particle identification is performed using information from the TPCs and ECals to identify electron-like tracks. The dE/dx information from the TPC is used to construct pull values for a given hypothesis particle. ECal information is used to discriminate between muons and electrons for tracks with a measured momentum of greater than 300 MeV/c, below this the particles cannot be reliably separated. The combination of TPC and ECal information used is dependent on which ECal is used (downstream or barrel) and more details can be found in [93].

6. Second TPC PID

If the track has a component in a second TPC that component must also not be consistent with a muon in the second TPC.

7. TPC Veto

   There must be no reconstructed TPC tracks with starting position upstream of the candidate track start position during the same bunch. This removes events upstream of the FGD which could produce an electron-like signal.

8. Pair veto

   Pair production by photons is a background to this selection due to the presence on an electron. If there is an oppositely charged track in the same event the invariant mass of the two tracks is calculated. The event is vetoed if this mass is less than 100 MeV/c^2.

9. P0D and ECal veto

   The γ background is further reduced by requiring that there must be no reconstructed P0D objects or ECal objects that start or end upstream of the candidate track start position during the same bunch.

The reconstructed momentum distribution for the electron candidates is shown in figure 8.1 broken down by neutrino parent. There are four neutrino parents which contribute a significant fraction of the events, with any remaining parents grouped as before into a final, 'other' sample. The two largest contributions are from charged pions and kaons are the same as used in the FHC ν_μ analysis in chapters 4-7. As these can be measured more easily with that analysis due to small contributions from other neutrino parents along with much higher statistics it is unlikely that this analysis will improve the measurements in chapter 7.

8.2 Systematic Uncertainties

The systematic uncertainties are generated using the method described in section 5.2. The total uncertainty is shown in figure 8.2 and is broken down by source of uncer-
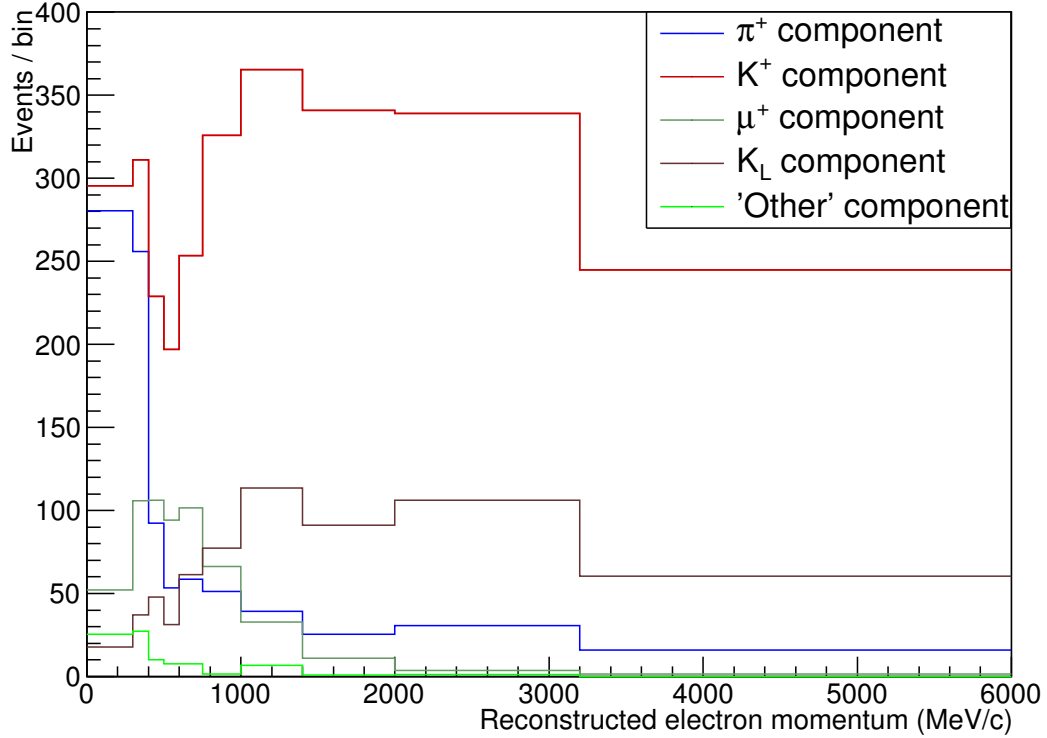
Figure 8.1: Distribution of electron candidate momentum for run 4 MC (6.72×10^{21} POT NEUT MC) divided by neutrino parent. The 'other' sample contains all events not included by the remaining samples.

tainty. The systematic uncertainties are relatively similar to those of the ν_μ and $\bar\nu_\mu$ analyses however the statistical uncertainties are much greater. The only data sample in the muon (anti)neutrino analyses that was statistically limited was run 5. The results from that fit show very large uncertainties giving little power to understanding the neutrino parent yields. This is likely to be the case again here as, due to the much lower contribution to the total flux (1%), the statistical uncertainties will be around an order of magnitude larger than for the ν_μ analysis. A combined fit using data from run 2-4 would reduce these uncertainties slightly though this would still be statistically limited.
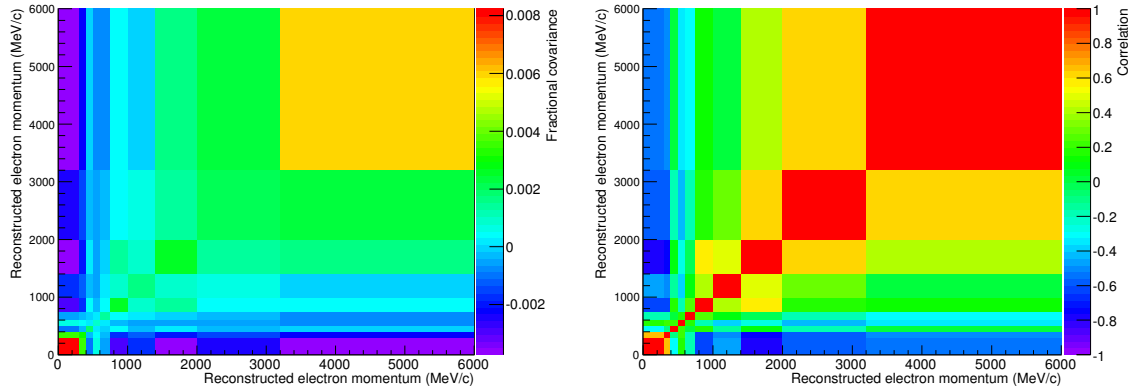
(a) Run 4 full, shape-only systematic uncertainty covariance matrix

(b) Run 4 full, shape-only systematic uncertainty correlation matrix
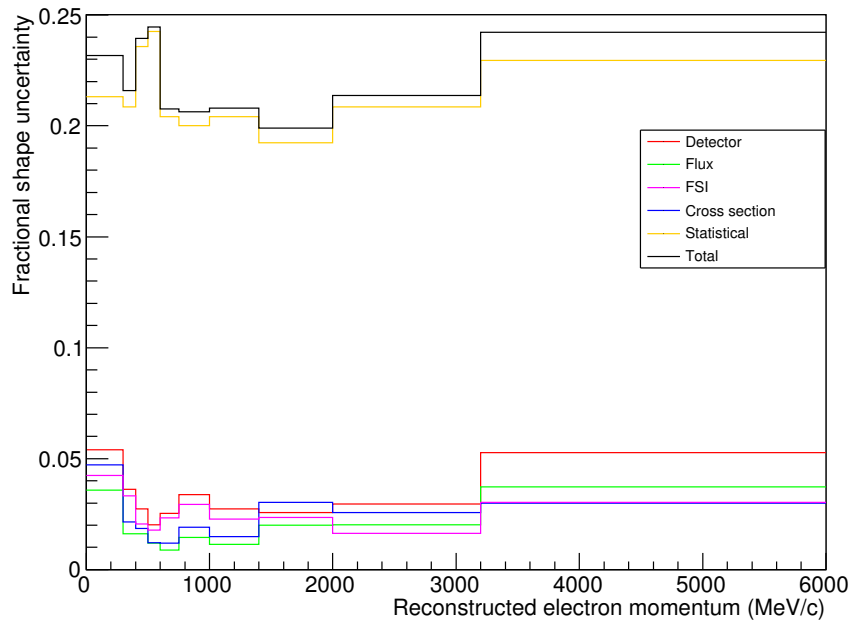
(c) Run 4 full, shape-only systematic uncertainties

Figure 8.2: The top plots show the shape-only, (a) fractional covariance and (b) correlation matrices for all run 4 (FHC) systematic uncertainties. The uncertainty on each bin (c) is the square root of the diagonal element of the covariance matrix and is show below, both as a total uncertainty and broken down by type. The off-diagonal elements of (a) and (b) show the covariance and correlation between bins respectively.

8.3 Validation Tests

To test the feasibility of this analysis the same validation tests are performed and can be compared to the previous validation studies. The same studies as performed for the muon (anti)neutrino analyses are used and consist of toy data studies along with both NEUT and GENIE fake data fits, as described in section 6. The same choice of binning was used for these studies as in the ν_μ analysis in section 5.1. This results in a roughly uniform number of events in each bin, and while the bin size could be increased to reduce the statistical uncertainties this would come at the expense of losing shape definition between neutrino parent contributions.

8.3.1 Toy Data Tests

A single set of scalings was used in the toy data sets and is presented here for comparison with previous tests with the neutrino parent yields left at the nominal values. The purpose of this is partly to test for biases, but mostly to investigate how the large uncertainties used within the fit affect the uncertainties on the fitted values. The results from this test are shown in figure 8.3. The pull means, given in table 8.1, are larger than for the ν_μ analysis but this is likely due to reduced separation between distribution making it more challenging to find the correct value.

Run	Toy set	π^+ pull mean	π^+ pull width	K^+ pull mean	K^+ pull width
4	1	-0.020	0.996	0.010	0.985

Run	Toy set	μ^+ pull mean	μ^+ pull width	K_L pull mean	K_L pull width
4	1	-0.004	0.995	0.003	0.986

Table 8.1: Means and widths for pull distributions from the ν_e toy data test. The pull means found here are larger than for the ν_μ analysis but this is likely due to reduced separation between distributions making it more challenging to find the correct value.

8.3.2 Fake Data Tests

The first fake data test uses a NEUT MC sample as the fake data. When this test was performed it was found that two of the four fitting parameters became negative. As
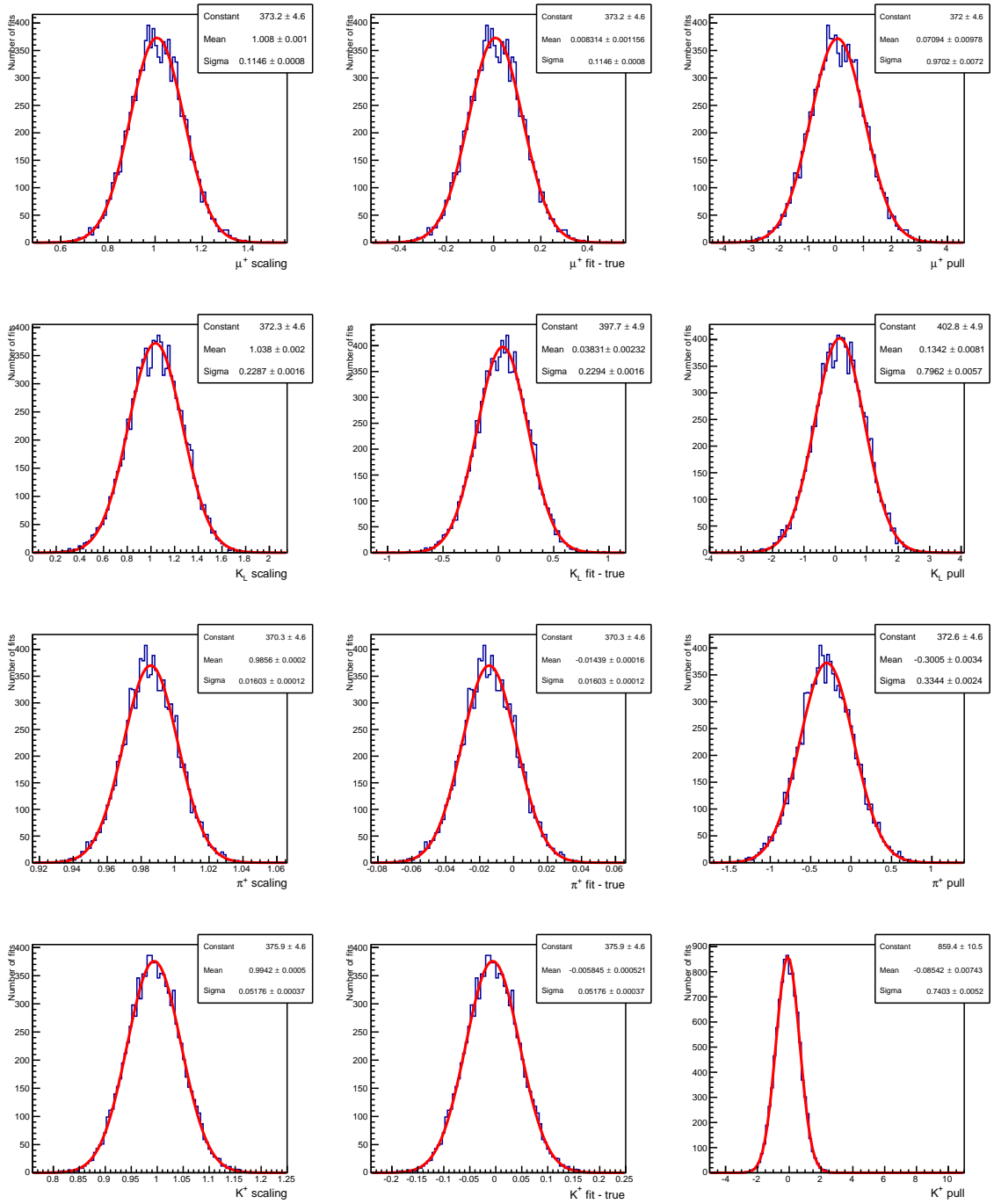
Figure 8.3: Run 4 toy data results from initial scalings set at their nominal value of one. The fit results appear Gaussian as expected however the pull means are larger than observed in the ν_μ analysis, possibly due to a larger number of significant neutrino parents and reduced shape separation between them.

such results are unphysical a lower bound of zero was applied to all four parameters. This was then repeated using a GENIE MC sample as fake data. The results of these tests are shown in figures 8.4 and 8.5 and tables 8.2 and 8.3 and show substantial deviations from the true neutrino parent yields. This poses a major problem that would need to be overcome before this analysis could be applied to data.

Run	Parent	True value	Fitted value	Fit Uncertainty	χ^2/D.o.F	p value
4	μ^+	1.286	1.644	0.447	2.88/6	0.824
	K_L	0.847	0.000	0.001		
	π^+	1.117	0.520	0.281		
	K^+	0.953	1.254	0.094		

Table 8.2: Run 4 NEUT fake data results. NEUT is used as MC with a statistically independent NEUT sample as the fake data set. The true values are the ratio of true events in the fake data set to the expected number calculated using the MC sample. The results do not agree well with the true values.

Run	Parent	True value	Fitted value	Fit Uncertainty	χ^2/D.o.F	p value
4	μ^+	1.032	2.229	0.653	6.85/6	0.335
	K_L	0.932	0.000	0.000		
	π^+	1.430	0.591	0.469		
	K^+	1.077	1.337	0.151		

Table 8.3: Run 4 GENIE fake data results. A GENIE sample is used as fake data with NEUT as MC and, due to the different models, cross section and FSI uncertainties are included in the fit. The true values are the ratio of true events in the data set to the expected number given by the MC and scaled by the relative size. The results show substantial disagreement

8.4 Constraining the Fit

As two of the parent yields, charged pions and kaons, have already been measured using a higher statistics sample it is possible to use these results to provide constraints in this analysis. This is done by altering the χ^2 equation to give:
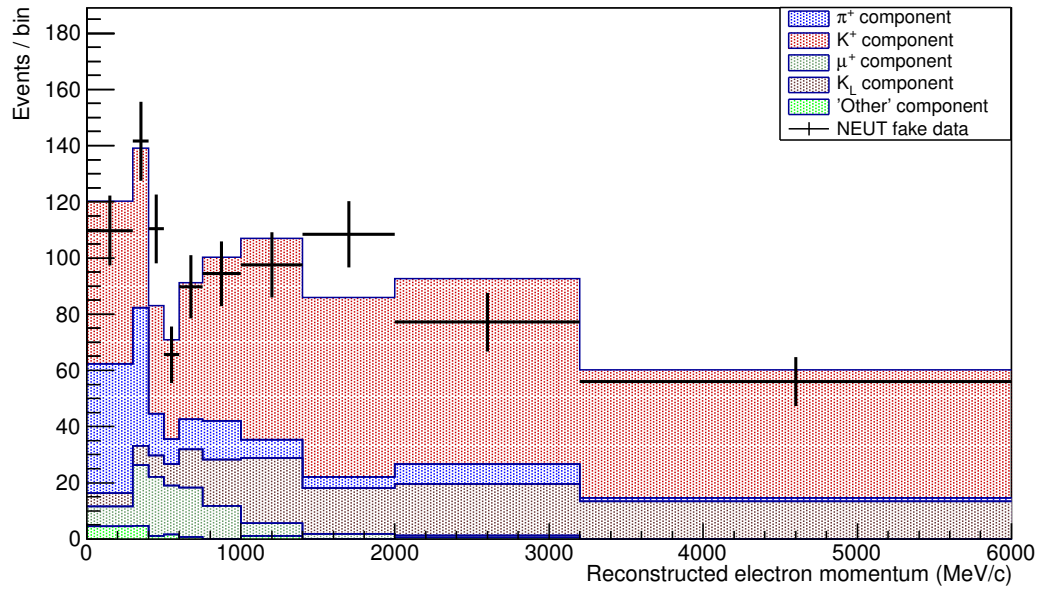
(a) Run 4 NEUT fake data prefit
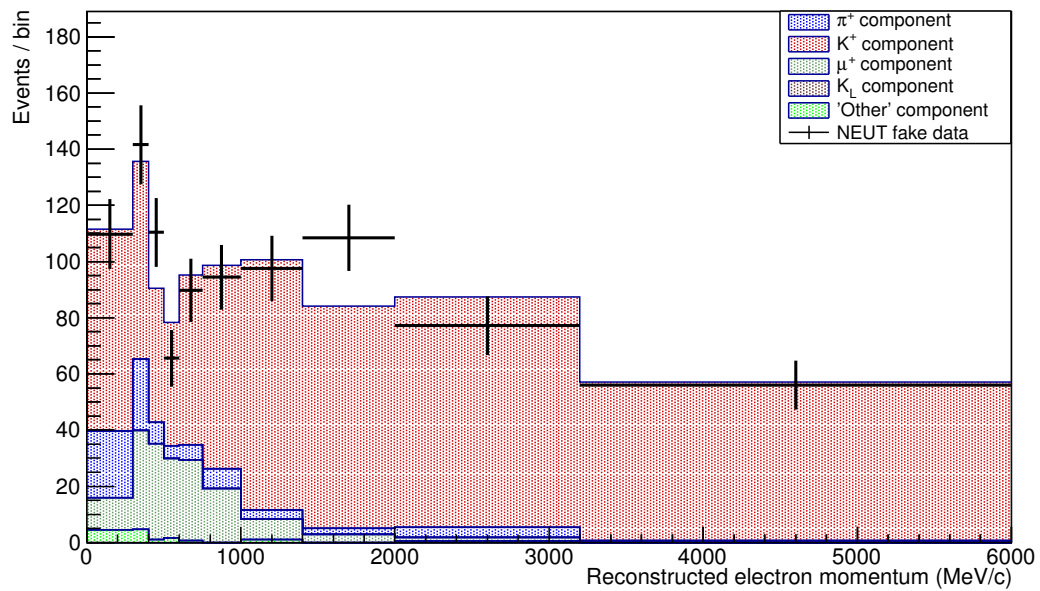
(b) Run 4 NEUT fake data postfit

Figure 8.4: Run 4 prefit and postfit distributions, using a fake data set drawn from the NEUT MC fitted using a statistically independent NEUT MC. The error bars shown are purely statistical.

(a) Run 4 GENIE fake data prefit
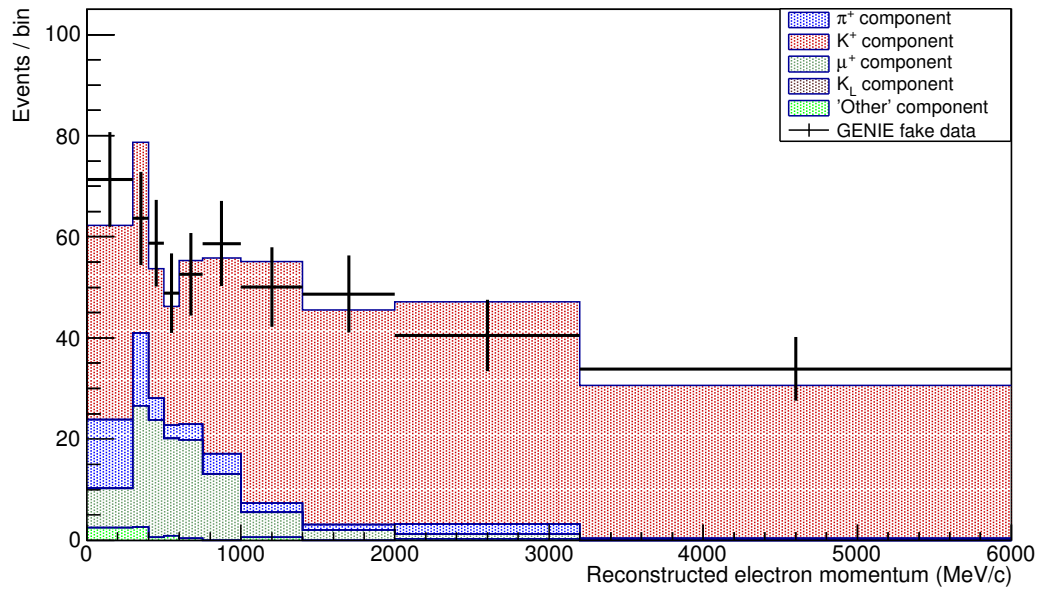
(b) Run 4 GENIE fake data postfit

Figure 8.5: Run 4 prefit and postfit distributions with a GENIE fake data sample (5.30×10^{20} POT) and NEUT as MC. Due to the different MC generators the error bars shown here include cross-section and FSI uncertainties in addition to the statistical uncertainties.

$$\chi^2 = \left(\sum_{i=1}^{N_{\text{Bins}}} (\text{D}_i - \text{MC}_i) V_{ij}^{-1} (\text{D}_j - \text{MC}_j) \right) + \left(\frac{f_{\pi^+} - \text{fit}_{\pi^+}}{\sigma_{\pi^+}} \right)^2 + \left(\frac{f_{K^+} - \text{fit}_{K^+}}{\sigma_{K^+}} \right)^2, \quad (8.1)$$

where f_{π^+} and f_{K^+} are the scale factors which change during the fit and fit_{π^+}, σ_{π^+}, fit_{K^+} and σ_{π^+} are the fitted values and uncertainties from the ν_μ analysis. D and MC are the binned data and MC distributions respectively and V_{ij} is a covariance matrix containing the relevant systematic and statistical uncertainties.

8.4.1   Revised Fake Data Tests

The NEUT and GENIE fake data tests described in section 8.3.2 are repeated with constraints applied, in order to test the effect these have on the results. For the NEUT fake data test, shown in figure 8.6, the same generators are used for both MC and fake data samples and therefore the values of fit_{π^+} and fit_{K^+} are set to one. For the GENIE fake data set, shown in figure 8.7, the values are set to the fitted results from the run 4 GENIE test in section 6.2.2. The results of these tests are given in tables 8.4 and 8.5 for NEUT and GENIE respectively.

Run	Parent	True value	Fitted value	Fit Uncertainty	χ^2/D.o.F	p value
4	μ^+	1.286	1.346	0.345	3.38/6	0.760
	K_L	0.847	0.713	0.326		
	π^+	1.117	1.009	0.021		
	K^+	0.953	1.008	0.036		

Table 8.4: Run 4 NEUT fake data results with constraints from ν_μ analysis. NEUT is used as MC with a statistically independent NEUT sample as the fake data set. The true values are the ratio of true events in the fake data set to the expected number calculated using the MC sample. The results agree much better with the true values than they did without the constraint applied, with three out of four parameters within one sigma and the remaining parameter within two sigma of the true values.
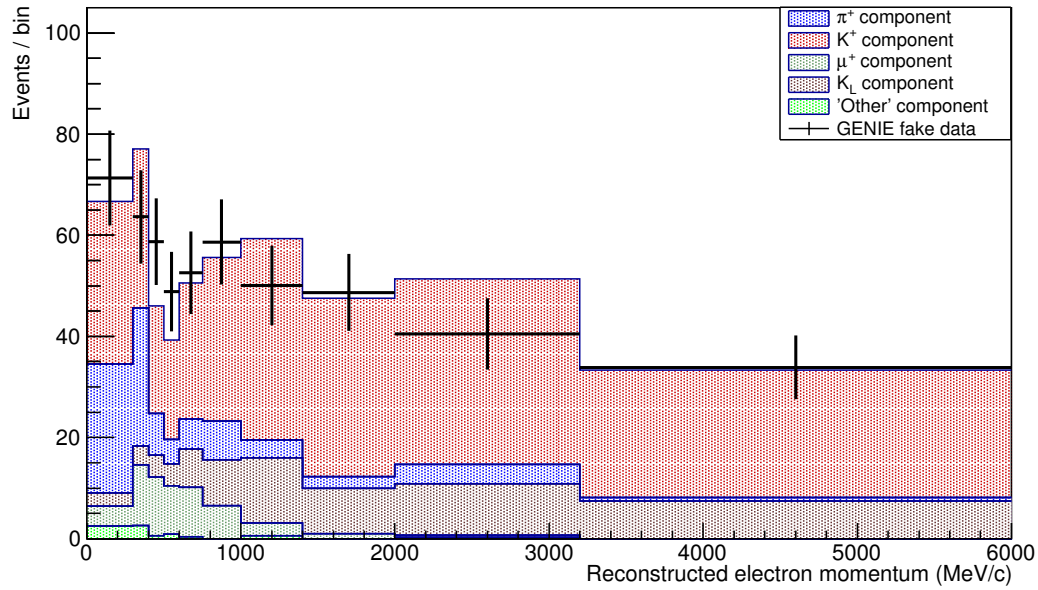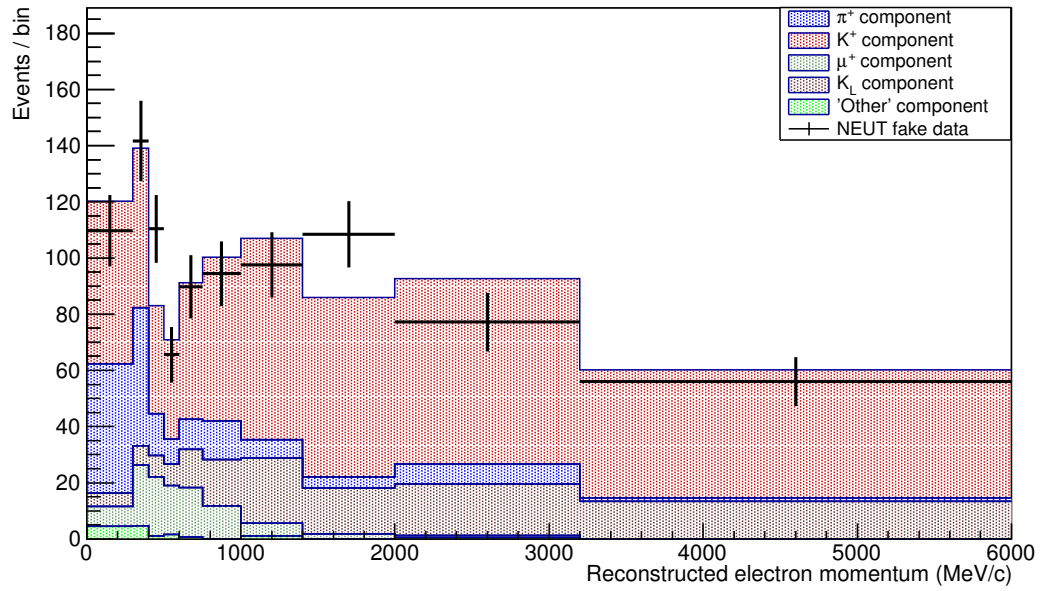
(a) Run 4 NEUT fake data prefit
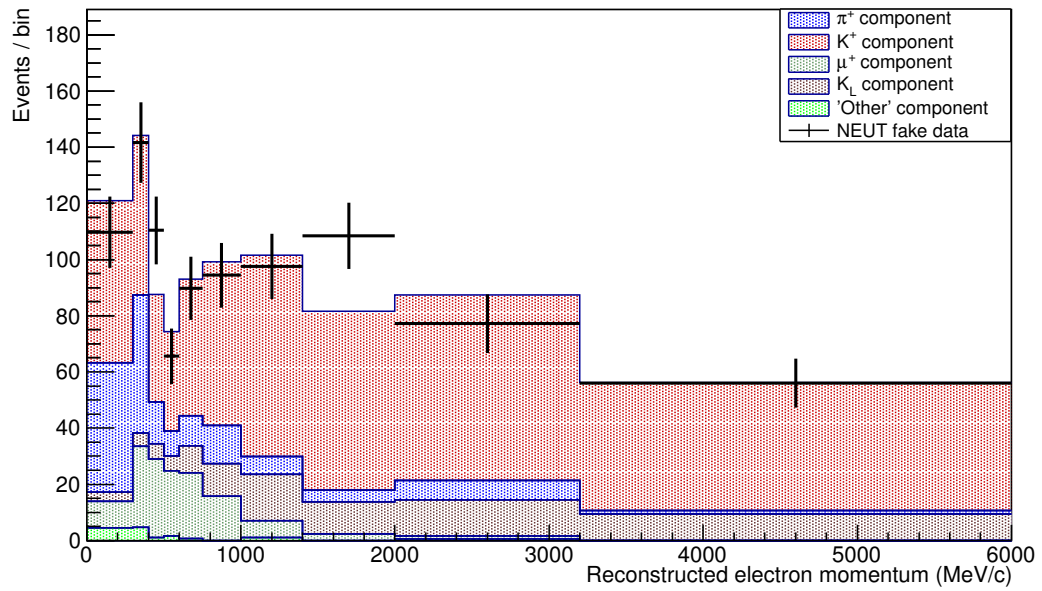
(b) Run 4 NEUT fake data postfit

Figure 8.6: Run 4 prefit and postfit distributions with constraints from ν_μ analysis, using a fake data set drawn from the NEUT MC fitted using a statistically independent NEUT MC. The error bars shown are purely statistical.

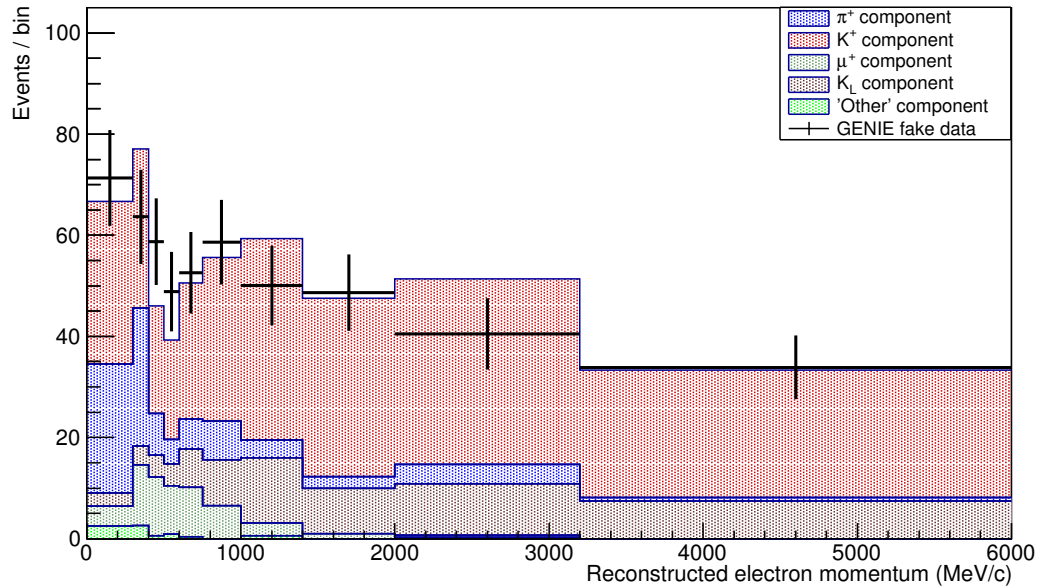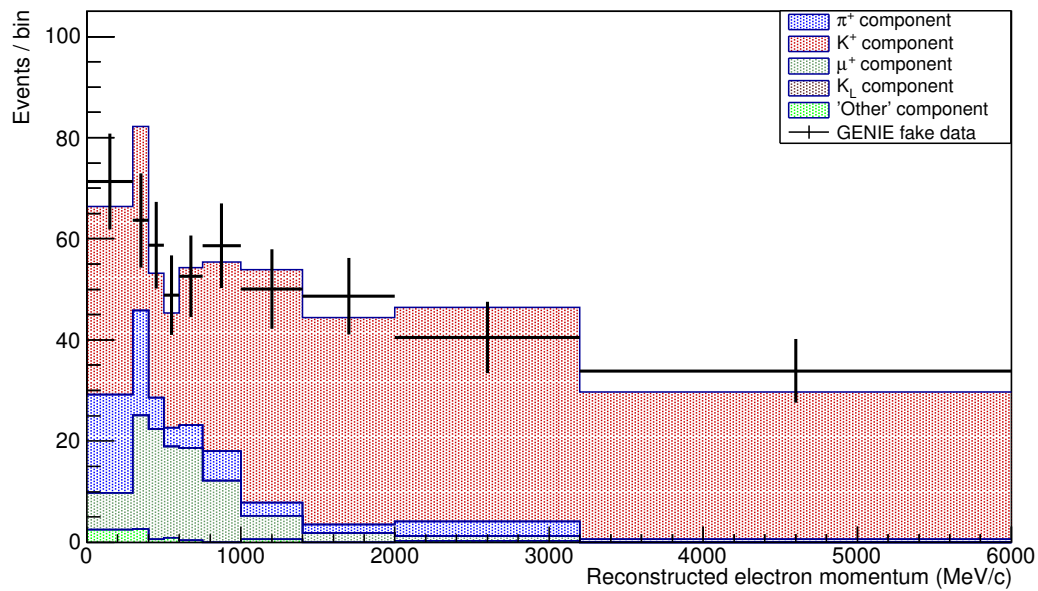(a) Run 4 GENIE fake data prefit

(b) Run 4 GENIE fake data postfit

Figure 8.7: Run 4 prefit and postfit distributions with constraints from ν_μ analysis using a GENIE fake data sample (5.30×10^{20} POT) and NEUT as MC. Due to the different MC generators the error bars shown here include cross-section and FSI uncertainties in addition to the statistical uncertainties.

Run	Parent	True value	Fitted value	Fit Uncertainty	χ^2/D.o.F	p value
	μ^+	1.032	2.087	0.616		
	K_L	0.932	0.000	0.018		
4	π^+	1.430	0.849	0.343	7.71/6	0.260
	K^+	1.077	1.291	0.136		

Table 8.5: Run 4 GENIE fake data results with constraints from ν_μ analysis. A GENIE sample is used as fake data with NEUT as MC and, due to the different models, cross section and FSI uncertainties are included in the fit. The true values are the ratio of true events in the data set to the expected number given by the MC and scaled by the relative size. The results of the constrained fit are still not in agreements with the expected values.

8.5   Conclusions

The validation tests that were previously successful have not worked reliably for this selection. The main reason likely to be behind this is that the different neutrino parent contributions have less shape difference for this selection than the selections used for the other analyses. This is most clearly seen in the K^+ and K_L samples which show very little shape difference. It was hoped that using the measurements from the ν_μ analysis could be used to constrain the charged meson yields sufficiently however this proved unsuccessful. This results in less fitting power and less reliable results, as seen in section 8.3.2.

The limiting factor for this analysis is the statistical uncertainties at around 20% for run 4. A combined fit using data from runs 2-4 and run 8 would increase the statistics by a factor of less than two resulting in statistical uncertainties similar to those for the $\bar{\nu}_\mu$ analysis which has better separation between neutrino parents. For this reason this analysis is not performed in this thesis but it may be possible to carry this out using later, higher-statistics runs along with the ν_μ analysis constraints in the future.

Chapter 9

Overall Conclusions and Future Work

This thesis set out to provide a cross check of the flux models used by the T2K experiment using data collected with the ND280 detector for events starting within FGD1. The flux models are based on hadron measurements by NA61 using a thin target. These measurements contain information about the hadrons that leave the thin target but do not cover the effects of increasing the target length and the presence of downstream elements, such as the magnetic horns. It is therefore important to provide an *in-situ* cross-check of these models to confirm that the observed neutrino parent yields are in agreement with the flux model. The conclusions of that work are presented in this chapter along with relevant ideas for potential future work.

9.1 Conclusions

The work presented in this thesis used a ν_μ CC inclusive selection for FHC runs and both ν_μ and $\bar{\nu}_\mu$ CC inclusive selections for RHC runs to measure the neutrino parent yields relative to the flux model. These selections were found to give good separation in reconstructed muon momentum for events from neutrinos from different parents. Muon momentum was used rather than attempting to reconstruct the neutrino energy due to the large model dependencies especially for higher energy events which

require a large number of particles to be accurately reconstructed. The reconstructed momentum for selected muons formed a histogram which was fit to using templates created from NEUT MC.

The analysis was performed for FHC runs 2-4 both separately and combined as well as for RHC runs 5 and 6 separately. No joint RHC fit was performed as, due to the relative size of the two runs, the results would have little effect compared to the run 6 results.

Previous results from [78], using FHC runs 1 and 2, measured best fit values for π^+ and K^+ yields of 0.775 and 0.855 respectively. The 2D distribution was consistent with the nominal values at the 1σ level. Later results [79], using runs 2 and 3, measured best fit values for π^+ and K^+ yields of 0.98 and 1.06 respectively, and is also consistent with the nominal values at the 1σ level. Both analyses show uncertainties typically around the 20% level, however these include normalisation uncertainties.

This analysis differs from previous FHC results by using a shape-only fit and also provides the first measurement using RHC data. The shape-only method allows for comparison of the neutrino parent yields relative to each other with substantially reduced uncertainties. The normalisation uncertainties can then be added on a bin-by-bin basis to the final distribution, as shown in figures 7.8 and 7.9.

The results from all fits performed are consistent with the nominal flux models and thus support the results from NA61/SHINE and the modelling of the beamline components such as the horns. The limiting factor to this analysis are normalisation uncertainties on the cross section models, at around 10%. As the normalisation uncertainties are fully correlated the relative scale of neutrino parents relative to each other is not affected.

The results show good agreement with the flux models and are consistent with the neutrino parent yields measured by NA61/SHINE using thin target data. It also appears that these yields are stable over time.

A ν_e analysis was also explored in chapter 8 however due to the very low statistics and lack of separation between neutrino parents it was decided not to proceed with this approach without more data becoming available.

Current work implementing results from NA61/SHINE using a replica T2K target is expected to reduce the flux uncertainties to approximately half the current values. This will result in improved precision in cross-section measurements. The combined reduction of these systematic errors would allow greater sensitivity to differences between the observed and expected neutrino parent yields. It may also be possible to utilise differences in the flux as a function of off-axis angle to further test these results.

9.2 Future Work

The hadron decays that produce the T2K neutrino beam described in section 3.7 provide two potential differences between neutrino parents. This thesis investigates the effect on neutrino energy, and therefore lepton momentum for CC events, however the dependence on off-axis angle is not explored. Figure 3.16 showed the changes in the neutrino energy distribution between on-axis and 2.5° off-axis.

While this can be a substantial change, FGD1 is not the ideal place to make a measurement using this effect. The reason for this is that at only 2 m in size and approximately 280 m downstream of the target it only subtends an angle of 0.4°. There are, however, other detectors which are better suited to this type of measurement. The best candidates for this are the ND280 ECals, at around 3 m in size, or INGRID which, at 10 m in size and centred on the beam axis, spans a range from $0 - 1°$ off-axis. Figure 9.1 shows the difference in number of interactions in different ECal regions normalised by mass. There is a clear gradient from most on-axis (bottom-left) to least on-axis (top-right). A similar effect is seen in figure 9.2 which shows the number of events in different INGRID modules along the horizontal and vertical parts of the cross structure.

9.2.1 ECal-as-target

The ECals were not originally designed to be used as a target. Unsurprisingly this means there are several challenges that need to be overcome before such an analysis is possible.
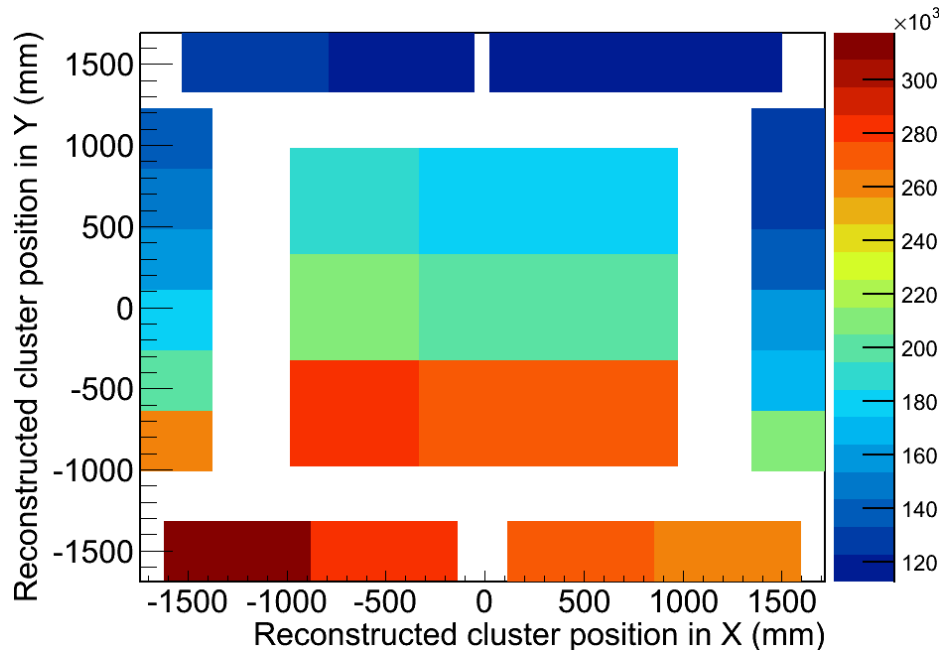
Figure 9.1: Number of events in equal mass regions of the ECals showing the variation with off-axis angle from most on-axis (bottom-left) to least on-axis (top-right) [94].
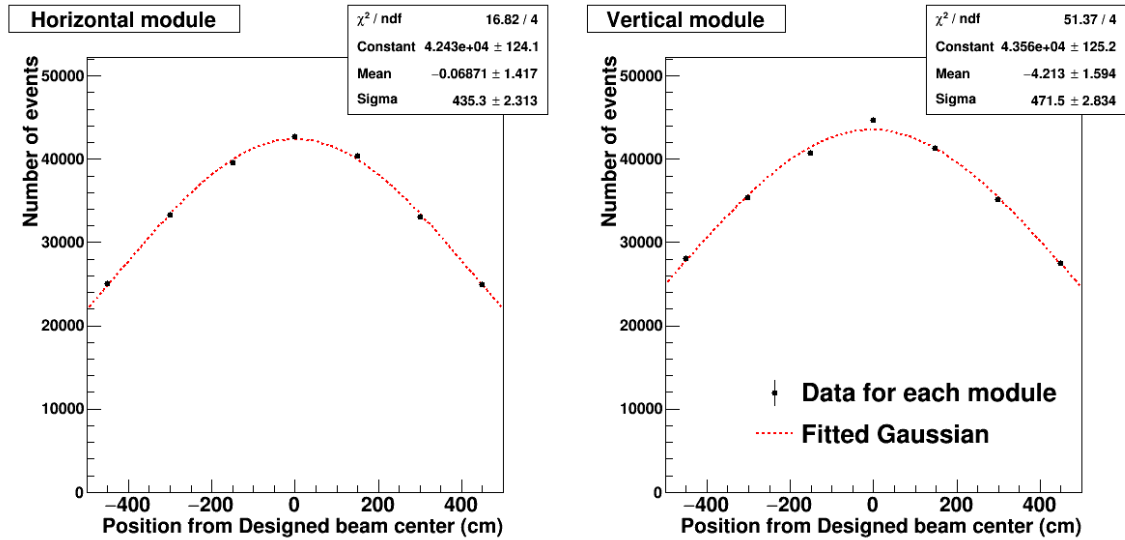

Figure 9.2: The number of events for each INGRID module is plotted for both horizontal and vertical parts of the cross structure. The peak shows the beam centre location [95].

Due to the required resolution, the scintillator bar cross sections are larger in the ECals than for the FGDs reducing the resolution of the detector. Also, unlike the FGDs, one of the scintillator bar directions for the barrel ECal is along the beam axis and therefore some very forward going particles will pass through very few bars making it very difficult to accurately reconstruct the associated vertex and tracks.

Not all challenges are hardware based, the existing reconstruction was not designed to select and categorise events which begin in the ECal. However recent work has been done on reconstructing events in the ECal and developing selections [96] [97].

Due to the larger mass in the ECals relative to the FGDs there is a large increase in the number of interactions, leading to higher statistics in principle. However, given the largely forward nature of the lepton produced in CC interactions there is a smaller chance that there will be a TPC track for the lepton. As this is where the particle identification and momentum are determined requiring the same TPC track conditions as for the FGD analysis would substantially reduce the statistics. In addition, as the lepton moves from the vertex in the ECals towards the TPC some momentum is lost, which would need to be corrected for if the same procedure were to work.

There are three ways in which this work could be performed, each with their own challenges:

1. Require a TPC track

   This method would require a TPC track of the same quality as for the FGD analysis. This has the advantages that the method is largely the same as for the FGD based analyses however, requiring a TPC track also reduces the benefit of higher statistics due to the larger mass.

2. Momentum-by-range

   It is possible to use the range of the muon candidate within the ECal to estimate its momentum. This requires the muon candidate track to be fully contained by the ECal, meaning that very forward-going events would be preferentially selected. Due to the orientation of half the bars of the barrel ECal being along the beam direction, it is likely that many forward-going tracks will cross few bars

resulting in poor reconstruction. In addition to this problem, low momentum muons are more likely to be contained and therefore the high momentum events required to constrain the neutrinos produced by kaon decays may not be present.

3. Off-axis angle

   The neutrino energy from different parent decays varies differently with off-axis angle. Figure 9.3 show the number of events which pass the ν_μ selection detailed in section 4.1, broken down by neutrino parent for the two regions of FGD1 shown in figure 9.4. These regions contain a quarter of the fiducial volume each and the internal boundaries are lines of approximately constant off-axis angle. This shows an apparent drop in flux around the peak from the pion component but relatively little change in the kaon component. In order to use this method it would be necessary to check this is true for the selection used in the analysis. As the FGDs span only a small range in off-axis angle this method was not used in that analysis.

   As the ECals surround the tracking region, including the FGDs, they span a greater range in off-axis angle making them a better option to make use of this effect. If there is a significant difference between the distributions from different neutrino parents for various off-axis regions then it should be possible measure the parent yield without requiring a momentum measurement. This is likely to be the best method as the efficiency should be less sensitive to muon momentum, allowing both high and low energy events to be selected which is required to measure both charged pions and kaons.

9.2.2 INGRID

Due to the design of INGRID, described in section 3.4, and its constituent modules an analysis performed using this data would have to consider the rate of events occurring in different modules of increasing off-axis angle. This is the case as the modules are too shallow to contain many of the higher momentum muons and there is no TPC to
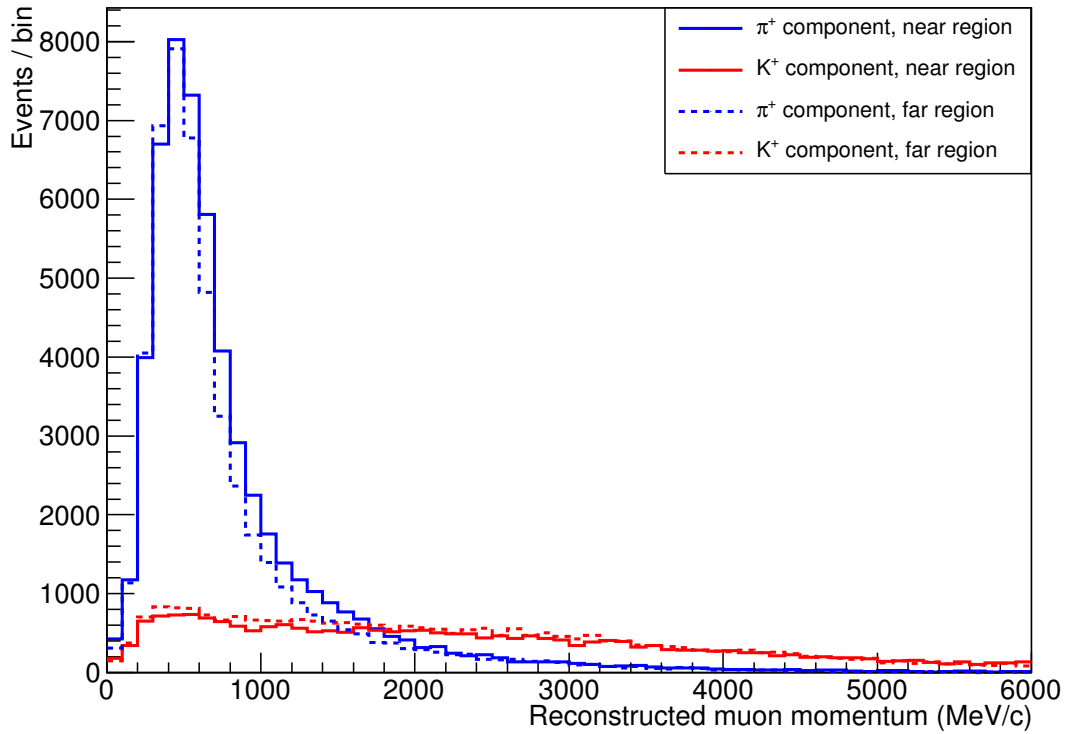
Figure 9.3: Number of events which pass the ν_μ selection detailed in section 4.1, broken down by neutrino parent for the two regions of FGD1 shown in figure 8.4.

use for momentum measurement and PID. The measurement of interaction rates as a function of position is already used to monitor the position and profile of the beam.

An INGRID analysis would have advantages over the ECal alternative as both orientations of scintillator bars are perpendicular to the beam direction making reconstruction significantly easier.
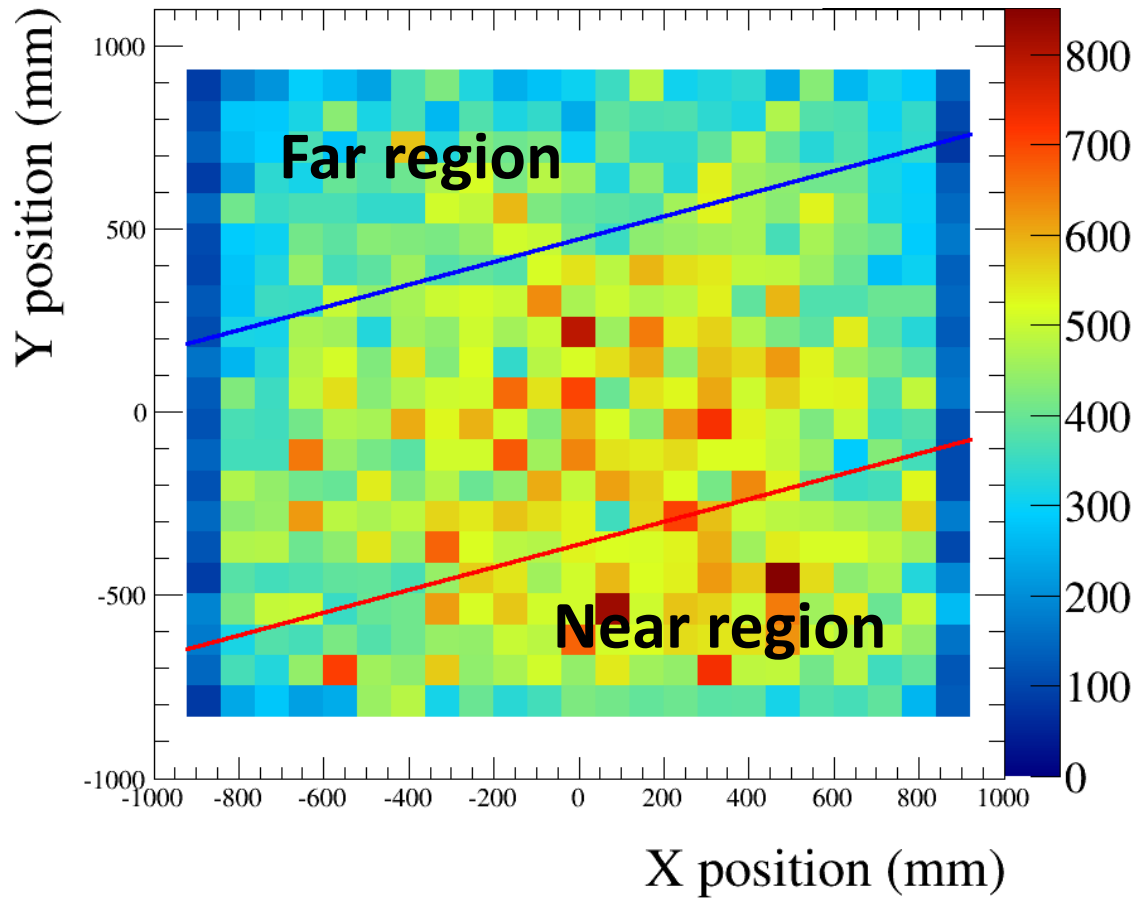
Figure 9.4: Event rate as a function of position in FGD1. The two regions defined each cover a quarter of the total fiducial volume and the internal boundary is defined at approximately constant of-axis angle. There is a clear drop in event rate from the most on-axis region to the least on-axis region.

Appendix A

Systematic uncertainties

Figures A.1 - A.5 show the fractional covariance and correlation matrices for each run broken down into detector, flux, cross section and FSI uncertainties. Due to the different sources of uncertainty each of these pairs of matrices have different features. The detector systematics behave similarly for particles with similar kinematic properties which leads to elements near the diagonal being strongly correlated. In order to preserve the overall normalisation the bins away from the diagonal anti-correlate. The flux and cross-section uncertainties are both dominated by different processes in the low and high momentum parts other distributions. In the case of the flux this is due to the different neutrino parents resulting in vastly different neutrino energy spectra. The cross section is dominated by CCQE interactions at low energies but other modes become dominant at higher energies. This energy dependence leads to strong anti-correlations between the low and high muon momentum regions. The final set of uncertainties deal with which particles make it out of the nucleus following the interaction. As this analysis uses an inclusive muon selection these uncertainties are generally the smallest and often at their largest in the lowest momentum bin.
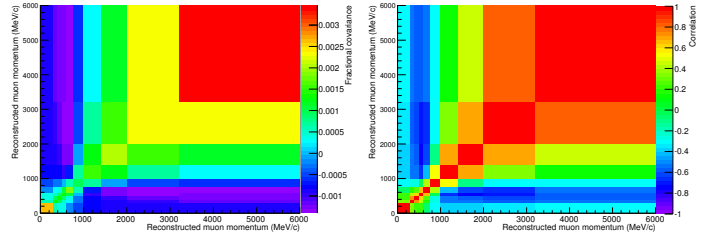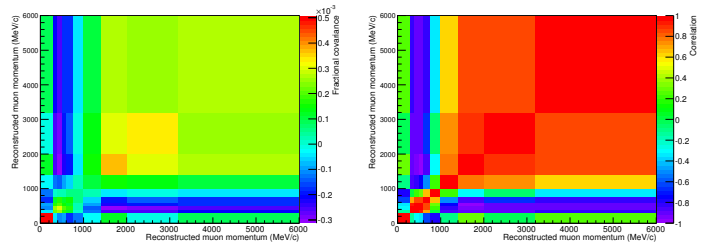
(a) Run 2 detector systematics covariance matrix

(b) Run 2 detector systematics correlation matrix
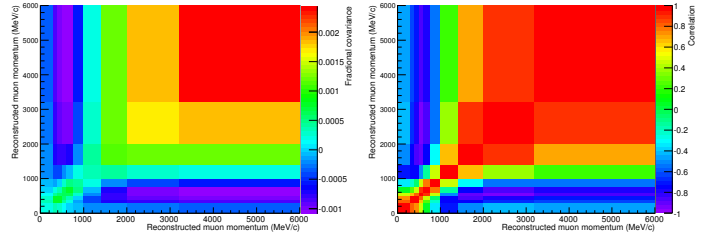
(c) Run 2 flux systematics covariance matrix

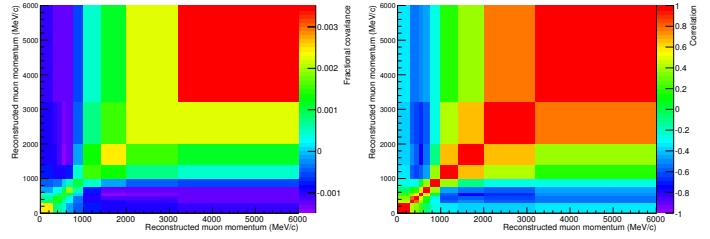(d) Run 2 flux systematics correlation matrix
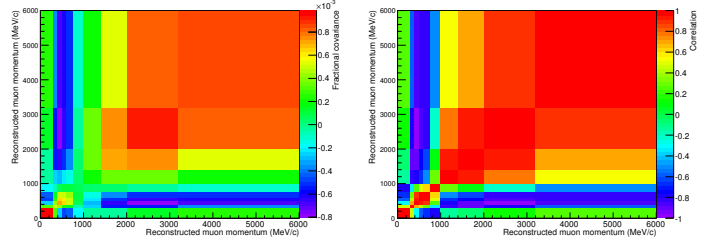
(e) Run 2 cross-section covariance matrix

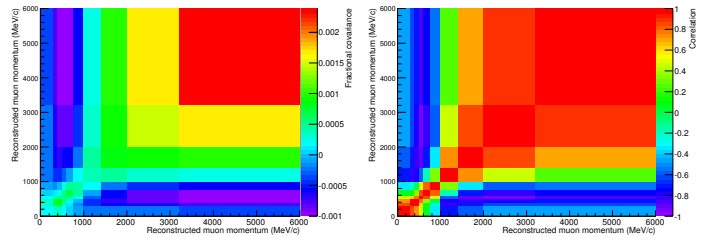(f) Run 2 cross-section systematics correlation matrix

(g) Run 2 FSI systematics covariance matrix
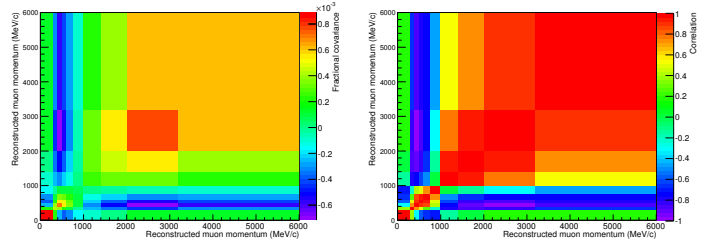
(h) Run 2 FSI systematics correlation matrix

Figure A.1: Run 2 systematics broken down into detector, flux, cross section and FSI matrices.
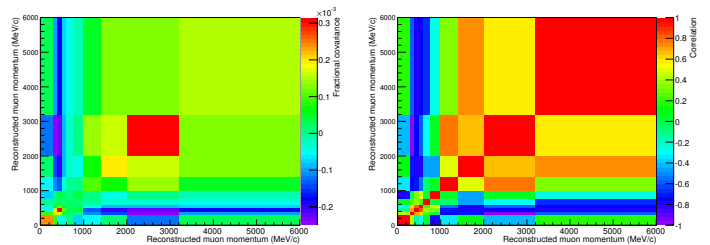
(a) Run 3 detector systematics covariance matrix

(b) Run 3 detector systematics correlation matrix

(c) Run 3 flux systematics covariance matrix

(d) Run 3 flux systematics correlation matrix

(e) Run 3 cross-section covariance matrix

(f) Run 3 cross-section systematics correlation matrix

(g) Run 3 FSI systematics covariance matrix

(h) Run 3 FSI systematics correlation matrix

Figure A.2: Run 3 systematics broken down into detector, flux, cross section and FSI matrices.
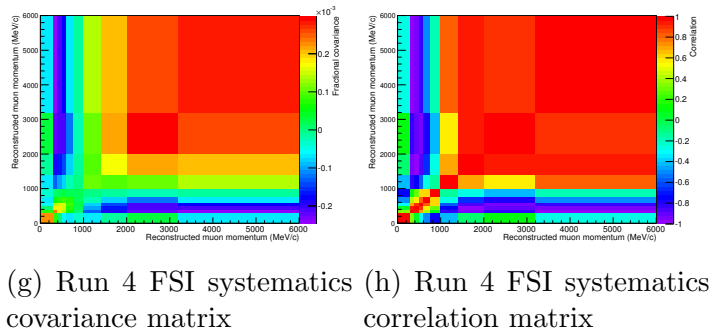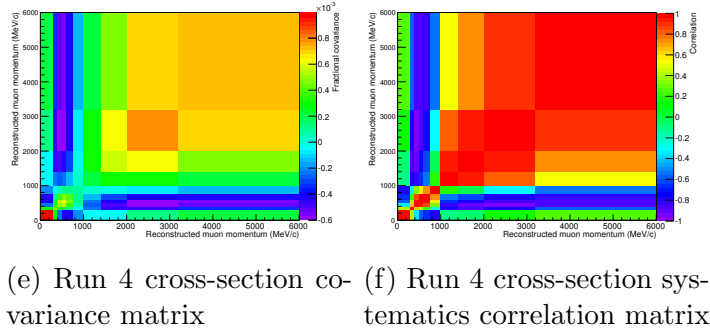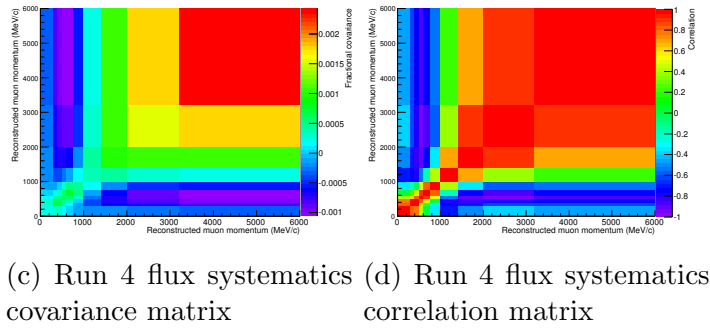
(a) Run 4 detector systematics covariance matrix

(b) Run 4 detector systematics correlation matrix

(c) Run 4 flux systematics covariance matrix

(d) Run 4 flux systematics correlation matrix

(e) Run 4 cross-section covariance matrix

(f) Run 4 cross-section systematics correlation matrix

(g) Run 4 FSI systematics covariance matrix

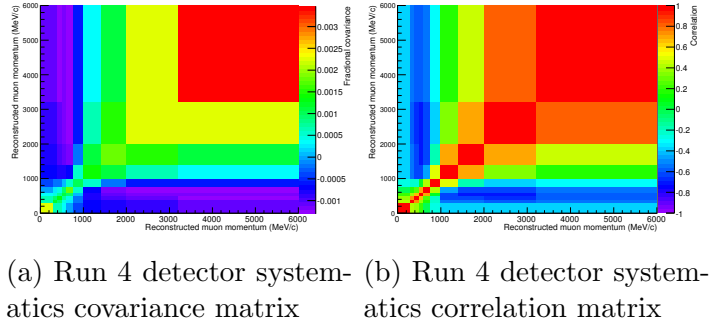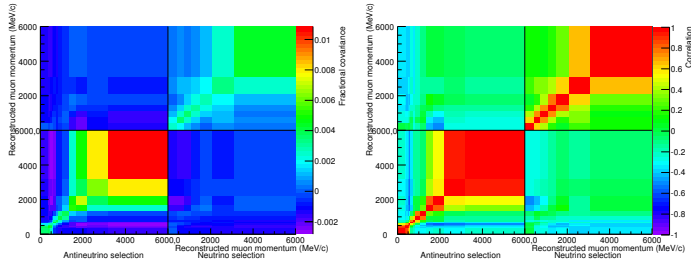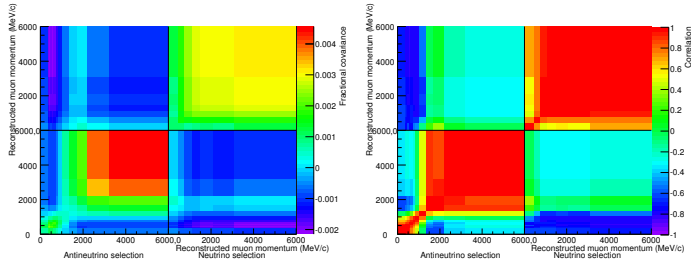(h) Run 4 FSI systematics correlation matrix

Figure A.3: Run 4 systematics broken down into detector, flux, cross section and FSI matrices.

(a) Run 5 detector systematics covariance matrix

(b) Run 5 detector systematics correlation matrix

(c) Run 5 flux systematics covariance matrix

(d) Run 5 flux systematics correlation matrix

(e) Run 5 cross-section covariance matrix

(f) Run 5 cross-section systematics correlation matrix

(g) Run 5 FSI systematics covariance matrix

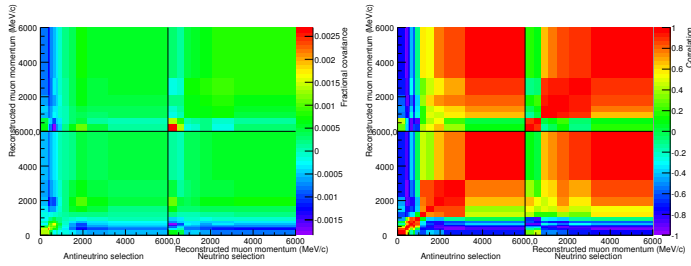(h) Run 5 FSI systematics correlation matrix

Figure A.4: Run 5 systematics broken down into detector, flux, cross section and FSI matrices.
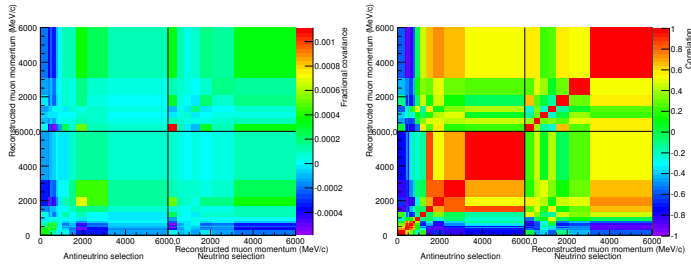
(a) Run 6 detector systematics covariance matrix

(b) Run 6 detector systematics correlation matrix

(c) Run 6 flux systematics covariance matrix
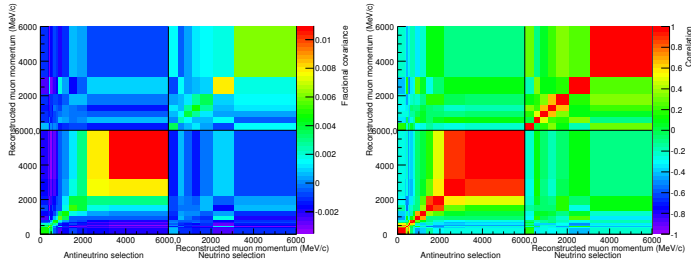
(d) Run 6 flux systematics correlation matrix

(e) Run 6 cross-section covariance matrix

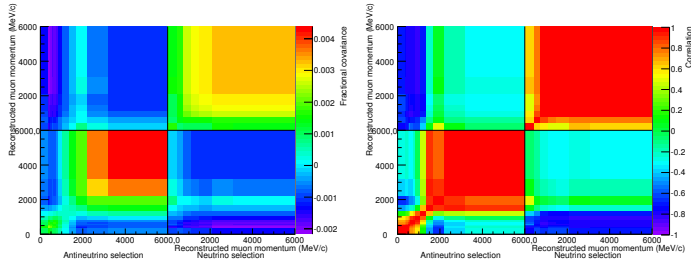(f) Run 6 cross-section systematics correlation matrix

(g) Run 6 FSI systematics covariance matrix

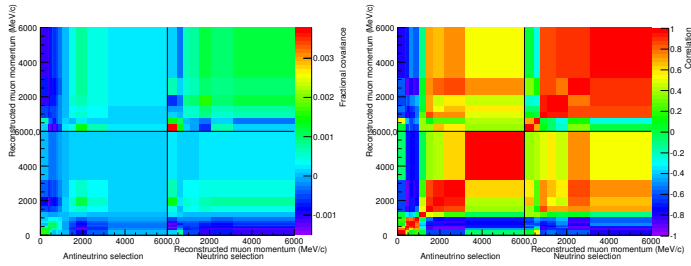(h) Run 6 FSI systematics correlation matrix

Figure A.5: Run 6 systematics broken down into detector, flux, cross section and FSI matrices.
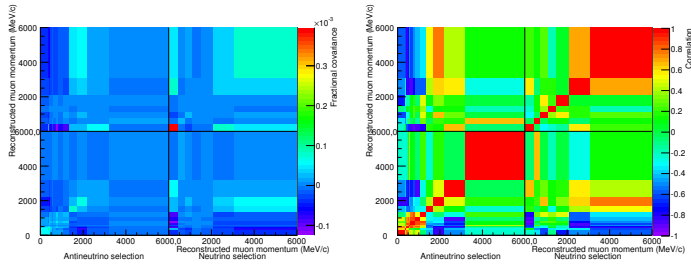
Appendix B

Toy data results

This appendix contains the results from the toy data studies used in the fitter validation and is described in section 6.1. The plots show the distribution of fitted values, the difference between fitted value and true value and the pull values for each set of initial scalings for each run. Gaussian fits were applied to each distribution to confirm that the shape appeared as expected.

Figure B.1: Run 2 toy data results from initial scalings given by toy set 1 from table 6.1.

Figure B.2: Run 2 toy data results from initial scalings given by toy set 2 from table 6.1.

Figure B.3: Run 2 toy data results from initial scalings given by toy set 3 from table 6.1.

Figure B.4: Run 2 toy data results from initial scalings given by toy set 4 from table 6.1.

Figure B.5: Run 3 toy data results from initial scalings given by toy set 1 from table 6.1.

Figure B.6: Run 3 toy data results from initial scalings given by toy set 2 from table 6.1.

Figure B.7: Run 3 toy data results from initial scalings given by toy set 3 from table 6.1.

Figure B.8: Run 3 toy data results from initial scalings given by toy set 4 from table 6.1.
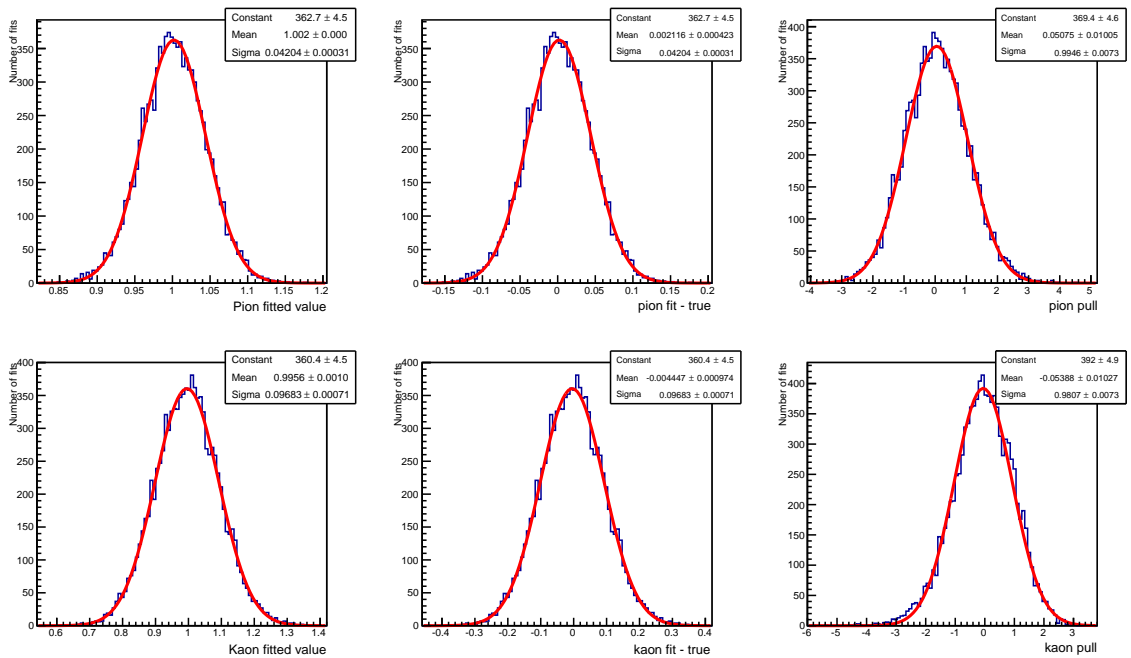

Figure B.9: Run 4 toy data results from initial scalings given by toy set 1 from table 6.1.

Figure B.10: Run 4 toy data results from initial scalings given by toy set 2 from table 6.1.

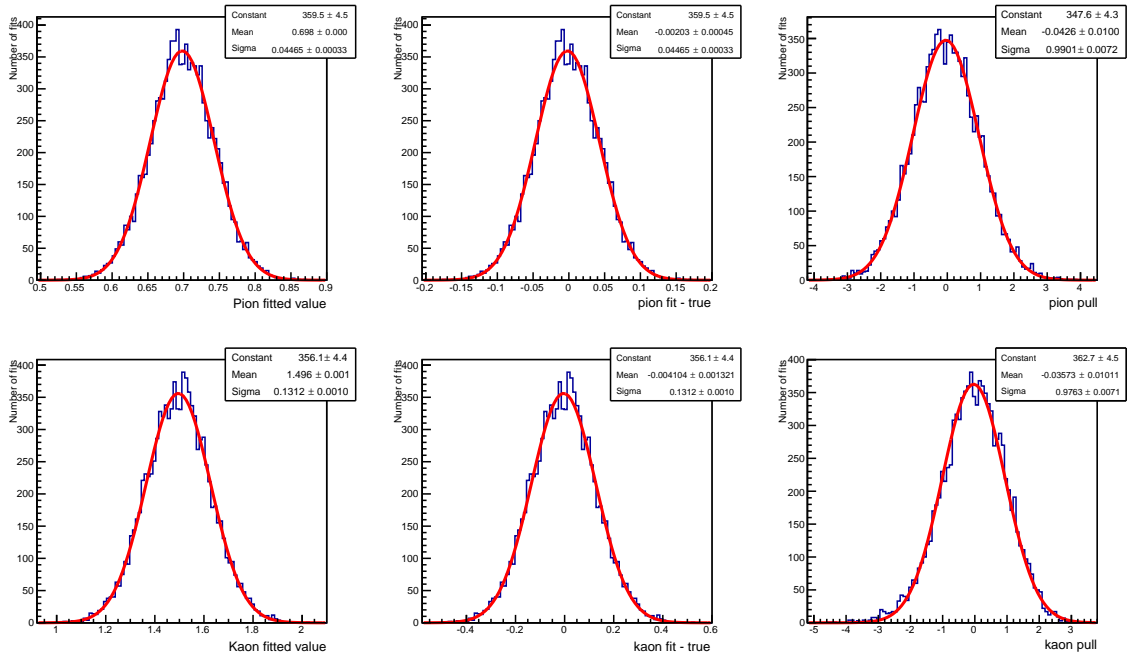Figure B.11: Run 4 toy data results from initial scalings given by toy set 3 from table 6.1.

Figure B.12: Run 4 toy data results from initial scalings given by toy set 4 from table 6.1.
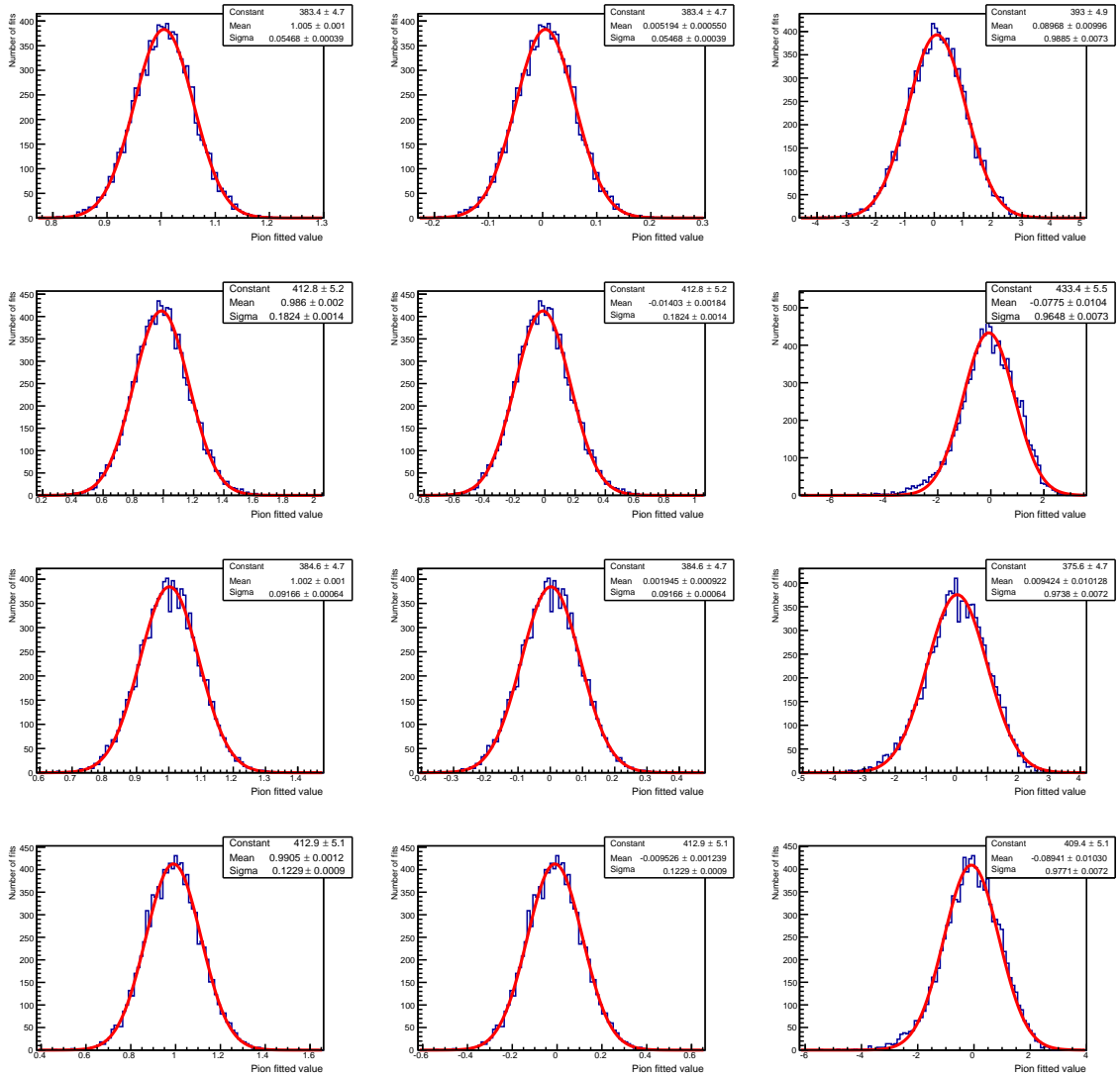
Figure B.13: Run 5 toy data results from initial scalings given by toy set 1 from table 6.2.
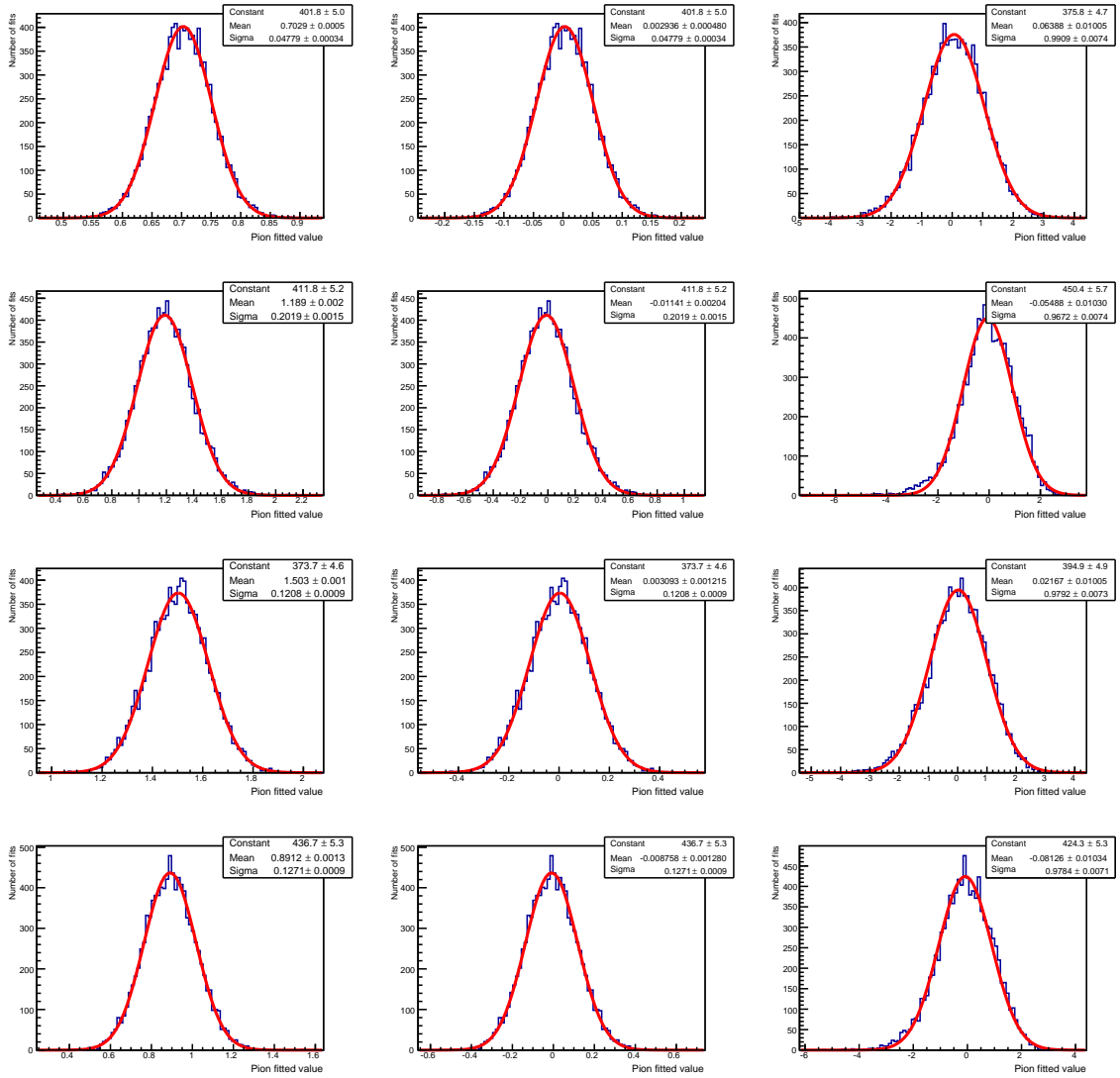
Figure B.14: Run 5 toy data results from initial scalings given by toy set 2 from table 6.2.
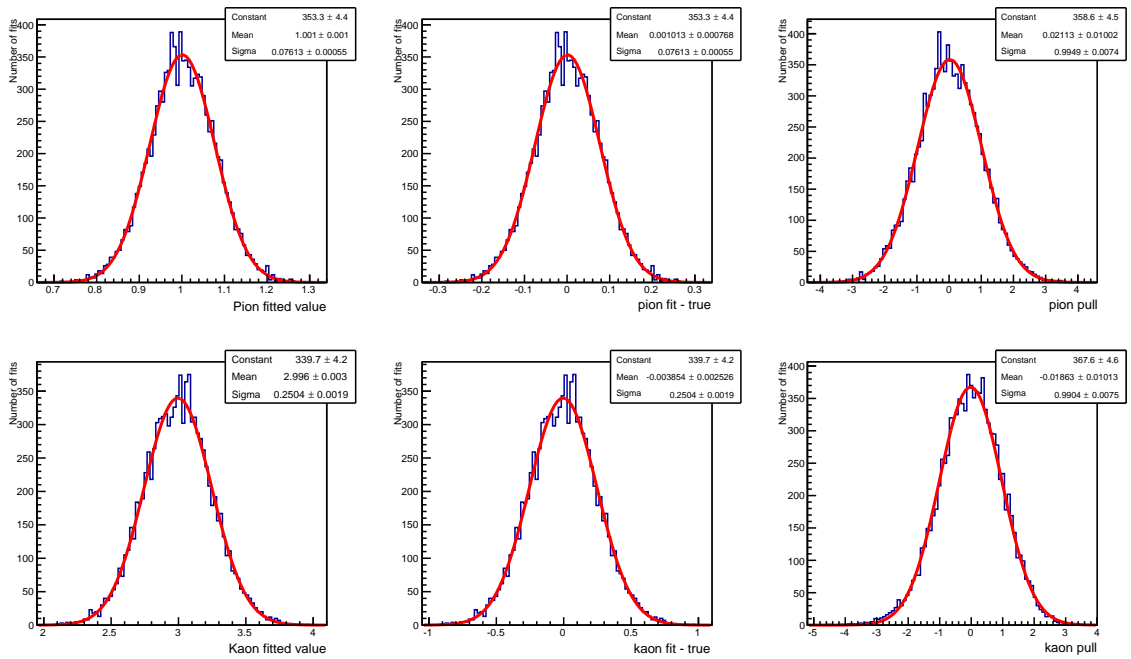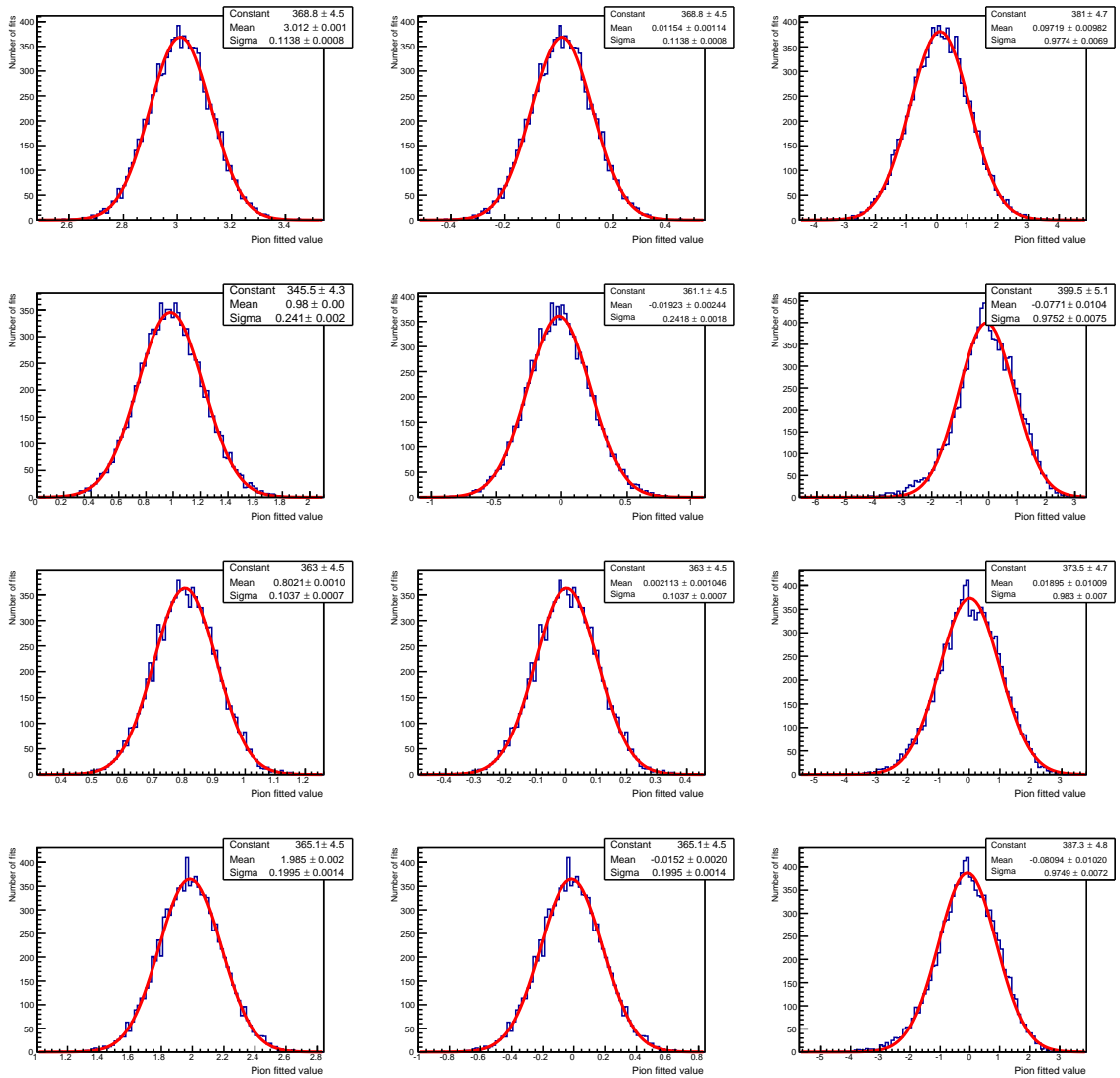
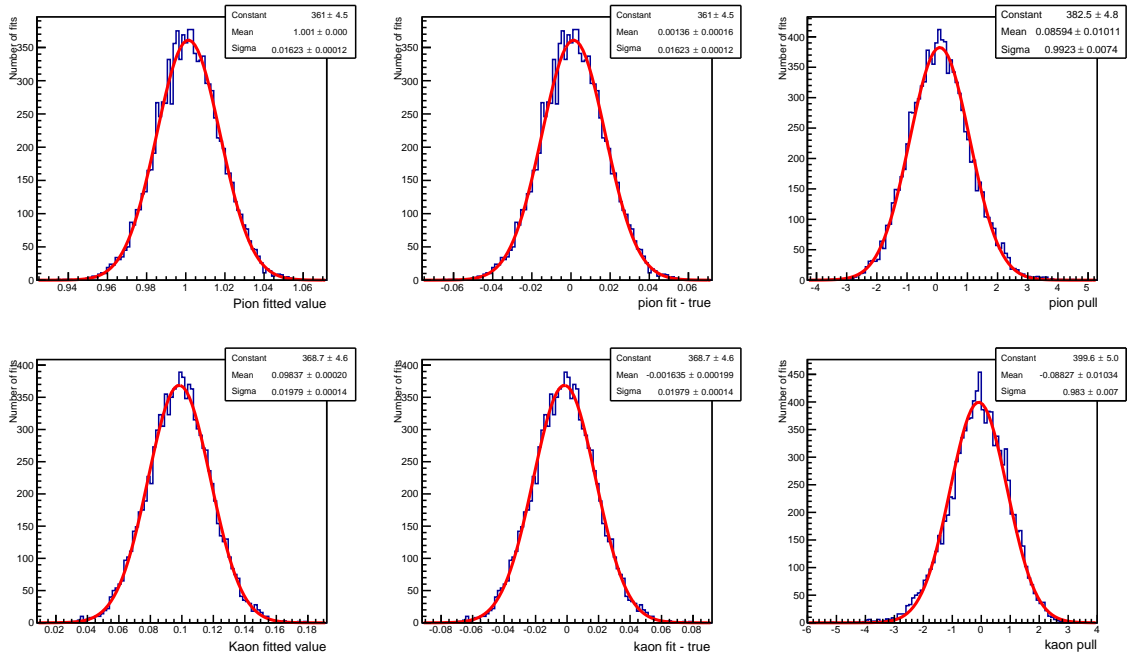Figure B.15: Run 5 toy data results from initial scalings given by toy set 3 from table 6.2.
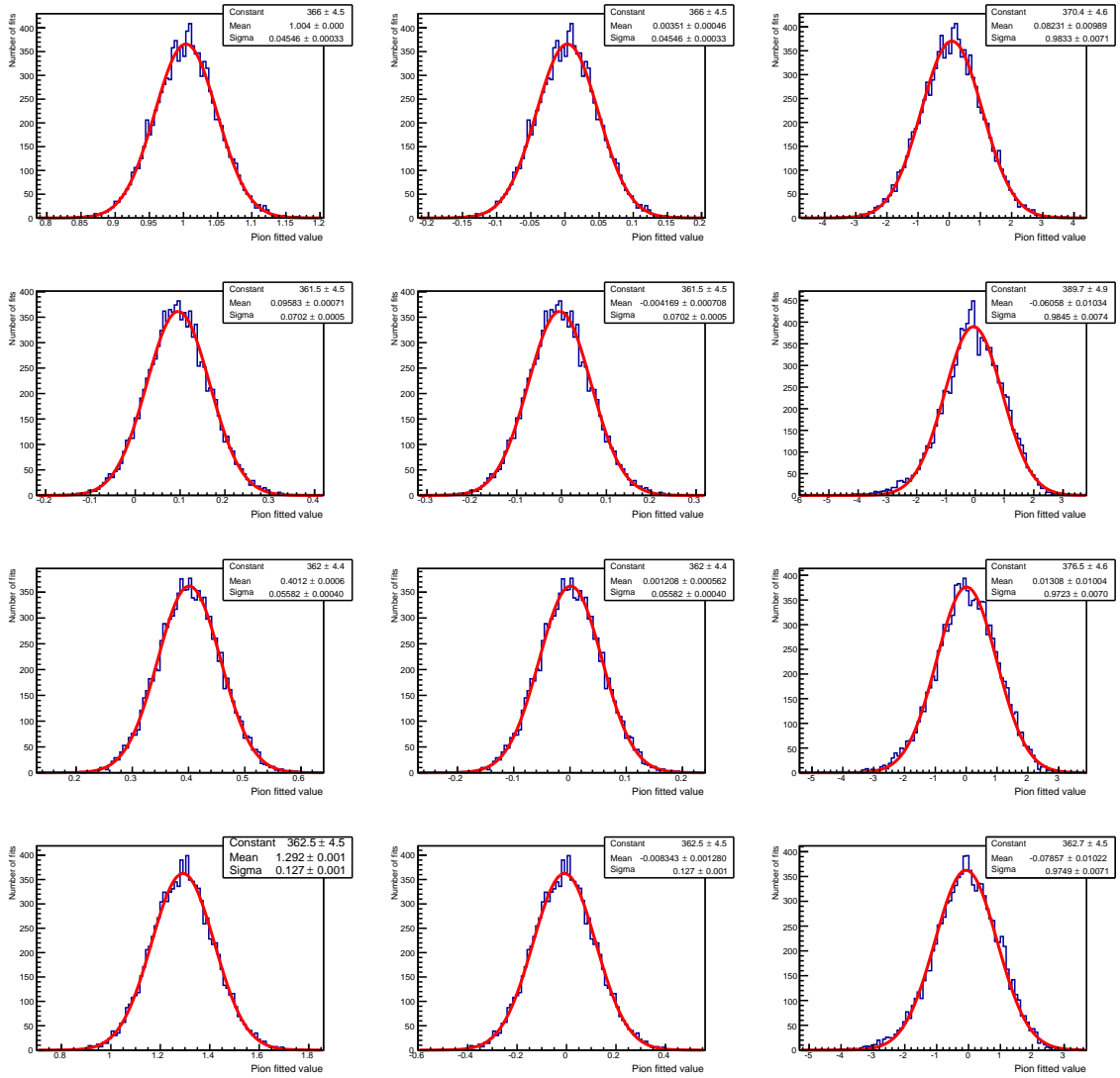
Figure B.16: Run 5 toy data results from initial scalings given by toy set 4 from table 6.2.
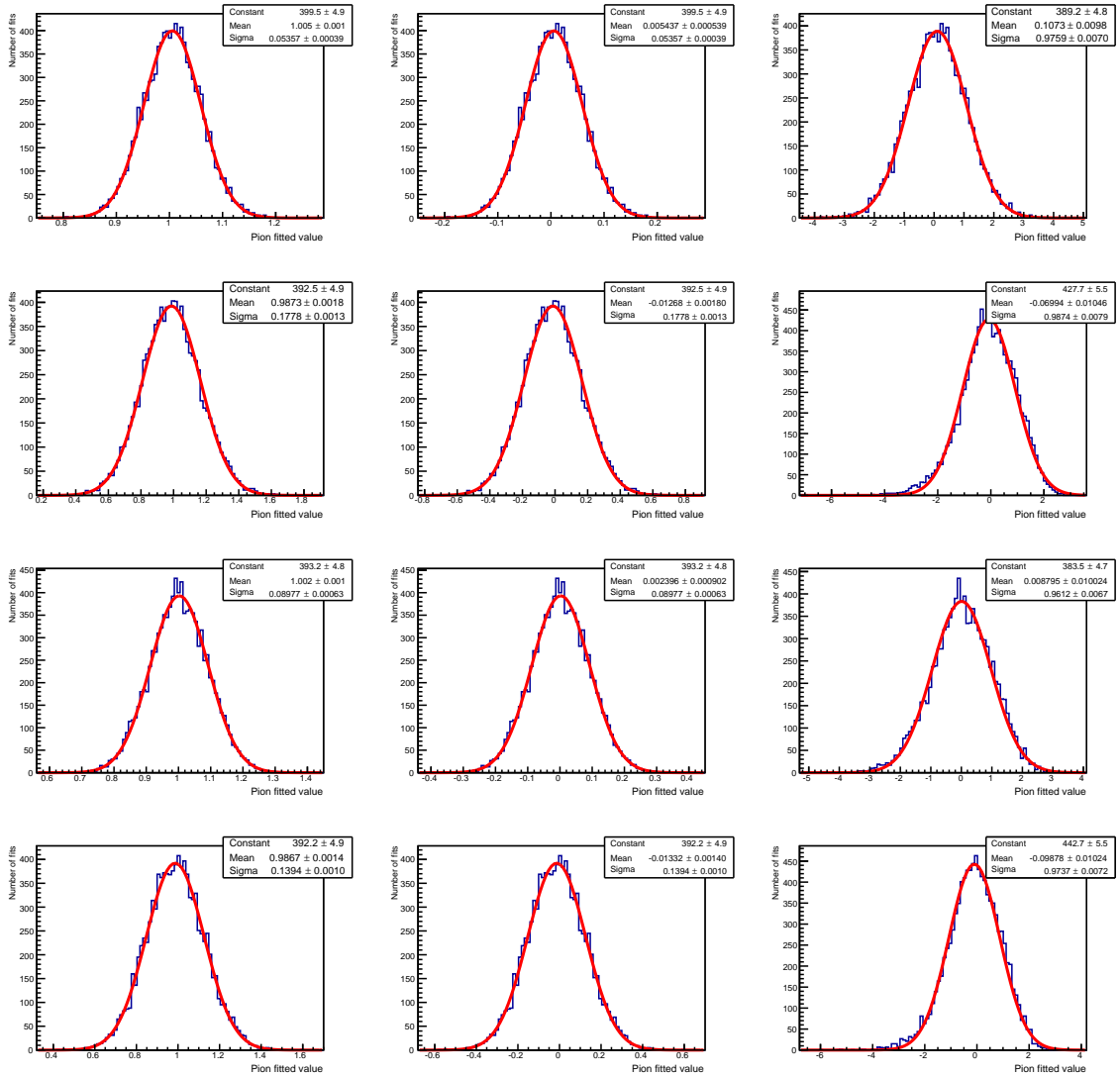
Figure B.17: Run 6 toy data results from initial scalings given by toy set 1 from table 6.2.
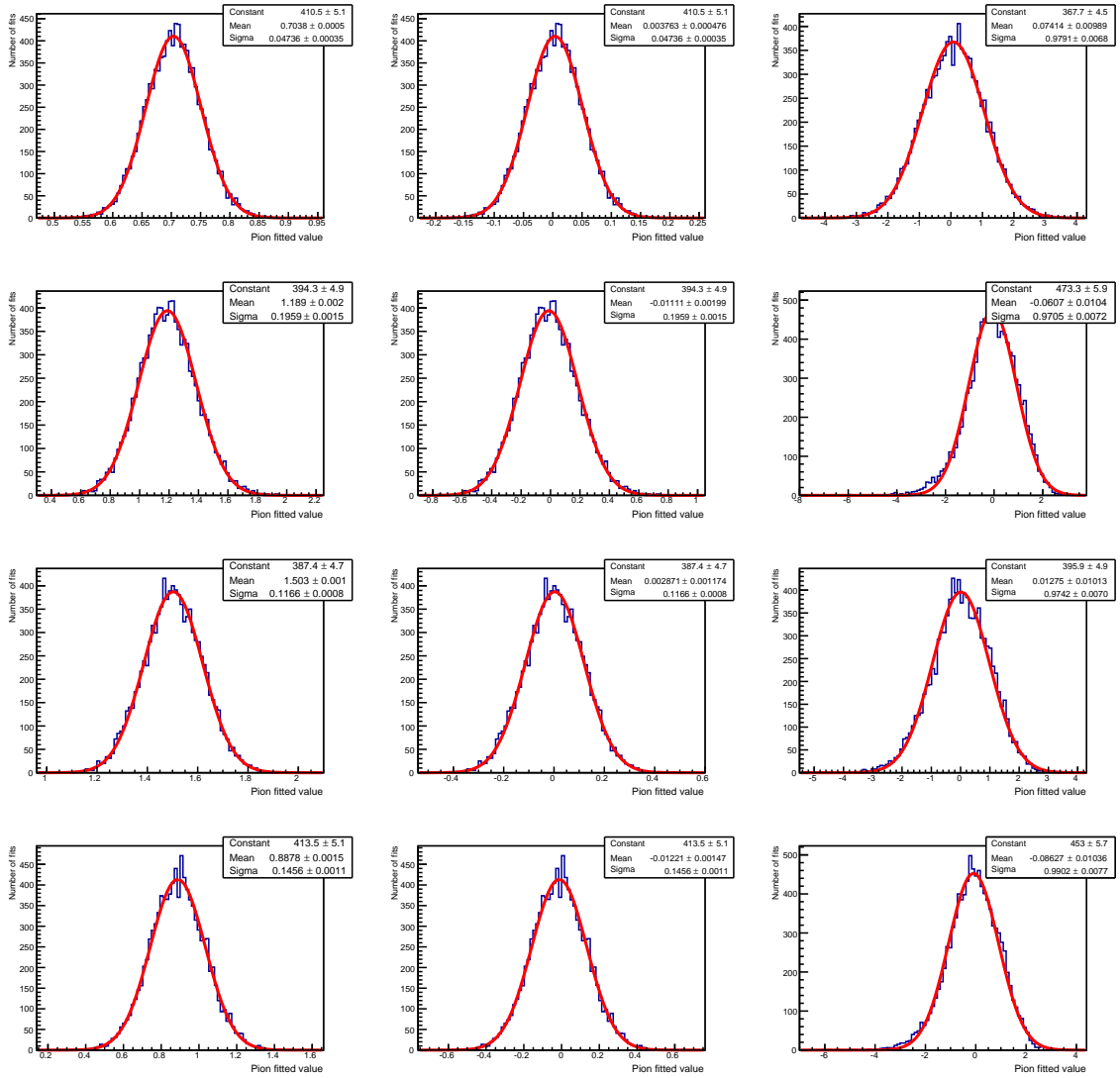
Figure B.18: Run 6 toy data results from initial scalings given by toy set 2 from table 6.2.
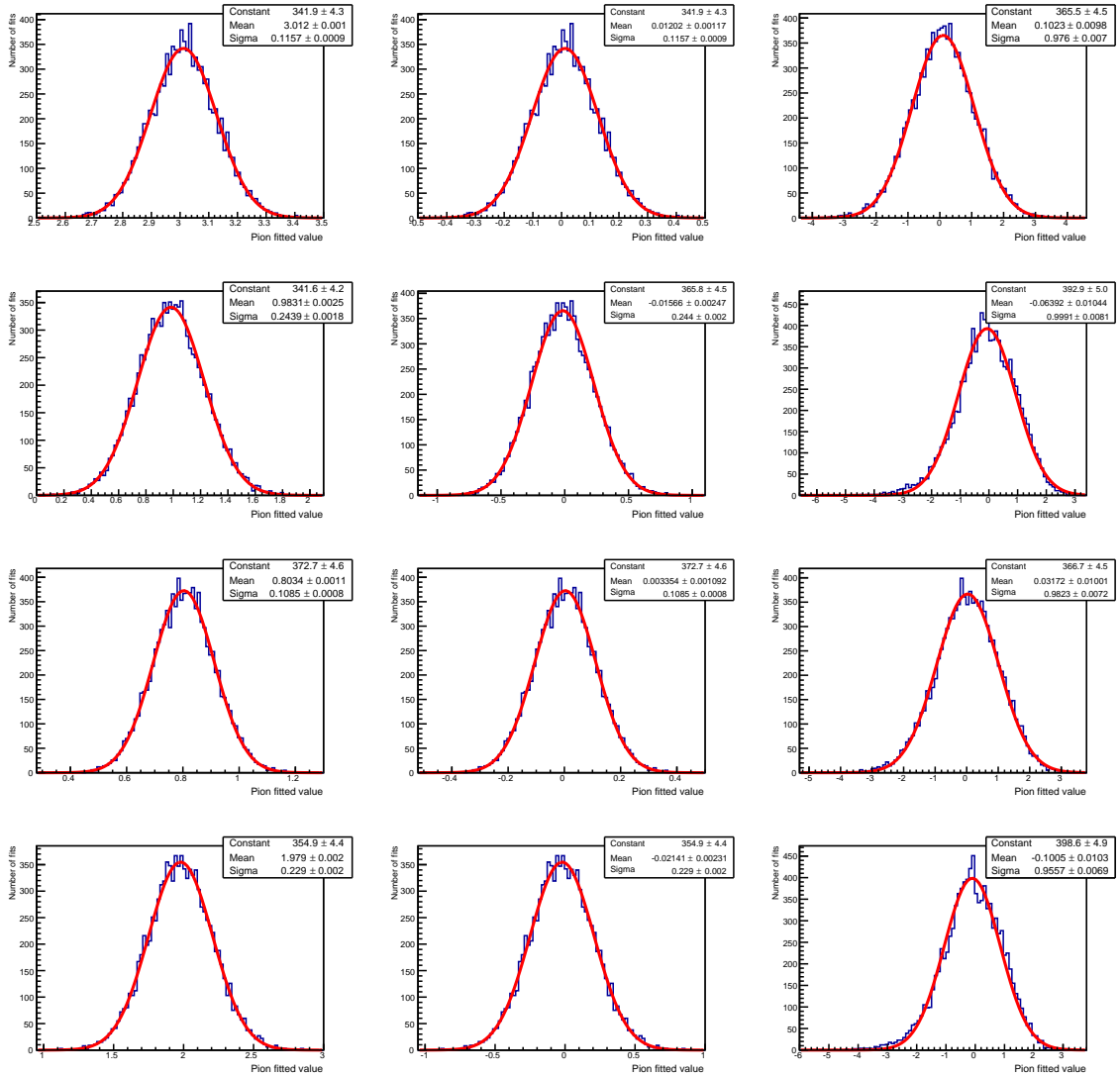
Figure B.19: Run 6 toy data results from initial scalings given by toy set 3 from table 6.2.

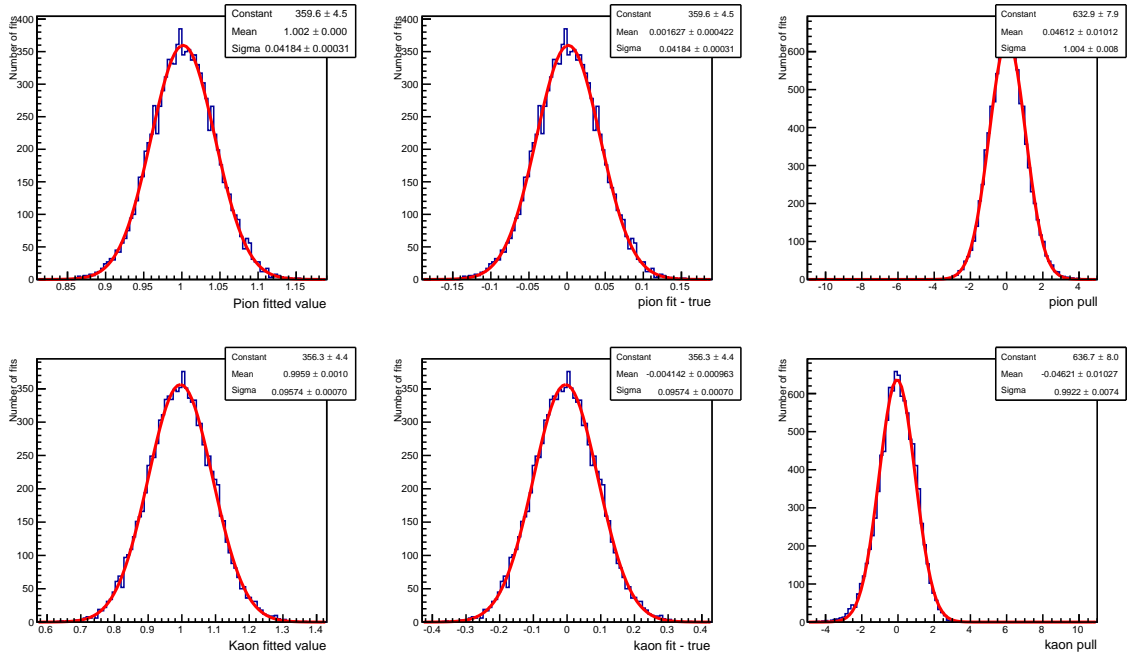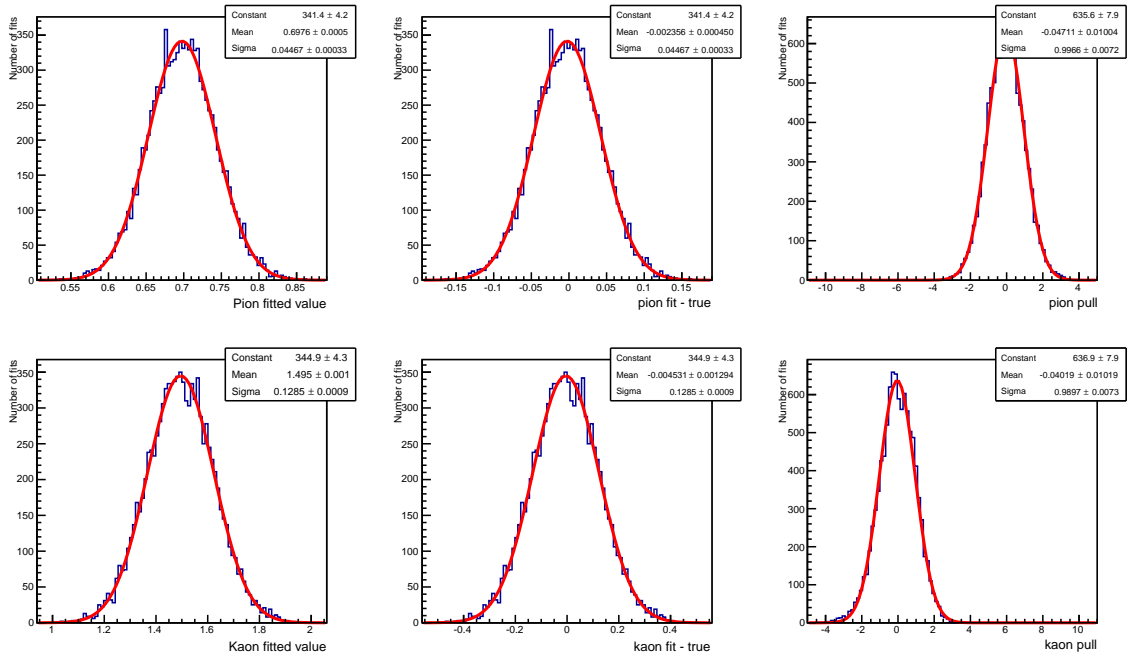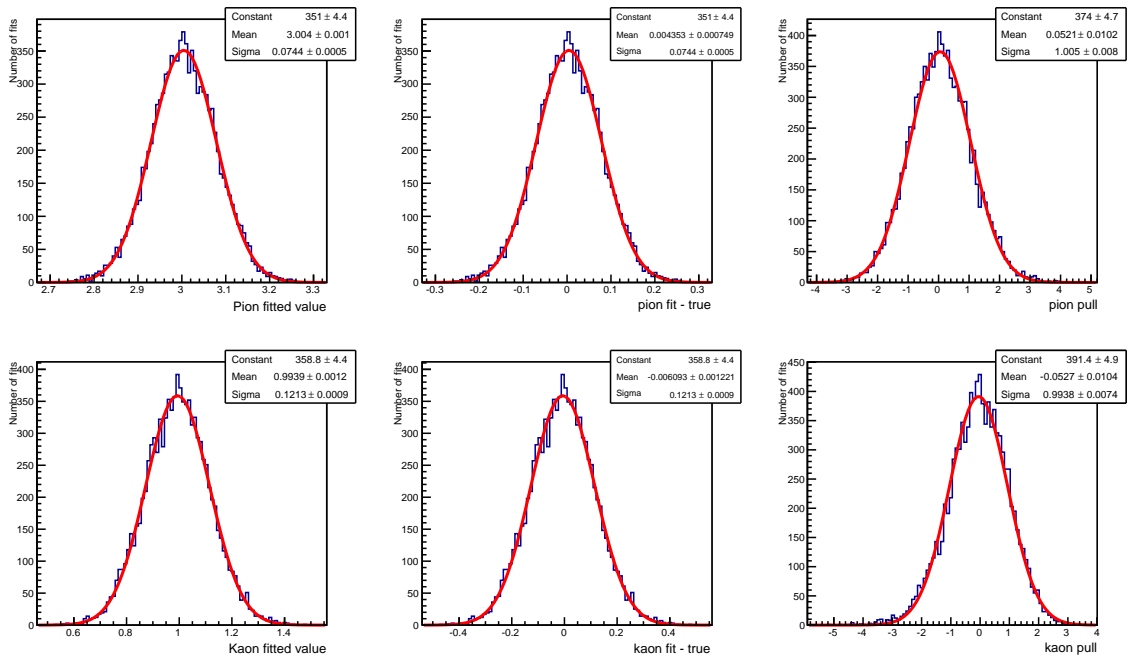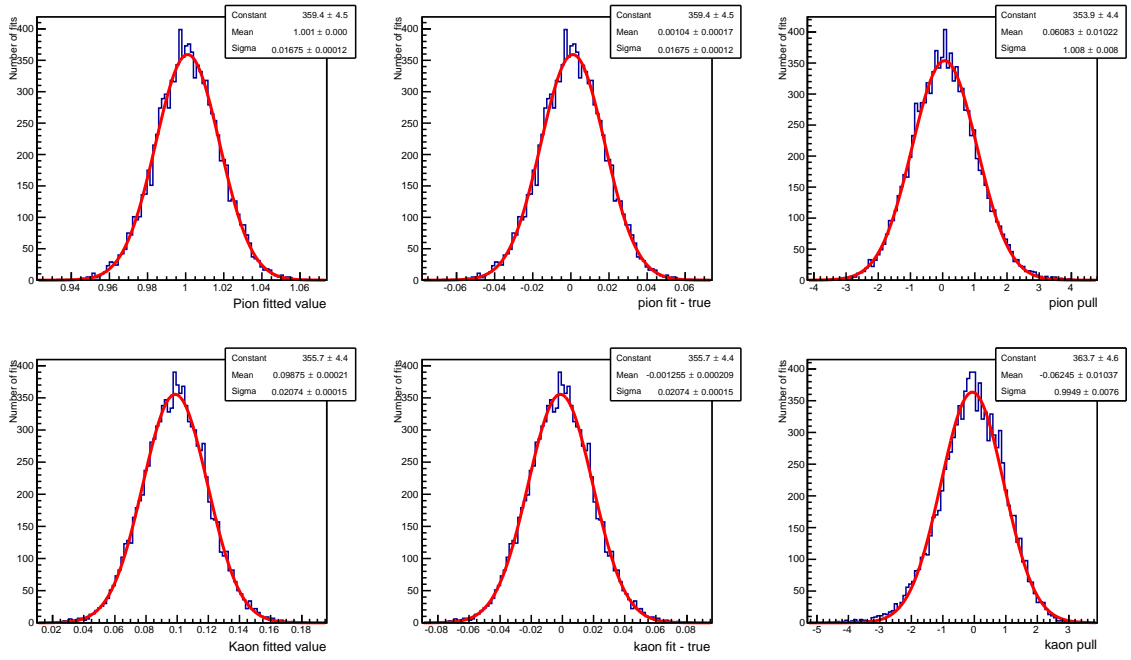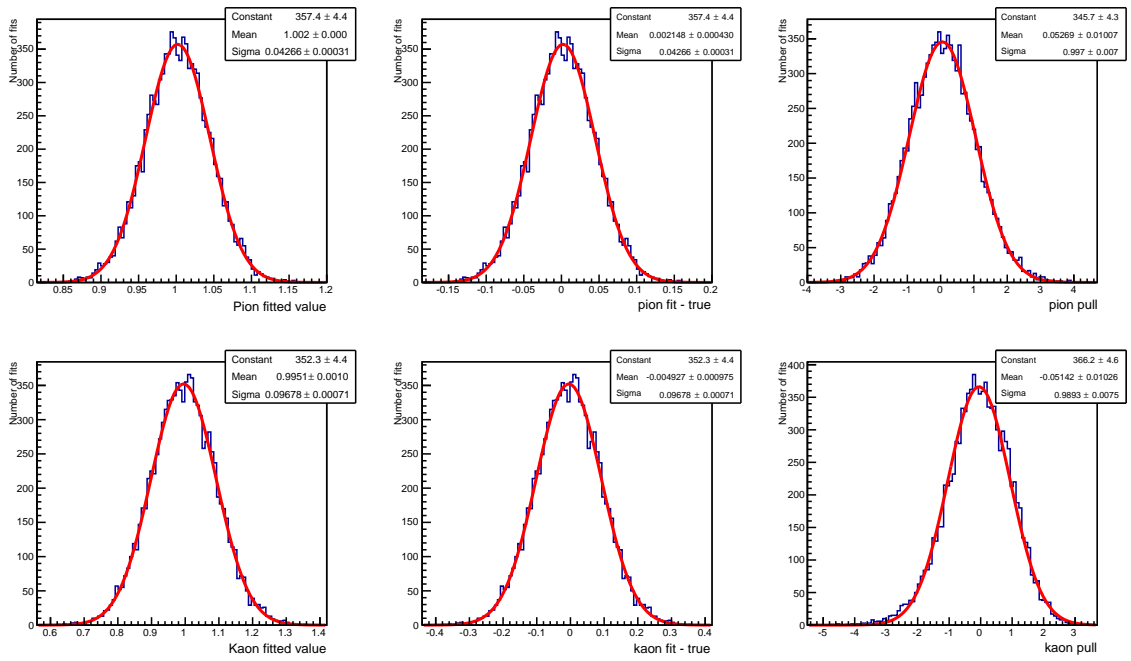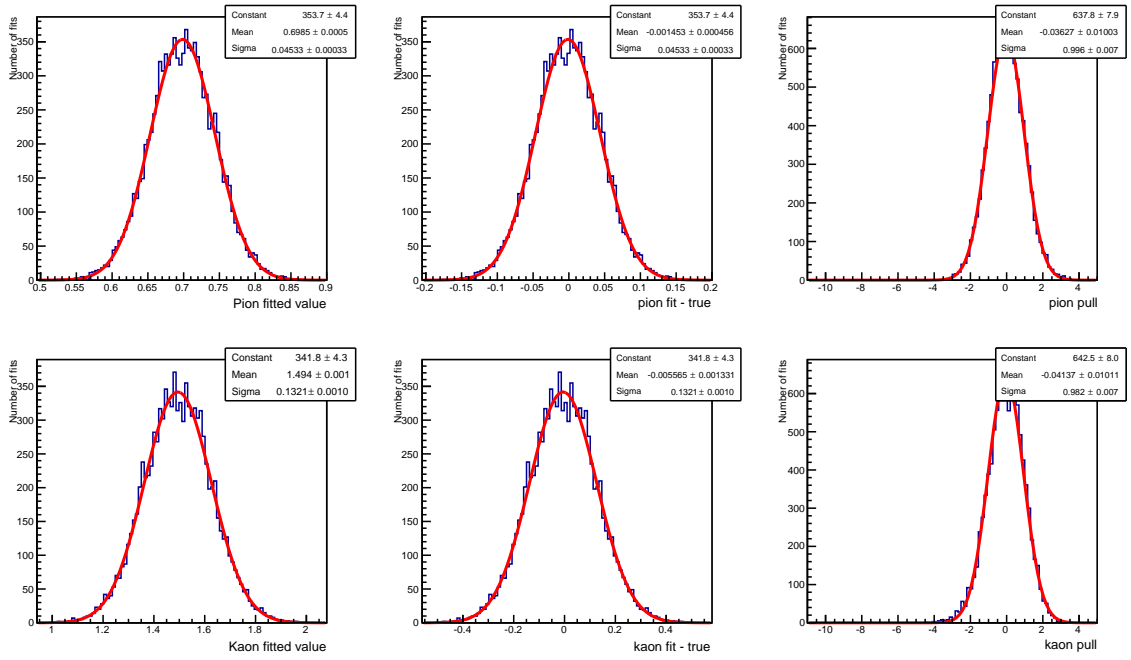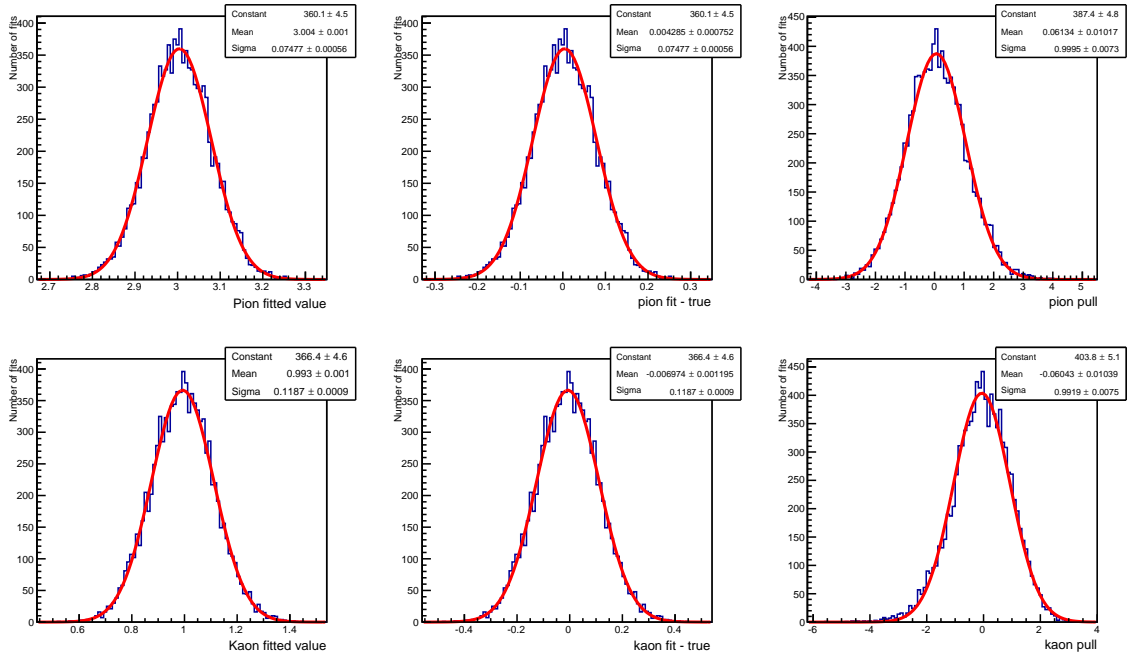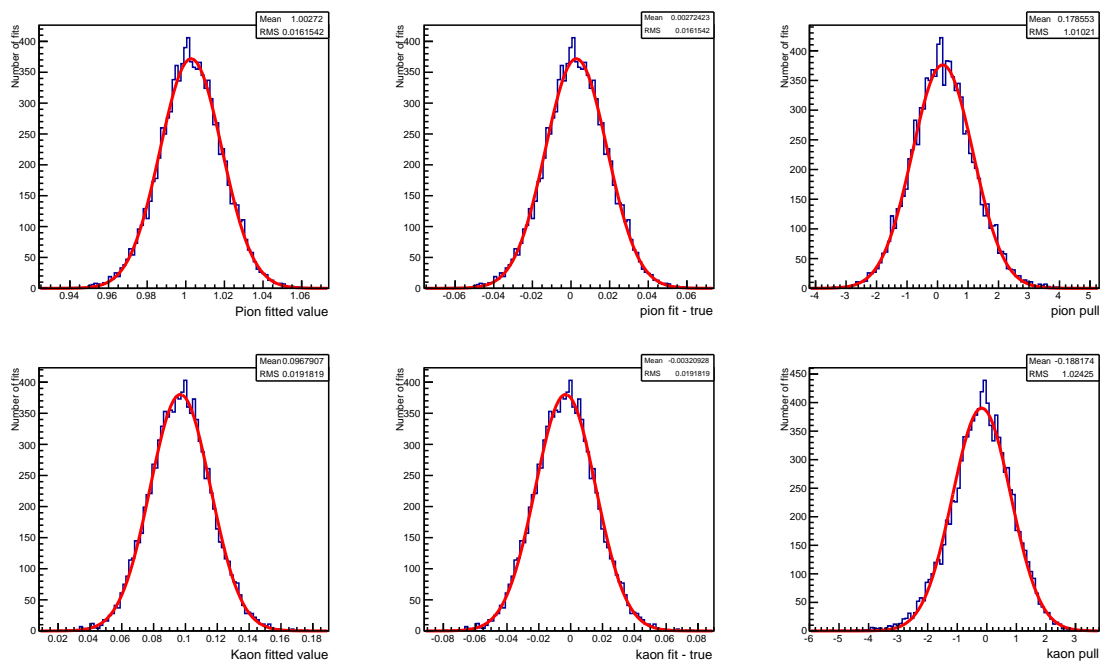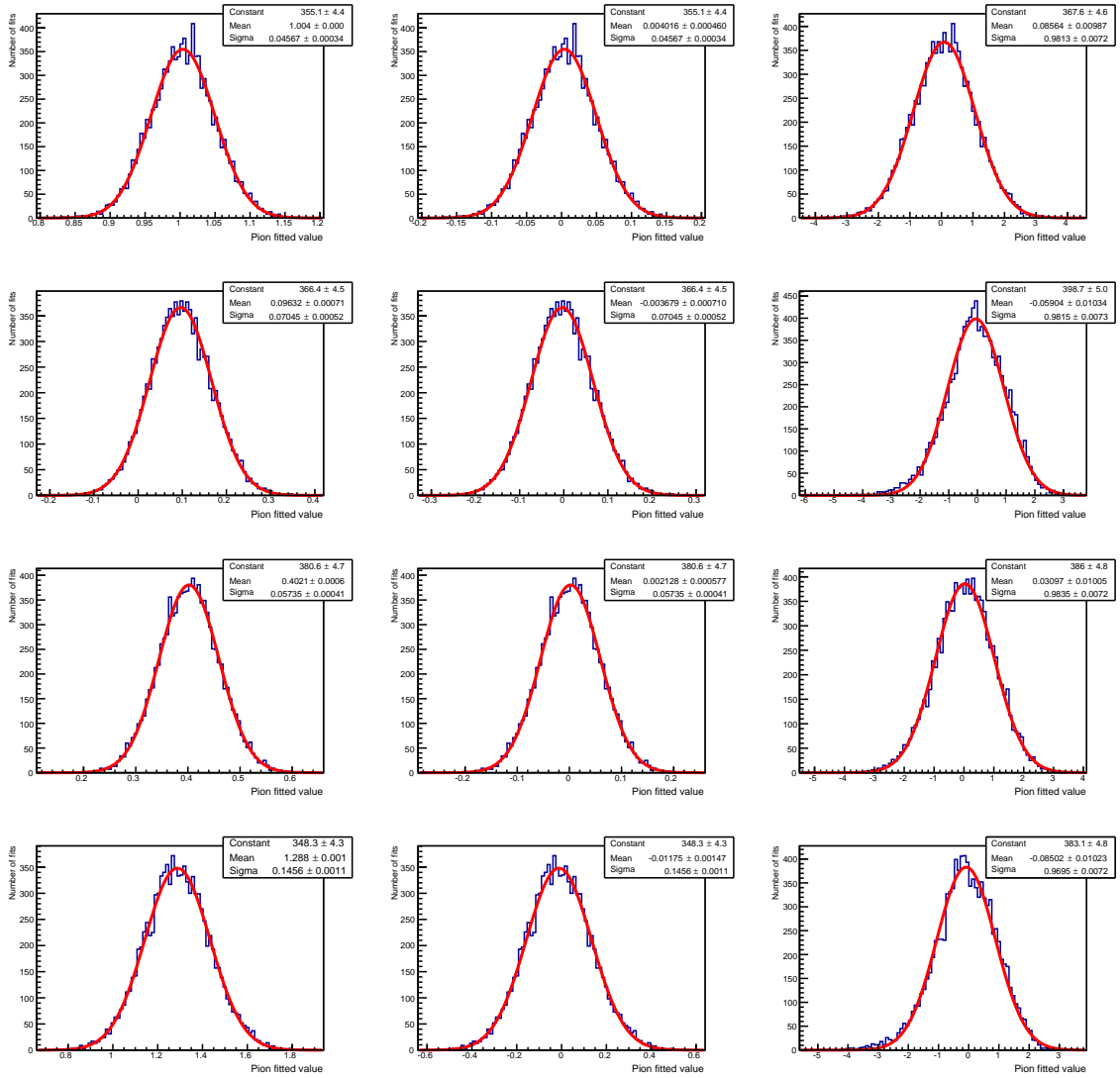Figure B.20: Run 6 toy data results from initial scalings given by toy set 4 from table 6.2.

Bibliography

[1] N. Abgrall et al. Measurements of cross sections and charged pion spectra in proton-carbon interactions at 31 GeV/c. *Phys. Rev. C*, 84:034604, Sep 2011.

[2] N. Abgrall et al. Measurement of production properties of positively charged kaons in proton-carbon interactions at 31 GeV/c. *Phys. Rev. C*, 85:035210, Mar 2012.

[3] W. Pauli. Dear radioactive ladies and gentlemen. *Phys. Today*, 31N9:27, 1978.

[4] F. Reines and C. L. Cowan. Detection of the free neutrino. *Phys. Rev.*, 92:830–831, Nov 1953.

[5] G. Danby, J-M. Gaillard, K. Goulianos, L. M. Lederman, N. Mistry, M. Schwartz, and J. Steinberger. Observation of high-energy neutrino reactions and the existence of two kinds of neutrinos. *Phys. Rev. Lett.*, 9:36–44, Jul 1962.

[6] K. Kodama et al. Observation of tau neutrino interactions. *Physics Letters B*, 504(3):218 – 224, 2001.

[7] The ALEPH Collaboration, The DELPHI Collaboration, The L3 Collaboration, The OPAL Collaboration, The SLD Collaboration, The LEP Electroweak Working Group, The SLD Electroweak, and Heavy Flavour Groups. Precision electroweak measurements on the z resonance. *Physics Reports*, 427(5–6):257 – 454, 2006.

[8] Bruce T. Cleveland, Timothy Daily, Jr. Raymond Davis, James R. Distel, Kenneth Lande, C. K. Lee, Paul S. Wildenhain, and Jack Ullman. Measurement

of the solar electron neutrino flux with the homestake chlorine detector. *The Astrophysical Journal*, 496(1):505, 1998.

[9] J. N. Abdurashitov et al. Solar neutrino flux measurements by the soviet-american gallium experiment (sage) for half the 22-year solar cycle. *Journal of Experimental and Theoretical Physics*, 95(2):181–193, Aug 2002.

[10] M. Cribier et al. Results of the whole gallex experiment. *Nuclear Physics B - Proceedings Supplements*, 70(1):284 – 291, 1999. Proceedings of the Fifth International Workshop on topics in Astroparticle and Underground Physics.

[11] Y. Fukuda et al. Measurements of the solar neutrino flux from super-kamiokande's first 300 days. *Phys. Rev. Lett.*, 81:1158–1162, Aug 1998.

[12] Y. Fukuda et al. Evidence for oscillation of atmospheric neutrinos. *Phys. Rev. Lett.*, 81:1562–1567, Aug 1998.

[13] Gulsheen Ahuja, Manmohan Gupta, and Monika Randhawa. Constructing the CKM and PMNS matrices from mixing data. 2006.

[14] The Daya Bay Collaboration. Observation of electron-antineutrino disappearance at daya bay. 108:171803, Apr 2012.

[15] Patrick Pfahler and the Double Chooz Collaboration. The double chooz experiment. *Journal of Physics: Conference Series*, 375(4):042064, 2012.

[16] T. Araki et al. Measurement of neutrino oscillation with KamLAND: Evidence of spectral distortion. *Phys. Rev. Lett.*, 94:081801, 2005.

[17] K. J. Ahnet al. RENO: An Experiment for Neutrino Oscillation Parameter θ_{13} Using Reactor Neutrinos at Yonggwang. 2010.

[18] The T2K Collaboration. The t2k experiment. *Nuclear Instruments and Methods in Physics Research Section A: Accelerators, Spectrometers, Detectors and Associated Equipment*, 659(1):106 – 135, 2011.

[19] Jianming Bian. The NOvA Experiment: Overview and Status. In *Meeting of the APS Division of Particles and Fields (DPF 2013) Santa Cruz, California, USA, August 13-17, 2013*, 2013.

[20] Alexandre B. Sousa. First MINOS+ Data and New Results from MINOS. *AIP Conf. Proc.*, 1666:110004, 2015.

[21] Ivan Esteban, M. C. Gonzalez-Garcia, Michele Maltoni, Ivan Martinez-Soler, and Thomas Schwetz. Updated fit to three neutrino mixing: exploring the accelerator-reactor complementarity. *JHEP*, 01:087, 2017.

[22] The SNO Collaboration. Direct evidence for neutrino flavor transformation from neutral-current interactions in the sudbury neutrino observatory. 89:011301, Jun 2002.

[23] M.P. Decowski. Kamland's precision neutrino oscillation measurements. *Nuclear Physics B*, 908:52 – 61, 2016. Neutrino Oscillations: Celebrating the Nobel Prize in Physics 2015.

[24] Y. Fukuda et al. The Super-Kamiokande detector. *Nucl. Instrum. Meth.*, A501:418–462, 2003.

[25] M. Merck. The icecube detector: A large sensor network at the south pole. *IEEE Pervasive Computing*, 9(4):43–47, October 2010.

[26] The T2K Collaboration. Measurement of neutrino and antineutrino oscillations by the t2k experiment including a new additional sample of ν_e interactions at the far detector.

[27] The T2K Collaboration. Evidence of electron neutrino appearance in a muon neutrino beam. *Phys. Rev. D*, 88:032002, Aug 2013.

[28] Morgan Wascko. T2k status, results, and plans, June 2018.

[29] J. A. Formaggio and G. P. Zeller. From ev to eev: Neutrino cross sections across energy scales. *Rev. Mod. Phys.*, 84:1307–1341, Sep 2012.

[30] R.A. Smith and E.J. Moniz. Neutrino reactions on nuclear targets. *Nuclear Physics B*, 43:605 – 622, 1972.

[31] H. De Vries, C.W. De Jager, and C. De Vries. Nuclear charge-density-distribution parameters from elastic electron scattering. *Atom. Data Nucl. Data Tabl.*, 36:495536, 1987.

[32] P K A de Witt Huberts. Proton spectral functions and momentum distributions in nuclei from high-resolution (e,e'p) experiments. *Journal of Physics G: Nuclear and Particle Physics*, 16(4):507, 1990.

[33] D. Rohe et al. Correlated strength in the nuclear spectral function. *Phys. Rev. Lett.*, 93:182501, Oct 2004.

[34] Omar Benhar and Adelchi Fabrocini. Two-nucleon spectral function in infinite nuclear matter. *Phys. Rev. C*, 62:034304, Aug 2000.

[35] M. Martini, M. Ericson, G. Chanfray, and J. Marteau. Unified approach for nucleon knock-out and coherent and incoherent pion production in neutrino interactions with nuclei. *Phys. Rev. C*, 80:065501, Dec 2009.

[36] J. Nieves, I. Ruiz Simo, and M. J. Vicente Vacas. Inclusive charged-current neutrino-nucleus reactions. *Phys. Rev. C*, 83:045501, Apr 2011.

[37] Tomasz Golan. Modeling nuclear effects in nuwro monte carlo neutrino event generator. http://neutrino.ift.uni.wroc.pl/files/phd_tomasz_golan.pdf, 2014.

[38] Patrick de Perio. Neut pion fsi. *AIP Conference Proceedings*, 1405(1):223–228, 2011.

[39] S. Boyd, S. Dytman, E. Hernández, J. Sobczyk, and R. Tacik. Comparison of models of neutrinonucleus interactions. *AIP Conference Proceedings*, 1189(1):60–73, 2009.

[40] Steven Dytman. Neutrino event generators. *AIP Conference Proceedings*, 896(1):178–184, 2007.

[41] Julien Lesgourgues and Sergio Pastor. Neutrino cosmology and Planck. *New J. Phys.*, 16:065002, 2014.

[42] J. D. Vergados, H. Ejiri, and F. Šimkovic. Neutrinoless double beta decay and neutrino mass. *Int. J. Mod. Phys.*, E25(11):1630007, 2016.

[43] B. Bornschein. Determination of neutrino mass from tritium beta decay. *Fusion Science and Technology*, 54(1):59–66, 2008.

[44] Francesco Capozzi, Eleonora Di Valentino, Eligio Lisi, Antonio Marrone, Alessandro Melchiorri, and Antonio Palazzo. Global constraints on absolute neutrino masses and their ordering. *Phys. Rev.*, D95(9):096014, 2017.

[45] N. R. Cahn et al. White Paper: Measuring the Neutrino Mass Hierarchy. In *Proceedings, 2013 Community Summer Study on the Future of U.S. Particle Physics: Snowmass on the Mississippi (CSS2013): Minneapolis, MN, USA, July 29-August 6, 2013*, 2013.

[46] Mark G. Inghram and John H. Reynolds. Double beta-decay of te^{130}. *Phys. Rev.*, 78:822–823, Jun 1950.

[47] Oliviero Cremonesi. Neutrinoless double beta decay: Present and future. *Nucl. Phys. Proc. Suppl.*, 118:287–296, 2003. [,287(2002)].

[48] A. Aguilar-Arevalo et al. Evidence for neutrino oscillations from the observation of anti-neutrino(electron) appearance in a anti-neutrino(muon) beam. *Phys. Rev.*, D64:112007, 2001.

[49] A. A. Aguilar-Arevalo et al. Improved search for $\overline{\nu}_\mu \rightarrow \overline{\nu}_e$ oscillations in the miniboone experiment. *Phys. Rev. Lett.*, 110:161801, Apr 2013.

[50] B. Armbruster et al. Upper limits for neutrino oscillations $\overline{\nu}_\mu \rightarrow \overline{\nu}_e$ from muon decay at rest. *Phys. Rev. D*, 65:112001, Jun 2002.

[51] P. Astier et al. Search for nu(mu) —¿ nu(e) oscillations in the NOMAD experiment. *Phys. Lett.*, B570:19–31, 2003.

[52] M. Antonello et al. Search for anomalies in the ν_e appearance from a ν_μ beam. *The European Physical Journal C*, 73(10):2599, Oct 2013.

[53] A. A. Aguilar-Arevalo et al. Observation of a Significant Excess of Electron-Like Events in the MiniBooNE Short-Baseline Neutrino Experiment. 2018.

[54] P. Adamson et al. Search for sterile neutrinos in MINOS and MINOS+ using a two-detector fit. *Submitted to: Phys. Rev. Lett.*, 2017.

[55] R. Acciarri et al. Design and Construction of the MicroBooNE Detector. *JINST*, 12(02):P02017, 2017.

[56] J. M. Conrad and M. H. Shaevitz. Sterile Neutrinos: An Introduction to Experiments. 2016.

[57] J. M. Conrad and M. H. Shaevitz. Sterile Neutrinos: An Introduction to Experiments. *Adv. Ser. Direct. High Energy Phys.*, 28:391–442, 2018.

[58] The T2K Collaboration. Official documents. http://www.t2k.org/docs/photos/general/.

[59] A. Hasler. *T2K Replica Target Hadron Production Measurements in NA61/SHINE and T2K Neutrino Flux Predictions*. PhD thesis, Geneva U., 2015.

[60] The T2K Collaboration. Nd280 flux uncertainties. https://www.t2k.org/docs/plots/045/flux-plots.

[61] PDG. http://pdg.lbl.gov/2018/listings/contents$_l$istings.html.

[62] Yoshio Saito. Materials and processing of vacuum components for the high-intensity proton beam accelerator, j-parc. *Vacuum*, 73(2):181 – 186, 2004. Proceedings of the European Vacuum Congress Berlin 2003, 23-26 June 2003, featuring the 8th European Vacuum Conference, 2nd Annual Conference of the German Vacuum Society.

[63] S. Bhadra et al. Optical transition radiation monitor for the t2k experiment. *Nuclear Instruments and Methods in Physics Research Section A: Accelerators, Spectrometers, Detectors and Associated Equipment*, 703:45 – 58, 2013.

[64] The T2K Collaboration. T2k neutrino flux prediction. *Phys. Rev. D*, 87:012001, Jan 2013.

[65] The T2K Collaboration. Flux plots. https://t2k.org/docs/plots/045/flux-plots.

[66] K. Abe et al. Measurements of the t2k neutrino beam properties using the ingrid on-axis near detector. *Nuclear Instruments and Methods in Physics Research Section A: Accelerators, Spectrometers, Detectors and Associated Equipment*, 694:211 – 223, 2012.

[67] T2K Technical 160. Measurement of the flux averaged inclusive numu charged current cross section with ingrid and proton module.

[68] S. Assylbekov et al. The T2K ND280 Off-Axis Pi-Zero Detector. *Nucl. Instrum. Meth.*, A686:48–63, 2012.

[69] K. Abe et al. Measurement of the electron neutrino charged-current interaction rate on water with the t2k nd280 π^0 detector. *Phys. Rev. D*, 91:112010, Jun 2015.

[70] N. Abgrall et al. Time projection chambers for the t2k near detectors. *Nuclear Instruments and Methods in Physics Research Section A: Accelerators, Spectrometers, Detectors and Associated Equipment*, 637(1):25 – 46, 2011.

[71] P.-A. Amaudruz et al. The t2k fine-grained detectors. *Nuclear Instruments and Methods in Physics Research Section A: Accelerators, Spectrometers, Detectors and Associated Equipment*, 696:1 – 31, 2012.

[72] K. Abe et al. First measurement of the ν_μ charged-current cross section on a water target without pions in the final state. *Phys. Rev. D*, 97:012001, Jan 2018.

[73] K. Abe et al. First measurement of the muon neutrino charged current single pion production cross section on water with the T2K near detector. *Phys. Rev.*, D95(1):012010, 2017.

[74] The T2K Collaboration. The electromagnetic calorimeter for the t2k near detector nd280. *Journal of Instrumentation*, 8(10):P10019, 2013.

[75] S. Aoki et al. The T2K Side Muon Range Detector (SMRD). *Nucl. Instrum. Meth.*, A698:135–146, 2013.

[76] Y. Ashie et al. Measurement of atmospheric neutrino oscillation parameters by super-kamiokande i. *Phys. Rev. D*, 71:112005, Jun 2005.

[77] The SuperKamiokande Collaboration. Images of super-kamiokande events. http://www.ps.uci.edu/ tomba/sk/tscan/pictures.html.

[78] Sarah J Ives. Study of the kaon contribution to the t2k neutrino beam using neutrino interactions in the near detecto. http://www.t2k.org/docs/thesis/060/sarahivesthesis, 2012.

[79] Rebekah J Smith. Measurement of kaon and pion contributions to the t2k neutrino beam. http://www.t2k.org/docs/thesis/056/rjsthesis, 2013.

[80] K. Abe et al. Measurement of neutrino and antineutrino oscillations by the t2k experiment including a new additional sample of ν_e interactions at the far detector. *Phys. Rev. D*, 96:092006, Nov 2017.

[81] K. Abe et al. Proposal for an Extended Run of T2K to 20×10^{21} POT. 2016.

[82] K. Abe et al. Physics potential of a long-baseline neutrino oscillation experiment using a J-PARC neutrino beam and Hyper-Kamiokande. *PTEP*, 2015:053C02, 2015.

[83] The Nova Collaboration. Constraints on oscillation parameters from ν_e appearance and ν_μ disappearance in nova. *Phys. Rev. Lett.*, 118:231801, Jun 2017.

[84] L. Aliaga et al. Neutrino Flux Predictions for the NuMI Beam. *Phys. Rev.*, D94(9):092005, 2016. [Addendum: Phys. Rev.D95,no.3,039903(2017)].

[85] T2K Technical 212. Numu cc event selections in the nd280 tracker using run 2+3+4.

[86] T2K Technical 152. Cc multiple pion nu-mu event selections in the nd280 tracker using run 1+2+3+4 data.

[87] T2K Technical Note 248. Cc numu background event selection in the nd280 tracker using run 5c+run 6 anti-neutrino beam data.

[88] T2K Technical Note 246. Cc anti-nu event selection in the nd280 tracker using run 5c and run 6 anti-neutrino beam data.

[89] R Mankel. Pattern recognition and event reconstruction in particle physics experiments. *Reports on Progress in Physics*, 67(4):553, 2004.

[90] A. Izmaylov. Highland tutorial, june 2017.

[91] T2K Technical 265. Updated recommendation of the 2015 niwg parameters.

[92] Dariusz Dereniowski and Marek Kubale. Cholesky factorization of matrices in parallel and ranking of graphs. In Roman Wyrzykowski, Jack Dongarra, Marcin Paprzycki, and Jerzy Waśniewski, editors, *Parallel Processing and Applied Mathematics*, pages 985–992, Berlin, Heidelberg, 2004. Springer Berlin Heidelberg.

[93] T2K Technical 149. Measurement of the electron neutrino beam component in the nd280 tracker for 2013 analyses.

[94] D. Brailsford. Private communication.

[95] K. Iwamoto. Ingrid beam measurement status mr run 77 rhc, 2017.

[96] Dominic Brailsford. Measurement of the charged current inclusive muon neutrino interaction cross-section on lead using the t2k nd280 electromagnetic calorimeters. https://t2k.org/docs/thesis/066/ECalCCAnalysis.

[97] Luke Pickering. Measurement of lead-target neutrino interactions using the whole t2k near detector. https://t2k.org/docs/thesis/083/thesis, 2017.